ON THE INTERACTION AMONG THE EXTRATROPICAL ATMOSPHERIC TRANSIENTS OF DIFFERENT FREQUENCIES

By

Hai Lin

SUBMITTED IN PARTIAL FULFILLMENT OF THE
REQUIREMENTS FOR THE DEGREE OF
DOCTOR OF PHILOSOPHY
AT
McGILL UNIVERSITY
MONTREAL, QUEBEC
DECEMBER, 1994

ISBN 0-612-05745-3

A shortened version of the thesis title:

Interaction among extratropical transients of different frequencies

Abstract

The dynamics of low-frequency fluctuations (periods between 10 days and a season) is investigated. While those fluctuations are known to be forced, at least in part, by the underlying surface, the emphasis in this thesis is placed on processes taking place within the atmosphere.

The thermal interaction between the high-frequency (periods 2 to 10 days) and the low-frequency flow is first investigated. The temporal and spatial relationship between the heat flux convergence by the synoptic-scale eddies and the low-frequency temperature field is identified. It is shown that the low-frequency temperature fluctuations are negatively correlated with the heat flux convergence by the synoptic-scale eddies, implying the damping effect of high-frequency eddy heat flux on the slowly varying temperature field. The damping effect is not homogeneous in space, however, and different temperature patterns have different damping rates. The low-frequency temperature patterns over the North American and Siberian inland areas, where the strongest low-frequency temperature variances are observed, are associated with weak damping from the high-frequency eddies. A stronger dissipation is found for the low-frequency temperature variations in the storm track regions.

We then examine the El Niño-related interannual variations of the transient eddy activity and the associated multiscale interactions. A dataset from the U. S. National Meteorological Center (NMC) of 24 years is used. The purpose is to determine when the seasonal mean flow is less dependent on processes internal to the atmosphere and therefore more dependent on external forcing and thus more predictable. The results show that during El Niño winters the low-frequency eddy activity is reduced over

the North Pacific and the high-frequency baroclinic waves are shifted south-eastward of their normal position in the Pacific. Over the North Pacific less kinetic energy is supplied to the low-frequency eddies both from the large-scale seasonal mean flow and from the synoptic-scale eddies. Thus the atmosphere in that region is more "stable" during El Niño winters, and its state depends more on the external forcings.

Finally, the atmospheric predictability is studied explicitly. A large number of numerical experiments are performed to determine whether the forecast skill is dependent on the weather regimes. The predictions are made with a T21 three-level quasi-geostrophic model. The relationship between the forecast behaviour and the "interannual" variation of the Pacific/North American (PNA) anomaly is investigated. Comparison of the error growth for the forecasts made during the positive and negative PNA phases indicates that little difference of error growth can be realized before about a week. After that period the forecast error grows faster during the negative PNA phases. The forecast skill for the medium- and long-range predictions over the North Pacific, the North American and the North Atlantic regions is higher during the positive PNA phase than that during the negative PNA phase. A global signal of this relationship is also observed. The physical mechanism for the difference of error growth is discussed.

Résumé

On étudie la dynamique de la variabilité lente (périodes de 10 jours à une saison) de l'atmosphère. Il est connu que ces fluctuations sont forcées, du moins en partie, par l'action des océans et du sol sur l'atmosphère, mais cette thèse met l'accent sur les processus internes de l'atmosphère.

On examine d'abord l'interaction thermique entre les fluctuations à hautes fréquences (périodes de deux à 10 jours) et la variabilité lente (ou basses fréquences). Les relations temporelle et spatiale entre la convergence du flux de chaleur reliée aux systèmes synoptiques et la variabilité lente sont identifiées. On démontre qu'il existe une corrélation négative entre le champ de température à basse fréquence et la convergence du flux de chaleur induite par les systèmes synoptiques, de sorte que ces derniers atténuent, par leur flux thermique, la variabilité lente de la température. Le degré d'atténuation n'est pas spatialement homogène, par contre, de sorte que différents patrons de température à basses fréquences, situés à différents endroits, ont des taux d'atténuation différents. Les structures spatiales de la variabilité lente de la température situées sur l'Amérique du nord et la Sibérie ont de faibles taux d'atténuation par le flux de chaleur des ondes synoptiques; celles situées sur les trajectoires moyennes des ondes synoptiques, par contre, ont des taux de dissipation thermiques plus élevés.

On examine les fluctuations interannuelles reliées au phénomène El Niño et les fluctuations correspondantes dans les interactions entre les systèmes de différentes fréquences. Un jeu de données de 24 ans du Centre météorologique national américain est utilisé. Le but est de déterminer si dans certaines circonstances l'écoulement est

relativement moins influencé par les processus internes de l'atmosphère, et relativement plus contrôlé par un forçage externe, et de ce fait potentiellement plus prévisible. Les résultats indiquent que pendant les hivers où un El Niño est en cours l'intensité de la variabilité lente est plus faible sur le Pacifique nord, et les ondes baroclines à hautes fréquences se retrouvent au sud-est de leur position normale sur le Pacifique. Sur le Pacifique nord, l'écoulement à basses fréquences reçoit moins d'énergie de l'écoulement saisonnier et des systèmes synoptiques. Dans cette région l'atmosphère est plus "stable" pendant les hivers où un El Niño est en cours, et son état est plus influencé par les forçages externes.

Pour terminer, on étudie explicitement la prévisibilité de l'atmosphère. Des expériences numérique sont faites en grand nombre pour déterminer si la qualité des prévisions est fonction du régime de temps. Les prévisions sont faites à l'aide d'un modèle quasi-géostrophique à trois niveaux et à résolution triangulaire 21 (T21). On étudie la relation entre la qualité des prévisions et les fluctuations du patron PNA (Pacific North American pattern). Une comparaison de la croissance des erreurs de prévision en présence des phases positives, d'une part, et négatives, d'autre part, du patron PNA indique peu de différence au cours de la première semaine de prévision. Par la suite les erreurs de prévision croissent plus vite en présence de la phase négative du patron PNA. La qualité des prévisions à moyenne et longue échéances est plus élevée sur le Pacifique nord, le continent américain et l'Atlantique nord pendant la phase positive du patron PNA que pendant sa phase négative. Cette différence de qualité est aussi observée (à un moindre degré) lorsque l'on examine l'erreur moyenne globale des prévisions. On discute des mécanismes physiques responsables de ces différences.

Acknowledgments

I would like to express my deepest thanks to my supervisor, Professor Jacques Derome, for his guidance throughout this work. His constant encouragements and invaluable assistances made my study at McGill an enjoyable experience. I benefited greatly from his profound and extensive knowledge of atmospheric dynamics.

I am grateful to Dr. John Fyfe, who supervised me during my one-year study in the Department of Oceanography, University of British Columbia and introduced me to Professor Derome.

I acknowledge Alan Schwartz' help in solving some computer problems. I would also like to thank Marc Klasa who helped me proof-read part of this thesis.

I am indebted to Dr. Franco Molteni for his permission to use the three-level quasi-geostrophic model in Chapter 4 of this thesis.

I would thank the Natural Sciences and Engineering Research Council and the Atmospheric Environment Service of Canada for financial support during my study.

Finally I would like to thank my wife, Wei, and my son, Yulong, for their patience, understanding and support.

Contents

List of Figures

List of Symbols

a: Earth's radius (6.371×10^6 m)

$\mathcal{A}$: temperature advection by time-mean horizontal flow, Eq. (2.5)

$\mathcal{A}_l$: low-frequency temperature advection, Eq. (2.6)

$\mathcal{B}$: temperature advection by time-mean vertical motion and adiabatic effect, Eq. (2.5)

$\mathcal{B}_l$: low-frequency temperature advection by vertical motion and adiabatic effect, Eq. (2.6)

C: barotropic conversion of kinetic energy from mean flow to low-frequency transients

$\mathcal{C}_l$: low-frequency projection of horizontal heat flux convergence by transients, Eq. (2.6)

c_p: specific heat at constant pressure

$D_i (i = 1, 2, 3)$: diffusion of potential vorticity, Eq. (4.1)

$\mathcal{D}$: time-averaged vertical heat flux by transients, Eq. (2.5)

$\mathcal{D}_l$: low-frequency vertical heat flux, Eq. (2.6)

E: forecast error variance of streamfunction

E_{rms}: rms error of 500 hPa geopotential height

$\mathbf{E}$: extended E–P flux

F_c: geopotential height tendency of mean flow caused by the transients, Eq. (1.2)

$F_i (i = 1, 2, 3)$: potential vorticity forcing, Eq. (4.1)

f: Coriolis parameter

$\mathcal{F}_a$: anomalous high-frequency forcing of El Niño winters via that of non-El Niño winters, Eq. (3.3)

g: acceleration due to gravity (9.81 m s^{-2})

$\mathcal{G}_a$: anomalous low-frequency forcing of El Niño winters via that of non-El Niño winters, Eq. (3.3)

h: orographic height

H_0: atmospheric scale height

$\mathcal{H}_a$: anomalous $\overline{\mathcal{R}}$ of El Niño winters via that of non-El Niño winters, Eq. (3.3)

n: length of time series

n_{eff}: effective number of freedom

p: pressure

Q: diabatic heating

$q_i (i = 1, 2, 3)$: potential vorticity

R: gas constant for dry air

R_1(=700 km) and R_2(=450 km): Rossby radii of deformation for the 200-500 hPa layer and the 500-800 hPa layer

$\overline{\mathcal{R}}$: remaining components in time-mean vorticity balance equation other than eddy vorticity flux convergence, Eq. (3.1)

$\mathcal{R}_l$: remaining components in low-frequency vorticity balance equation other than eddy vorticity flux convergence, Eq. (3.5)

$\Re$: remaining components in time-mean geopotential tendency equation other than eddy vorticity flux convergence, Eq. (1.2)

T: temperature

t: time

u: eastward component of velocity

v: northward component of velocity

$\mathbf{V}$: horizontal velocity vector

Z_f: forecasted 500 hPa geopotential height

Z_o: "observed" 500 hPa geopotential height

z: geopotential height

z^*: normalized seasonal geopotential height anomaly

ϕ: latitude

$\psi_i (i = 1, 2, 3)$: streamfunction

ψ_f: forecasted streamfunction

ψ_o: "observed" streamfunction

λ: longitude

Ω: angular velocity of the earth

ω: vertical component of velocity in pressure coordinates

ζ: relative vorticity

$\overline{()}$: time average

$()'$: departure from time average

$()_h$: high-frequency component of a time series

$()_l$: low-frequency component of a time series

$\{\}_a$: $= \{\}_e - \{\}_n$, anomaly of El Niño winters via non-El Niño winters

$\{\}_e$: composite of El Niño winters

$\{\}_n$: composite of non-El Niño winters

∇: horizontal gradient operator

∇^{-2}: inversion of the two-dimensional Laplacian on a sphere

$J(a, b)$: Jacobian operator

Statement of Originality

The original results contained in this thesis are as follows:

1) With a resolution of 12 hours, the phase relationship (in time) between the low-frequency temperature and the heat-flux convergence by the synoptic-scale eddies is investigated. The low-frequency temperature variations are negatively correlated in time with the *in situ* synoptic-scale heat flux convergence with a very small time lag;

2) A spatial difference in the low-frequency temperature field and the heat flux convergence by the synoptic-scale transients is found. The eddy heat flux convergence has a smaller damping effect on the low-frequency temperature field in the inland regions than on that connected with the fluctuations within the storm tracks;

3) Significant correlations are found between the low-frequency eddy activity and El Niño events. During El Niño winters, which are normally associated with an enhanced Pacific/North American (PNA) pattern, the low-frequency eddy activity is reduced over the North Pacific;

4) The weak low-frequency activity during El Niño winters over the North Pacific is explained by a smaller kinetic energy transfer to the low-frequency eddies from the seasonal mean flow and a weaker synoptic-scale eddy forcing;

5) A large number of numerical experiments have been performed to determine whether the forecast skill is dependent on the circulation patterns. Comparison of the error growth for the forecasts made during the positive and negative PNA phases indicates that the forecast skill for the medium- and long-range predictions over the North Pacific, North American and the North Atlantic regions is higher during the positive PNA phases than that during the negative PNA phases. A global signal of

this relationship is also observed.

6) A physical mechanism for the difference between the error growth during the positive and negative PNA phases is provided.

7) Based on the fact that all the variabilities in our model are caused by internal nonlinear processes and that the system has a single climatology, the regime-dependent systematic error, which is negatively correlated with the slowly-varying PNA pattern, is explained.

Chapter 1

Introduction

1.1 Overview of the extratropical transients

The atmosphere exhibits variability on all spatial and temporal scales. To show the variability and the relative importance of different scales of motion in the atmosphere, a spectrum of kinetic energy with periods between seconds and several years is presented in Fig. 1.1. The peaks of the kinetic energy occur at 1 day, from a few days to a few weeks, and around 1 year. The first and the third peaks are related to the diurnal and annual cycles, respectively, while the second maximum is associated with large-scale transient disturbances in the middle latitudes. As this thesis will examine such issues as synoptic-scale and low-frequency eddies, eddy interactions, and predictions of slowly-varying processes in the atmosphere, the current understanding of the extratropical transients and their interactions with other scales of motion will be briefly reviewed in this Introduction.

1.1.1 Synoptic-scale eddies and storm tracks

The day-to-day weather changes in the middle latitudes of the Northern Hemisphere can often be related to the passage of highs and lows in the sea surface pressure field. These synoptic-scale disturbances on daily weather maps are characterized by

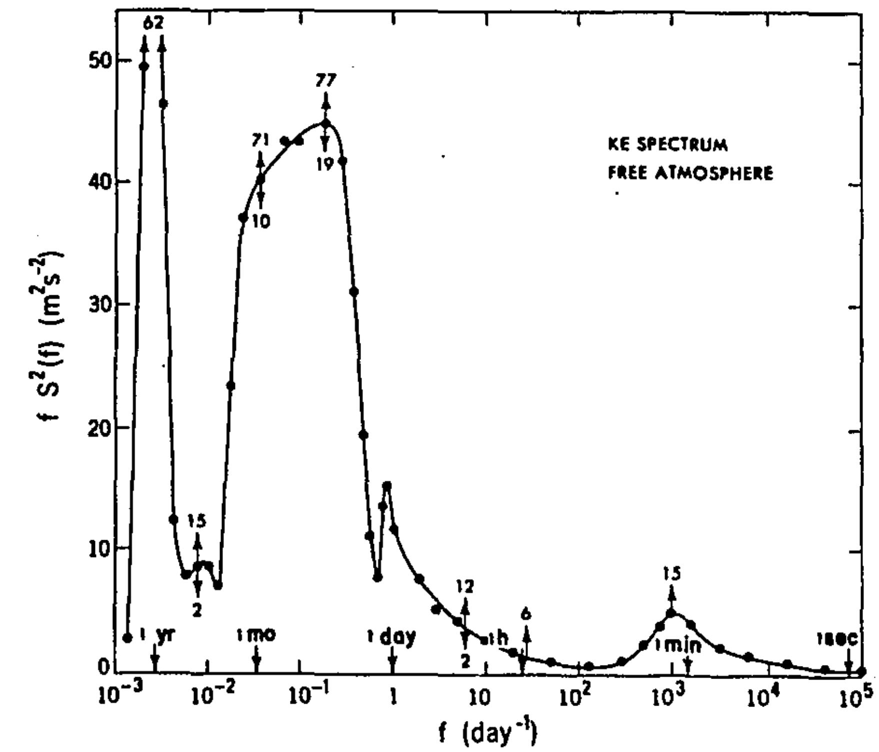

Figure 1.1: Spectrum of atmospheric kinetic energy. The abscissa axis is in units of $\log f$ and the ordinate axis in units of $fS^2(f)$, where f is the frequency and $S^2(f)$ is the explained variance. [From Vinnichenko, 1970]

periods ranging from a few days to about a week. The disturbances are arranged in the form of waves, with a mean zonal wavelength of about 4000 km, a westward tilt with height, and a mean eastward phase speed of 12–15 m s^{-1} (Wallace et al., 1988). The theory of baroclinic instability of the basic flow, pioneered by Charney (1947) and Eady (1949), is the generally accepted explanation for their existence.

The climatology of the synoptic-scale transients has been documented by a series of observational studies by Blackmon (1976) and Blackmon et al. (1977, 1984a, 1984b). It was shown that disturbances in the bandpass-filtered (periods of 2.5–6 days) data exhibit two zonally-elongated variance maxima over the North Pacific and North Atlantic for the meridional wind, temperature, geopotential height and vertical motion variables. Strong northward transports of heat and vorticity by the high-frequency eddies also take place in these regions. These zonally-elongated variance maxima coincide closely with the "storm tracks" as inferred from the frequency distribution and movement of the centres of cyclones (e.g., Petterssen, 1956). Thus, the maxima in the temporal variance are referred to as storm tracks, corresponding to the regions of strongest baroclinic wave activity. Wallace et al. (1988) argued that since the temporal variance comes from the propagation of both cyclones and anticyclones, the term "baroclinic waveguides" may be more appropriate as it does not imply a sense of polarity. However, very small differences were found in the propagation characteristics of positive and negative geopotential height anomalies in these regions. Thus the term "storm tracks" has been widely accepted in the literature and refers to the zonally-elongated maxima in the root-mean-square (rms) of bandpass-filtered geopotential height.

The planetary-scale waves in the time-mean flow tend to organize the synoptic-scale transient eddies into localized regions, or storm tracks, downstream of the main stationary pressure troughs. In a linear stability analysis of the observed wintertime flow, Frederiksen (1979) found a strong geographical dependence of the growing baroclinic modes on the longitudinal phase of the climatological planetary-scale waves. Lau (1988) investigated the month-to-month variation of the storm tracks and found that it was linked to the changes in the monthly averaged circulation pattern. The monthly averaged flow field induces a strong modulation of the trajectory of weather systems so that the storm tracks are preferentially located slightly downstream of the quasi-stationary troughs.

1.1.2 Eddy forcing of the time-mean flow

The existence and geographical position of storm tracks are dependent on the planetary-scale waves in the time-mean flow. On the other hand, the synoptic-scale eddies feed back onto the time-mean flow through the transports of vorticity and heat. This feedback process can modify the structure of the time-mean flow, and thus is referred to as eddy forcing.

Various analysis tools used to diagnose the eddy forcing on the time-mean flow have appeared in the literature. A comprehensive review of these diagnostic methods has been given by Holopainen (1984). Here we briefly describe the geopotential height tendency method.

To illustrate this method in a simple way, we start with the barotropic vorticity equation:

$$\frac{\partial \zeta}{\partial t} = -\nabla \cdot [(\zeta + f)\mathbf{V}] + D, \tag{1.1}$$

where ζ is the relative vorticity, $\mathbf{V}$ the horizontal velocity vector, and f the Coriolis parameter. D represents all the subgrid dissipative effects. By decomposing the variables into the time-mean and transient parts and using the geostrophic relationship, the equation for the geopotential height tendency of the time-mean motion can be written as

$$\frac{\partial \overline{z}}{\partial t} = F_e + \Re. \tag{1.2}$$

The term associated with the transient eddy vorticity flux, or barotropic eddy forcing, may be expressed as

$$F_e = -\frac{f}{g}\nabla^{-2}\nabla \cdot \overline{\zeta' \mathbf{V}'}, \tag{1.3}$$

where the operator ∇^{-2} denotes the inverse of the two-dimensional Laplacian on the sphere. The overbar represents a time average, and the prime represents a departure from the time average. To get the eddy vorticity forcing, the transient eddy vorticity flux convergence is first calculated using observational data, and an inverse of Laplacian operator is applied, which emphasizes the large-scale structure and makes the tendency field rather smooth. $\Re$ in Eq. (1.2) represents all the remaining terms in the time-mean geopotential tendency, such as horizontal advection by the time mean, and dissipation.

This technique of geopotential height tendency analysis was first introduced by Lau and Holopainen (1984). Instead of using the barotropic vorticity equation, they employed the quasi-geostrophic potential vorticity equation. The latter takes into account both the direct effect of the transient vorticity fluxes and the indirect effect of the eddy induced secondary circulation. This ensures that the geopotential tendency is in geostrophic and hydrostatic balance. As calculated by Lau and Holopainen (1984), the geopotential tendency of the time-mean flow associated with synoptic-scale eddies of periods between 2.5 and 6 days reaches maxima near the oceanic storm tracks. The vorticity flux convergence by synoptic-scale eddies leads to an eastward acceleration of the mean flow throughout the troposphere. Thus a positive feedback by the eddies works to enhance the westerly jet. Through the constraints of geostrophic and hydrostatic balance, the effect of the eddy heat flux on the geopotential tendency could also be evaluated. The eddy heat flux convergence tends to reduce the vertical shear of the westerlies along the storm tracks.

1.1.3 Intraseasonal variability

The intraseasonal temporal scales are those ranging from approximately one week (life time of a cyclonic system) to a season (3 months). The transients in this temporal span are also called low-frequency variabilities.

Investigations of the low-frequency, or intraseasonal, fluctuations are numerous. A comprehensive review of these studies can be found in Wallace and Blackmon (1983), and in a recent report by Pandolfo (1993). In contrast to the synoptic-scale eddies, whose three-dimensional structure and time evolution are quite well understood, the dynamics of the low-frequency variabilities are less clear. A frequency spectrum of a variable generally shows a broad peak between one week and a season, so that variabilities with a wide range of frequencies are contained in the intraseasonal time span. The circulation patterns on intraseasonal scales thus can be described only in rather general terms. This also makes it difficult to explain the cause of the low-frequency variability, because several mechanisms may be working together and interacting with each other.

The amplitude of the low-frequency fluctuations has a strong geographical dependence. During the winter season the temporal variance of the low-pass filtered (periods 10–90 days) 500 hPa geopotential height reaches a maximum over the North Atlantic and North Pacific, and over northwest Siberia, near 80°E (Blackmon, 1976; Blackmon et al., 1977, 1984a, and 1984b; Wallace and Blackmon, 1983). The two oceanic areas coincide with the ends of the storm tracks. A synoptic meteorologist might say that they represent the graveyards of cyclones at the ends of the two major storm tracks across the Pacific and Atlantic oceans, where the storms have entered the dissipating stage and become quasi-stationary. The centres of the low-pass variance in the Pacific and Atlantic also correspond closely to the longitudes with the highest percentage of blocking flows, as determined by Rex (1950).

The horizontal structure of the low-frequency eddies was revealed by a one-point correlation map, which correlates the low-pass filtered 500 hPa height at a specific point (usually the centre of the low-frequency activity) with the low-pass filtered 500 hPa height at every other gridpoint (e.g., Wallace and Blackmon, 1983). The correlation patterns from the low-pass filtered data are very different from those of higher frequency eddies, which have the structure of baroclinic waves. The correlation patterns for the low-frequency fluctuations have two-dimensional wave structures and larger scales. According to the geographical structure of the correlation patterns calculated from the wintertime monthly-mean 500 hPa geopotential height, Wallace and Gutzler (1981) identified five types of patterns. They are the Pacific/North American pattern (PNA), the West Atlantic pattern (WA), the East Atlantic pattern (EA), the Eurasian pattern (EU), and the West Pacific pattern (WP). The wavelike structures associated with these correlation patterns are much more clearly defined at the 500 hPa level than at the Earth's surface and their vertical structure may be regarded as equivalent barotropic with amplitude increasing with height.

A proper understanding of the mechanisms responsible for the genesis and maintenance of the low-frequency fluctuations is essential if we are to succeed in making reasonably accurate medium- and long-range weather predictions. The numerical models used to make these kinds of predictions should be able to simulate the evolutions of those transients with time scales longer than the life time of the cyclones.

One of the possible mechanisms for generating the low-frequency variabilities is the barotropic instability of the zonally-varying climatological basic state. Using a global barotropic model, linearized about the climatological mean 300 hPa wintertime flow, Simmons et al. (1983) were able to show that there are preferred patterns resulting from the dispersion of isolated initial perturbations distributed throughout the tropics and subtropics. These patterns tend to have structures similar to those of the observed Pacific/North American (PNA) and the East Atlantic (EA) patterns. It was also shown that these patterns are related to the most rapidly growing normal modes of the barotropic vorticity equation, linearized about the climatological 300 hPa wintertime flow.

The lower boundary forcing provided by the oceans can also induce low-frequency fluctuations in the atmosphere. The theoretical work on Rossby wave dispersion on a sphere provides an appealing description of the horizontal structures of the low-frequency fluctuations (e.g., Hoskins et al., 1977; Hoskins and Karoly, 1981). The theory predicts that the atmospheric planetary-scale response to a geographically localized tropical forcing takes the form of a wavetrain along a "great circle" emanating from the tropics, turning eastward to become tangent to a latitude circle, and curving back into the tropics.

Another process which is important in the dynamics of the low-frequency variabilities is the interaction with the high-frequency transients. The high-frequency eddies interact with the low-frequency fluctuations through their transports of vorticity and heat. The observational study by Green (1977) showed that the fluxes of vorticity due to the high-frequency transients act to maintain the low-frequency anomalies. From composite studies of the blocking events in the midlatitudes during the episodes of persistent geopotential height anomalies, Mullen (1987) found that the high-frequency synoptic eddies systematically transport vorticity into the upstream side of the blocking high, preventing it from being advected downstream by the time-mean flow. Lau (1988) investigated the relationship between the mean monthly circulation anomalies and the corresponding anomalies in the vorticity flux divergence by the synoptic-scale eddies. His results indicate that the eddy forcing in individual months tends to reinforce the concurrent mean monthly anomalies. By investigating the optimal relation between the low-frequency patterns and the high-frequency forcing, Metz (1990, 1991) arrived at similar results. Klasa et al. (1992) used 23 winters of NMC data to show that during months when the Pacific-North American (PNA) anomaly pattern is observed, the vorticity flux divergence associated with the synoptic-scale eddies leads to height tendencies that are spatially in phase with the PNA pattern. In a recent paper by Sheng and Derome (1993), the structure of the vorticity forcing by the synoptic-scale eddies and its relationship with the slow transients were investigated. They found that the fluctuations of the low-frequency transients are positively correlated in time with the vorticity forcing by the synoptic-scale eddies. In the eastern part of the Pacific and Atlantic basins, where the low-frequency transients achieve their maximum kinetic energy, a significant portion of the temporal variance of the slow transient height field can be related to the synoptic-scale vorticity forcing.

1.1.4 Energetics view of the eddy interactions

We have seen that the interactions between different time scales are important in explaining the existence of the slow transients and their features. The synoptic-scale eddies owe their existence to a baroclinic conversion of energy from the time-mean flow. The barotropic conversion of energy from the zonally inhomogeneous time-mean flow is an important source of energy for the low-frequency variabilities. The high-frequency eddies feedback onto the time-mean flow, through the vorticity and heat fluxes, and the forcing by the high-frequency transients plays an important role in maintaining the low-frequency flow.

A confirmation of the above is obtained by examining the energy transfer among the time-mean flow, the high- and the low-frequency transients. Using the atmospheric momentum and thermodynamic equations in spherical coordinates and decomposing each variable into the time-mean, the low-frequency and the high-frequency parts, Sheng and Hayashi (1990) derived the spectral energy equations in the frequency domain. Using a 5-year data set from the operational analyses of the European Centre for Medium Range Weather Forecasts (ECMWF), Sheng and Derome (1991a) studied the atmospheric large-scale energetics of the Northern Hemisphere in the frequency domain. The transient fluctuations were divided at a period of 10 days into low- and high-frequency groups. The energy cycle for the Northern Hemisphere winter season is presented in Fig. 1.2. The number given in each box is the amount of energy of the specified form and frequency band in units of 10^4 J/m^2. The arrows indicate the directions of the energy flow, while the values on the arrows give the rates of energy transfer in units of W/m^2.

From the energy cycle diagram we see that the energy source for the atmospheric system is the generation of time-mean available potential energy. This diabatic process is accomplished by the heating of the warm air in the equatorial latitudes and the cooling of the cold air in the polar latitudes, which builds up a strong north-south temperature gradient. The available potential energy of the time-mean flow is transferred to transient disturbances of both high and low frequencies, and the low-frequency available potential energy flows to the high-frequency transients. These transfers of available potential energy from slower transients down to the shorter time scales imply that the thermal interactions between eddies of different time scales cause a thermal "dissipation" of the slower ones. The available potential energy is converted to kinetic energy at all frequency bands. This result indicates that through mechanisms such as baroclinic instability, some of the eddy available potential energy is transformed into kinetic energy of the growing disturbances for both the low- and high-frequencies. The energy converted to the high-frequency eddies is the only

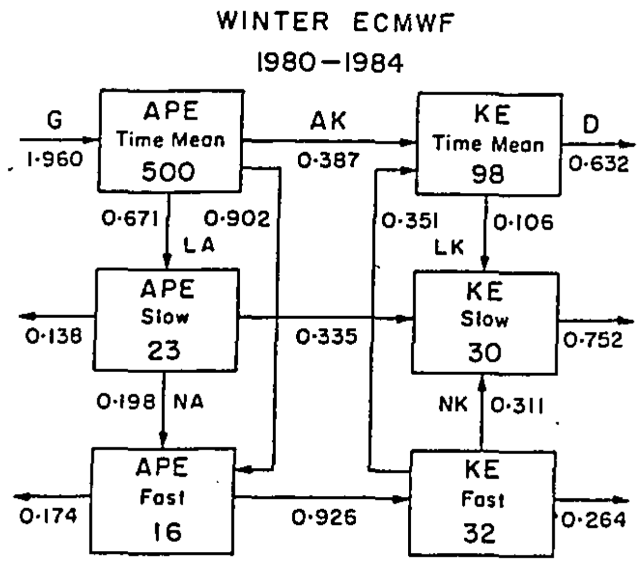

Figure 1.2: Schematic diagram of the atmospheric energy cycle in the frequency domain for the Northern Hemisphere in winter. The numbers in boxes denote the energy storage in units of 10^4 J/m^2, and the arrows represent energy conversions or exchanges in W/m^2. [From Sheng and Derome, 1991a]

kinetic energy source of the synoptic-scale eddies. The barotropic feedback process from the high-frequency eddies to the time-mean flow is clear from this diagram, which shows that the synoptic-scale eddies supply kinetic energy to the time-mean flow. As for the low-frequency fluctuations, the baroclinic conversion, although still important, is no longer the unique kinetic energy source. The low-frequency transients get kinetic energy also from two other processes, one being the interaction with the high-frequency eddies. This energy transfer is comparable with the baroclinic conversion, and is seen to be a major source of kinetic energy of the low-frequency fluctuations. The other process providing kinetic energy to the low-frequency eddies is the transfer of kinetic energy from the time-mean flow, which is consistent with the barotropic instability of the zonally-varying climatological basic state as proposed by Simmons et al. (1983). The kinetic energy of all frequency groups is dissipated by frictional processes.

From further local energy analyses, Sheng and Derome (1991a) showed that the low-frequency fluctuations over the continental areas are maintained primarily through the baroclinic conversion, while those over the oceans are maintained mainly by the barotropic energy transfer from the seasonal mean flow and the nonlinear energy transfer from the high-frequency eddies.

1.2 Motivation of the present study

The ultimate goal of atmospheric dynamical studies is to perform accurate predictions of the atmosphere. With the growth in power of high-speed computers, more and more sophisticated numerical models have been developed, which are taking into account more details of the atmospheric processes. These modern numerical models have proved to be very useful tools to make weather predictions. As was first pointed out by Lorenz (1963), there is a limit, however, to the predictability of the atmosphere due to two important reasons: 1) no matter how sophisticated the model is, it has only a finite number of degrees of freedom to approximate a continuum; 2) it is impossible to have a perfect knowledge of the initial conditions, and the initial errors eventually spread throughout the model. The estimation of the maximum time period over which weather forecasts can remain useful has been the subject of much interest (Charney et al., 1966; Lorenz, 1969). This limit to the predictability is thought to be of the order of two weeks, but at present forecasts typically remain useful for only about one week.

A time limit on weather forecasting skill does not imply that medium- to long-range and climate predictions are similarly restricted, since the weather might be regarded as noise on the predictable, slowly-varying signals. There exist some indications that the slowly-changing processes in the atmosphere are potentially predictable. Madden (1976) estimated the natural variability of the monthly-mean sea-level pressure arising from (forced by) the daily weather fluctuations. He argued that this natural variability is essentially unpredictable and can be therefore regarded as climate noise. Comparisons between the actual variability and the natural variability indicated that in some areas (south of 40°N and north of 60°N), the actual variability exceeds the natural variability. This result implies that some of the actual variability is caused by mechanisms other than the higher frequency weather disturbances. Although these mechanisms were not known, the part of the variability caused by them was considered to be at least potentially predictable. Using a three-dimensional quasi-geostrophic channel model of the atmosphere, Tung and Rosenthal (1986) argued that quasi-stationary long waves can probably be predicted at extended ranges if the boundary forcings are known during the integration.

As can be seen from the above, if we want to make a useful medium- to long-range atmospheric prediction, (1) the numerical model must include the potentially predictable slowly-varying signals; as discussed in the overview, these signals may come from the boundary conditions, barotropic instability of the mean flow, eddy forcing, etc.; (2) the effect of the weather noise must be small, or else treated properly.

Thus it is important to understand the effect of the high-frequency eddies on the slowly-varying processes, especially in extratropics where the interaction is strong. We will approach this point in Chapter 2, where the thermal effects of the high-frequency eddies on the slowly-varying flow will be discussed.

Another important issue in medium- to long-range and climate prediction arises from the fact that the predictive skill exhibits considerable variability. Mansfield (1986) discussed the extended range forecast skill of the UK Meteorological Office 5-layer model over 18 wintertime cases with initial conditions from December 1974 to December 1981. He noted that although on average the correlation between the forecasts and observations fell to zero by about 19 days, some forecasts had exceptional skill. Miyakoda et al. (1986) reported on the analysis of eight extended range forecasts with the GFDL model. Some of their 30-day-mean scores also showed quite encouraging results. One obvious question here is "what causes the variation in the forecasting skill?". Extended range weather predictions would be more valuable if we could evaluate, *ab initio*, the probable accuracy of every medium- to long-range prediction.

An observational study will be presented in Chapter 3 to investigate the interannual variations of the extratropical transients and their interactions. By doing so, we can identify periods when the atmosphere's internal processes are less important, so that the seasonal mean flow is more dependent on external forcing and thus potentially more predictable. Furthermore, in Chapter 4 a global spectral three-level quasi-geostrophic model will be used to study the dependence of predictability on the atmospheric flow patterns.

Chapter 2

On the Thermal Interaction between the Synoptic-Scale Eddies and the Intra-Seasonal Fluctuations in the Atmosphere

2.1 Introduction

As discussed in the overview, the high-frequency eddies interact with the low-frequency fluctuations through their transports of vorticity and heat. The relationship between the time evolution of the synoptic-scale eddies and that of the low-frequency fluctuations remains to be clarified. Lau (1988) has addressed this issue by studying the relationship between the mean monthly circulation anomalies and the corresponding anomalies in the vorticity flux divergence (geopotential tendency) by the synoptic-scale eddies. His results indicate that the eddy forcing in individual months tends to reinforce the concurrent mean monthly anomalies. By investigating the optimal relation between the low-frequency patterns and the high-frequency forcing, Metz (1990, 1991) arrived at similar results. Klasa et al. (1992) used 23 winters of NMC data to show that during months when the Pacific-North American (PNA) anomaly pattern is observed, the vorticity flux divergence associated with the synoptic-scale eddies leads to height tendencies that are spatially in phase with the PNA pattern.

In a recent paper by Sheng and Derome (1993), the structure of the vorticity forcing by the synoptic-scale eddies and its relationship with the slow transients were investigated using 300 hPa data with a time resolution of 12 hours. The transient fluctuations were divided at a period of 10 days into low and high frequency components. They found that the fluctuations of the low-frequency transients are positively correlated in time with the vorticity forcing by the synoptic-scale eddies. In the eastern part of the Pacific and Atlantic basins, where the low-frequency transients achieve their maximum kinetic energy, a significant portion of the time variance of the slow transient height field can be related to the synoptic-scale vorticity forcing.

The synoptic-scale eddies interact with the low-frequency flow not only through their vorticity flux, but also through their heat flux. The effect of the eddy heat flux on the slowly-varying temperature field is of interest if one wants to parameterize this effect in a low resolution climate model. Holopainen et al. (1982) has shown that the sensible heat transport by the synoptic-scale eddies acts to damp the temperature variance in the mean seasonal flow and the energetics calculations of Sheng and Derome (1991a) have confirmed that the damping effect also applies to the low-frequency flow. It is not clear from the above studies, however, how well the low-frequency temperature fluctuations and the synoptic-scale heat flux divergence are correlated in time.

In this chapter, we will investigate the thermal interaction between the low-frequency temperature and the low-frequency heat flux divergence by the synoptic-scale eddies. The spatial structures of the two quantities and their temporal phase relationship will be examined. In addition, we will examine the relative importance of the heat flux divergence by the synoptic-scale eddies in determining the low-frequency thermal variance. One significant difference between this study and that of Lau and

Nath (1991) is that we consider the time fluctuations of the low-frequency temperature field and the corresponding eddy heat flux convergence with a resolution of 12 hours, rather than on the basis of mean monthly anomalies. This allows us to examine the phase relationship (in time) between the low-frequency temperature and the thermal eddy fluxes.

2.2 Data and diagnosis procedure

2.2.1 Data set and filtering

The data base for this part of the study consists of the twice-daily (00 and 12 GMT) analyses for 5 individual winters (1981-82 to 1985-86) from the European Centre for Medium-Range Weather Forecasts (ECMWF). The winter season is taken to be the 120-day period starting from November 16. The data set and the period are so chosen in order to be consistent with the study of Sheng and Derome (1993) on the barotropical interaction between the low-frequency transients and the synoptic-scale eddies. The selected variables include the temperature T, the horizontal wind components u and v, and the vertical motion field ω. The variables are abstracted at 700 hPa, except for the temperature which is also needed at 850 and 500 hPa to calculate its vertical advection. The domain covers the entire Northern Hemisphere with a resolution of 5 degrees in both longitude and latitude. The data were checked for possible errors and no suspicious or missing records were found during this period.

We remove the seasonal cycle by fitting a least-squares parabola to each winter's data and subtracting it from the unfiltered time series. For all the remaining time series we apply the same procedure as Sheng and Derome (1993), i.e. Fourier filtering to generate the slow and fast transient time series. Thus the fast (synoptic time scale) transients have a frequency range corresponding to periods between 2 and 10 days, while the slow transients (low-frequencies) have periods from 10 to 120 days. In this process the eddies with periods shorter than 2 days are removed.

It should be noted that the separation of the transients into the low-frequency and synoptic-scale is done by means of a Fourier filter, which has a sharp separation of periods at 10 days, as is different from digital filters (e.g., Blackmon, 1976) which tend to have less sharp spectrum response curves.

2.2.2 Low-frequency variations of temperature tendencies

A variable which contains a time-mean and transients with periods between 2 and 120 days can be decomposed into three parts corresponding to three frequency bands, i.e.

$$X = \overline{X} + X_l + X_h, \tag{2.1}$$

where the overbar represents the time mean and the subscripts l and h denote the low- and high-frequency projections of the time series, respectively. The three parts are orthogonal to each other because of the Fourier decomposition, thus

$$\overline{X_l X_h} = 0. \tag{2.2}$$

For the product of two variables, X and Y, we have similar relations:

$$\overline{X_l Y_h} = \overline{X_h Y_l} = 0. \tag{2.3}$$

We start with the thermodynamic energy equation in the form of

$$\frac{\partial T}{\partial t} = -\mathbf{V} \cdot \nabla T - \omega\left(\frac{\partial T}{\partial p} - \frac{RT}{c_p p}\right) + Q, \tag{2.4}$$

where T is temperature, t time, p pressure, $\mathbf{V}$ the horizontal velocity component, ω the vertical component of velocity in pressure coordinates, c_p is the specific heat at constant pressure, R is the gas constant for dry air and Q is the diabatic heating rate in units of degrees per unit time.

By decomposing the time-dependent variables in (2.4) into the form of (2.1) and then doing time average, we obtain the equation for the temperature tendency of the time-mean flow:

$$\frac{\partial \overline{T}}{\partial t} = -\nabla \cdot (\overline{\mathbf{V}_h T_h}) - \nabla \cdot (\overline{\mathbf{V}_l T_l}) + \mathcal{A} + \mathcal{B} + \mathcal{D} + \overline{Q}, \tag{2.5}$$

where

$$\mathcal{A} = -\overline{\mathbf{V}} \cdot \nabla \overline{T};$$

$$\mathcal{B} = -\overline{\omega}(\frac{\partial \overline{T}}{\partial p} - \frac{R\overline{T}}{c_p p});$$

$$\mathcal{D} = -(\frac{\partial}{\partial p} - \frac{R}{pc_p})(\overline{\omega_h T_h} + \overline{\omega_l T_l}).$$

The first two terms on the right-hand side of (2.5) represent the convergence of horizontal heat flux by transients, which are interpreted as the contributions to the time tendency from the high- and low-frequency transients, respectively. The term $\mathcal{A}$ represents temperature advection by the time-averaged horizontal flow; and term $\mathcal{B}$ is the effect of time mean vertical motions in advecting heat and in producing temperature changes due to adiabatic processes. The effects of vertical heat flux by transient eddies are included in term $\mathcal{D}$.

Similarly, the temperature tendency of the low-frequency transients can be expressed as:

$$\frac{\partial T_l}{\partial t} = \mathcal{A}_l + \mathcal{B}_l + \mathcal{C}_l + \mathcal{D}_l + Q_l, \tag{2.6}$$

where

$$\mathcal{A}_l = -\overline{\mathbf{V}} \cdot \nabla T_l - \mathbf{V}_l \cdot \nabla \overline{T};$$

$$\mathcal{B}_l = -\overline{\omega}(\frac{\partial T_l}{\partial p} - \frac{RT_l}{c_p p}) - \omega_l(\frac{\partial \overline{T}}{\partial p} - \frac{R\overline{T}}{c_p p});$$

$$\mathcal{C}_l = -\nabla \cdot (\mathbf{V}_h T_h)_l - \nabla \cdot (\mathbf{V}_l T_l)_l - \nabla \cdot (\mathbf{V}_h T_l + \mathbf{V}_l T_h)_l;$$

$$\mathcal{D}_l = -(\frac{\partial}{\partial p} - \frac{R}{pc_p})(\omega_h T_h + \omega_l T_l + \omega_h T_l + \omega_l T_h)_l.$$

Term $\mathcal{A}_l$ is the horizontal temperature advection representing the thermal interaction between the low-frequency flow and the time-averaged flow; term $\mathcal{B}_l$ is the adiabatic effect and temperature advection due to the vertical motion; term $\mathcal{C}_l$ represents the contributions of the horizontal heat transports by the synoptic-scale and low-frequency eddies and by the interactions between the high- and low-frequency flow; term $\mathcal{D}_l$ is the effect of the vertical eddy transports also by the synoptic-scale and low-frequency eddies, and by the interactions between the high- and low-frequency flow. Q_l is the low-frequency component of the diabatic heating in units of degrees per unit time.

It is seen that the contribution to the time tendency of the low-frequency temperature due to the interactions between the low- and high-frequency transients are included in terms $\mathcal{C}_l$ and $\mathcal{D}_l$. We will discuss these terms in detail in the next sections.

2.3 The eddy heat flux convergence and its relation with the time-mean temperature field

Using the similar time-averaged thermodynamic energy equation as (2.5), Lau (1979) diagnosed the local balance of heat at 1000 and 700 hPa. It was argued that the term $\mathcal{D}$ is much smaller than the other terms and can be neglected in the heat balance. A strong correspondence between the patterns of eddy heat flux convergence and the time-averaged temperature field was found. The strong convergences of heat fluxes by transient eddies over northeast Asia and northeast Canada act to dissipate the local cold temperature anomalies.

Here we reconstruct the relationship between the time-mean temperature field and the eddy heat flux convergence using the present data set, in order to compare with the results in the later sections.

Shown in Fig. 2.1a is the familiar distribution of the 700 hPa temperature field averaged for the five winters. It is seen that associated with the two major troughs located along the east coasts of Asia and North America, there are cold anomalies over the eastern parts of the two major land masses. The maximum north-south temperature gradients are observed along about 40°N, south of the two major troughs. It is in these regions that the atmosphere has strong baroclinicity. The temperature variability associated with the synoptic-scale eddies (Fig. 2.1b) is characterized by elongated bands of large standard deviations in the regions of the two major storm tracks (Blackmon et al., 1984a), a result consistent with the known baroclinic structure of the synoptic eddies.

The time-mean convergence of the horizontal sensible heat flux by the synoptic-scale eddies, $-\nabla \cdot (\overline{\mathbf{V}_h T_h})$, is shown in Fig. 2.2a. Generally, it shows a zonal distribution with the heat flux convergence north of 40°N, and divergence south of it. We note that the maxima and minima straddle the maxima of the synoptic-eddy temperature variance (Fig. 2.1b) in the storm tracks. By warming the regions north and cooling those further south, the synoptic-scale eddies act to reduce the local meridional temperature gradient in a manner similar to a downgradient mixing process. Fig. 2.2a provides qualitatively the same temperature tendency distribution as that calculated with the three-dimensional quasi-geostrophic equations by Lau and Holopainen (1984, Fig. 7a). The magnitudes are larger in the present study, presumably because of two reasons: i) the synoptic-scale eddies in the present study are obtained using a Fourier filter retaining eddies with time scale of 2-10 days, while in Lau and Holopainen (1984) they were computed using a 2.5-6 day digital filter, and probably more importantly, ii) the secondary circulation partially offsets the effects due to the heat flux convergence by the synoptic-scale eddies in the study of Lau and Holopainen (1984).

The convergence of heat flux by the low-frequency transients, $-\overline{\nabla \cdot T_l \mathbf{V}_l}$, is presented in Fig. 2.2b. Positive tendencies of the time-mean temperature are observed over the land masses where the wintertime temperature is relatively low, while negative tendencies of the time-mean temperature are found over the oceans where the seasonal mean temperature is high. The heat flux convergence by the low-frequency transients is likely to dissipate the zonal temperature gradient. Shown in Fig. 2.2c is

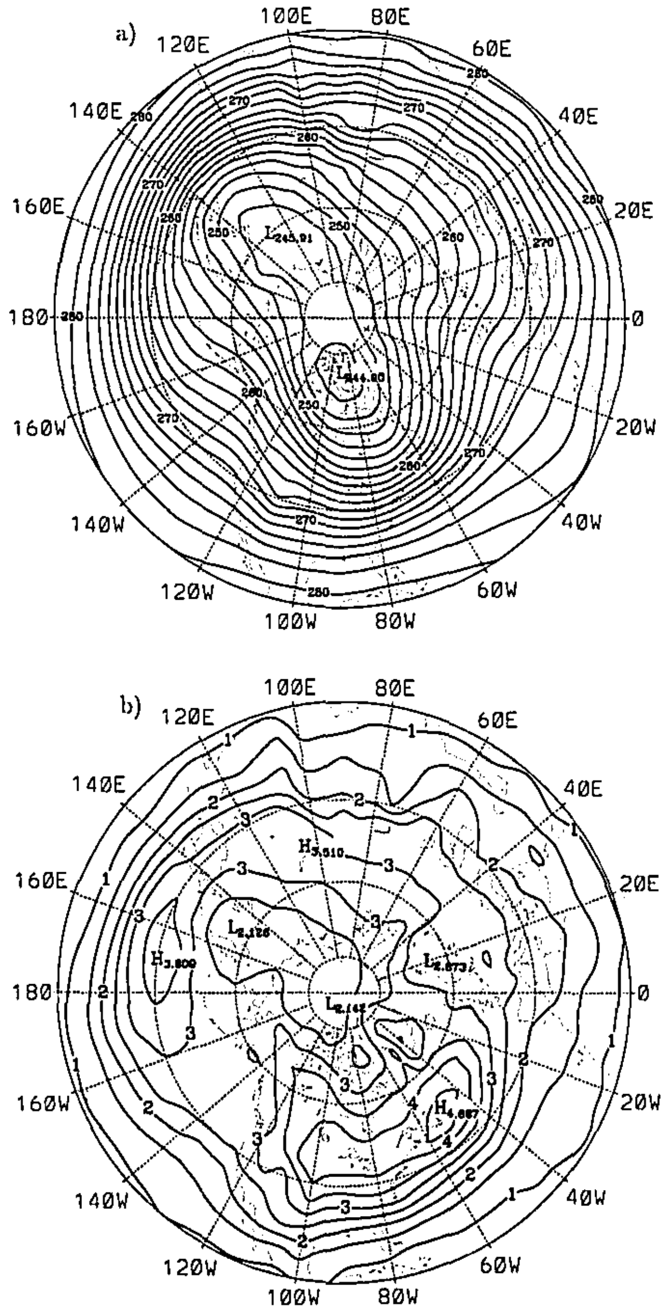

Figure 2.1: Climatology of the 700 hPa temperature in winter. (a) Time-averaged temperature field; (b) Temporal standard deviation of the temperature at 700 hPa associated with the high-frequency transients. Intervals are 2 K for (a) and 0.5 K for (b).

a)

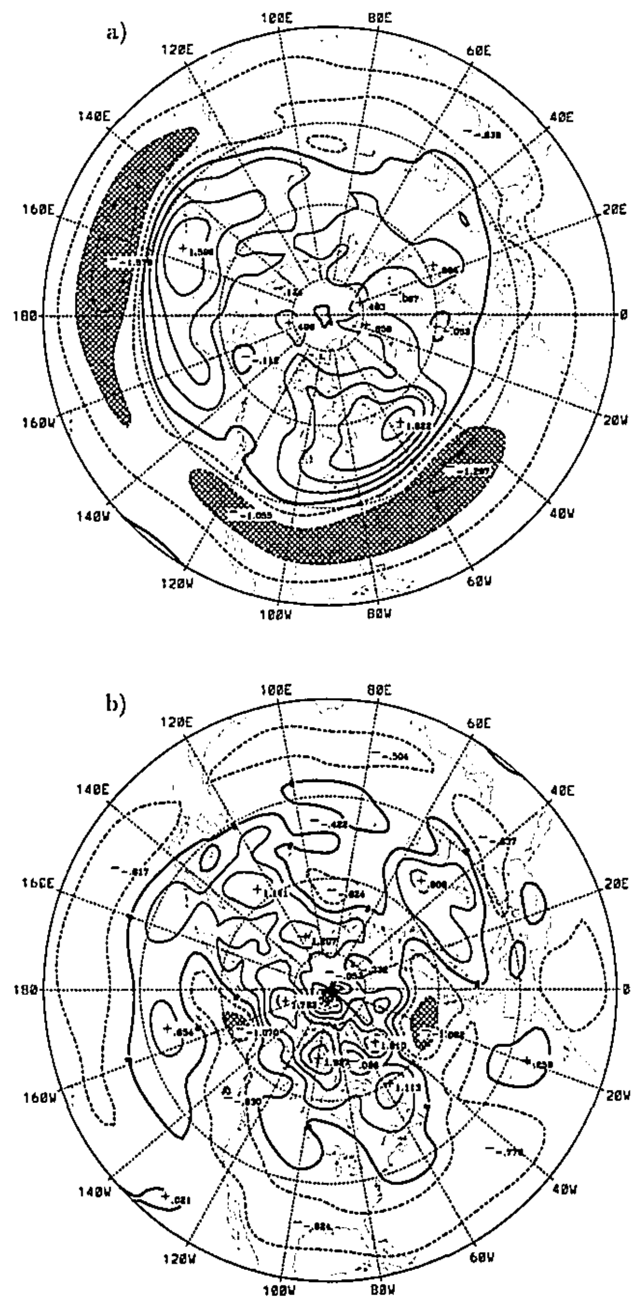

b)

Figure 2.2: Distributions of the time-averaged heat flux convergence due to (a) the synoptic-scale eddies, $-\nabla \cdot \overline{\mathbf{V}_h T_h}$; (b) the low-frequency transients, $-\nabla \cdot \overline{\mathbf{V}_l T_l}$; and (c) the total transients. Intervals are 0.4 K day^{-1}.

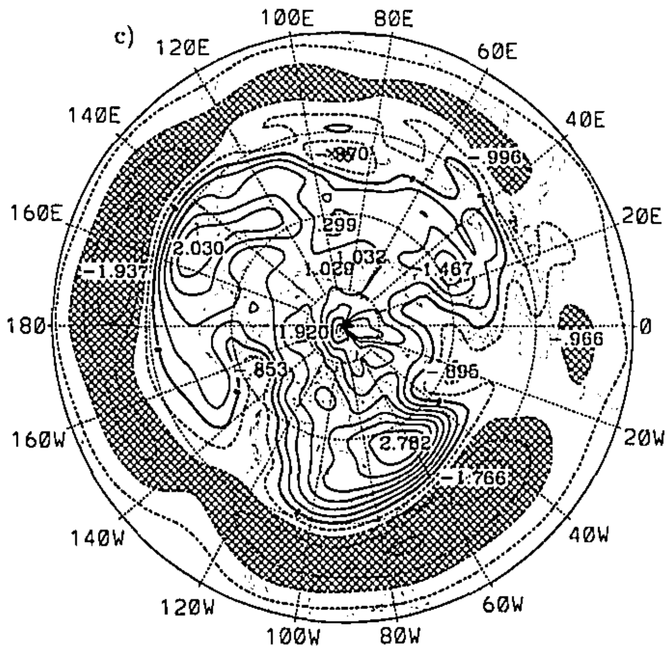

Figure 2.2: Continued.

the convergence of heat flux by the total transients. The distribution looks similar to Fig. 2.2a, indicating that the effect of the synoptic-scale eddies is dominant.

It is interesting to note that there is a strong correspondence between the patterns of the eddy heat flux convergence at 700 hPa (Fig. 2.2a and 2.2c) and the time-averaged 700 hPa temperature field (Fig. 2.1a). Strong convergence of heat flux over northeast Asia and northeast Canada acts to dissipate the cold temperature anomalies located in these regions. This relation supports the idea that the heat flux by the synoptic-scale eddies can be parameterized as a simple downgradient mixing process in low-resolution climate models.

2.4 The low-frequency temperature field and its time tendency

In Fig. 2.3 we show the geographical distribution of the temporal standard deviation of the low-frequency temperature during the five winters at 700 hPa. The low-frequency temperature variability maxima are found over the land masses (North America and Siberia), while the values over the oceans are relatively small. As is well known, the low-frequency geopotential height and kinetic energy variations reach their maxima over the oceans. This difference between the thermal and dynamical parts of the flow was also pointed out by Sheng and Derome (1991a) in the distribution of the low-frequency available potential and kinetic energies. The strong low-frequency wind disturbances over the eastern oceans tend to be equivalent barotropic and have weaker temperature fields than the continental disturbances. The low-frequency temperature variability over the continents seems to have no direct connection with the low-frequency variations over the eastern oceans. A likely explanation for the weakness of the low-frequency temperature variance over the oceans is the tendency of the oceans to warm (cool) the cold (warm) air, thus smoothing out the atmospheric temperature contrasts and reducing the possibility of persistent temperature anomalies.

To compare the relative importance of each term in (2.6), their temporal standard deviations are calculated. The standard deviation of $\partial T_l/\partial t$, the low-frequency temperature tendency, is given in Fig. 2.4a. The time derivative is estimated from the filtered low-frequency temperature time series by applying a centred finite difference in time over a period of 24 hours. Like the low-frequency temperature variability (Fig. 2.3), the standard deviation of the time derivative has maxima over the land masses and generally low values over the oceans.

The standard deviations of $\mathcal{A}_l$ and $\mathcal{B}_l$ are shown in Fig. 2.4b and Fig. 2.4c, respectively. In general the maxima of $\mathcal{A}_l$ and $\mathcal{B}_l$ are located near the two storm tracks, implying that the interactions between the low-frequency temperature field and the mean flow is very active in these regions. It is seen that these two terms are

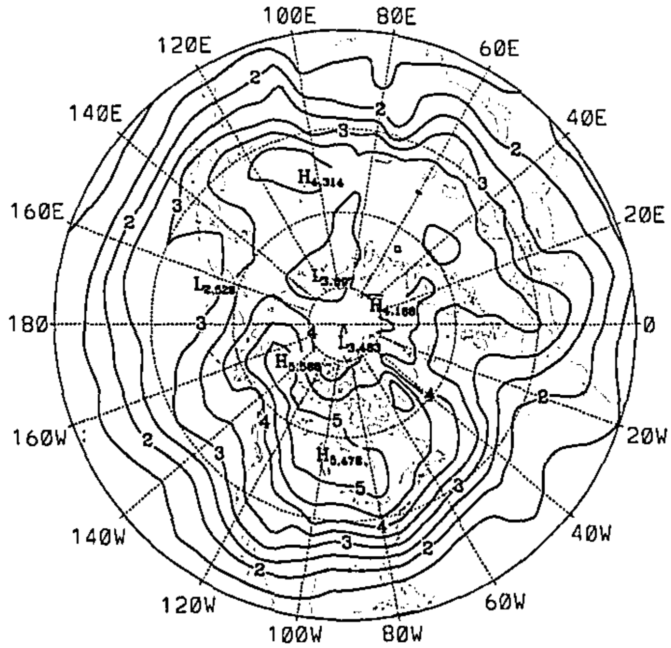

Figure 2.3: Temporal standard deviation of the temperature at 700 hPa associated with the low-frequency transients. The contour interval is 0.5 K.

quite strong when compared with the low-frequency temperature tendency (Fig. 2.4a). However, we will see in the later analyses of the low-frequency temperature variance budget that there is a tendency for cancelation between the effects of $\mathcal{A}_l$ and $\mathcal{B}_l$.

Shown in Fig. 2.4d is the temporal standard deviation of term $\mathcal{C}_l$, which is dominated by $-\nabla \cdot (\mathbf{V}_h T_h)_l$, the low-frequency heat flux convergence by the high-frequency eddies. The most notable features shown in the diagram are the strong centres close to the regions of the maximum synoptic-scale temperature variance (Fig. 2.1b), that is, over the storm tracks. Note that the centres do not coincide with the maxima of the standard deviation of the low-frequency temperature variability (Fig. 2.3). There is also a third maximum near 60°E, 60°N, where the time-mean heat flux convergence by the synoptic-scale eddies does not show large values (Fig. 2.2a). The standard deviation shown in Fig. 2.4d is comparable with that of the time-mean heat flux convergence by the synoptic-scale eddies as shown in Fig. 2.2a.

When the standard deviation of the low-frequency temperature tendency $\partial T_l/\partial t$

a)

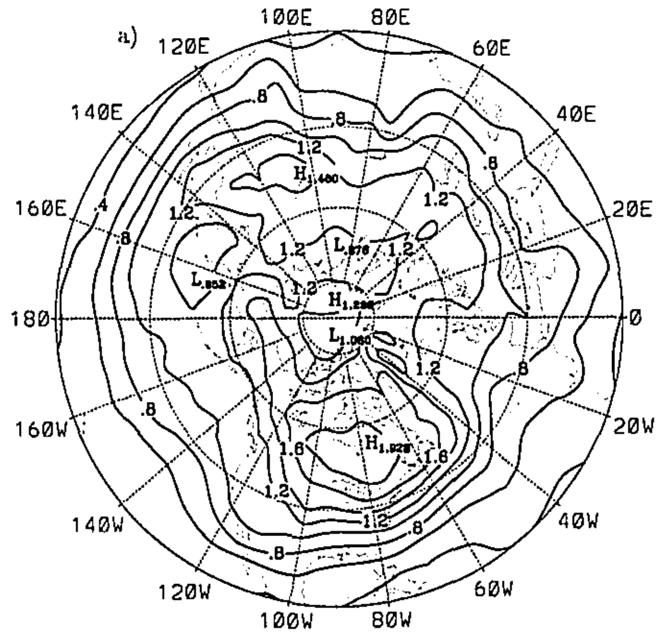

b)

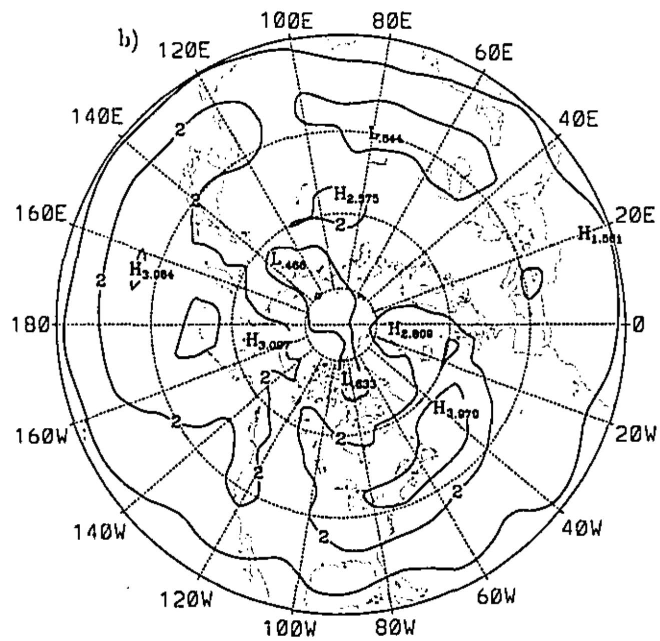

Figure 2.4: Distributions of root mean square (rms) of (a) $\partial T_l/\partial t$; (b) $\mathcal{A}_l$; (c) $\mathcal{B}_l$; and (d) $\mathcal{C}_l$. Intervals are 0.2 K day^{-1} for (a) and (d), and 1 K day^{-1} for (b) and (c).

c)

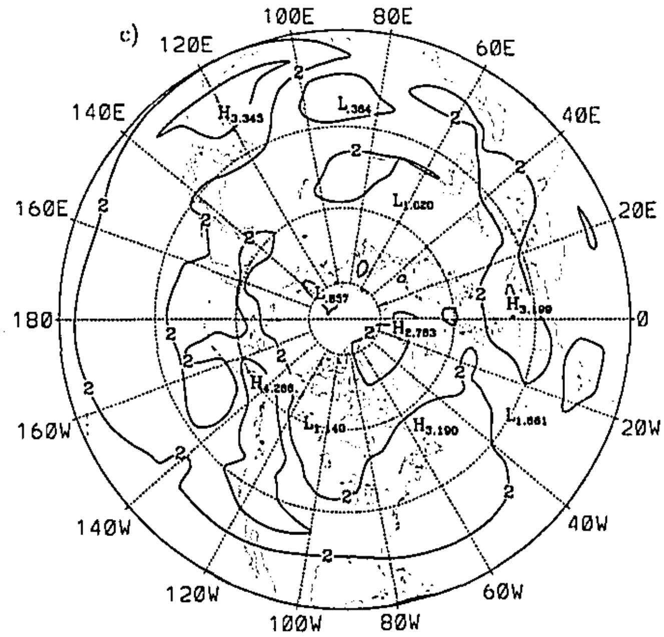

d)

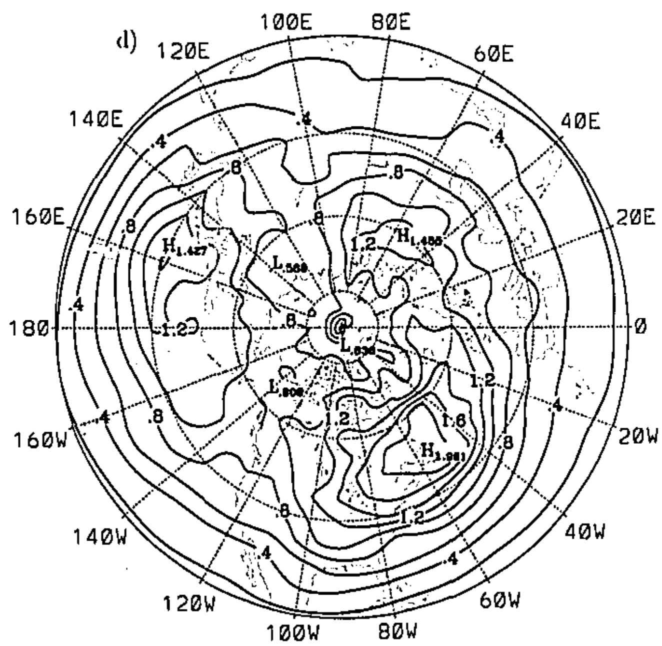

Figure 2.4: Continued.

(Fig. 2.4a) is compared with that of $-\nabla \cdot (\mathbf{V}_h T_h)_l$ (Fig. 2.4d), the maxima are found at about the same latitudes, and their magnitudes are comparable. It is interesting to note that the maximum amplitudes in the low-frequency temperature tendencies over North America and Siberia are located to the west of the maxima in $-\nabla \cdot (\mathbf{V}_h T_h)_l$ near the two major storm tracks. In other words, the maximum thermal interaction between the low-frequency temperature field and the synoptic-scale eddies reaches a maximum downstream of the maximum low-frequency temperature variability. We will see later that on average the synoptic-scale eddies tend to dissipate the low-frequency thermal variability, but in view of the above spatial phase difference, the effect of the synoptic-scale eddies on the low-frequency temperature is not a straightforward mixing process. This feature makes the parameterization of the $-\nabla \cdot (\mathbf{V}_h T_h)_l$ in terms of the low-frequency temperature field a more complex problem than the parameterization of the time average of $-\nabla \cdot (\mathbf{V}_h T_h)$ in terms of the time-mean temperature.

The standard deviation of term $\mathcal{D}_l$ is relatively small, with the maxima near the storm tracks of the order of 0.1K/day (not shown). Indeed this term is negligible.

2.5 Correlation study

Because the eddy heat flux convergence by the synoptic-scale eddies contributes to the net temperature tendency of the low-frequency flow (equation (2.6)), it may be tempting to refer to it as a "forcing" of the low-frequency variability. It must be recognized, however, that it is not clear *a priori* whether the heat flux convergence by the fast eddies leads to, or results from, the low-frequency fluctuations. Clearly, it would be of interest to determine whether a temporal phase lag exists between the two processes, in which case it would appear reasonable to view the leading process as "forcing" the other. In this section we look at the phase relationship between the heat flux convergence by the high-frequency eddies and the fluctuations in the low-frequency temperature.

Fig. 2.5 shows the lag-correlation coefficient fields between the low-frequency temperature and the heat flux convergence by the high-frequency eddies. The time lags are shown from -4 to $+4$ days at intervals of 2 days, with positive lags indicating the heat flux convergence leading the low-frequency temperature. The correlation coefficient at each grid point is first computed for individual seasons and then averaged over the 5 winters. The correlation coefficients shown in Fig. 2.5 have been multiplied by 100, so they represent the percentage values. Regions with strong negative correlations ($< -20\%$) are shaded.

On the simultaneous correlation map (lag 0, Fig. 2.5c), it is seen that in most of the middle and high latitudes the correlation coefficients are negative, indicating that the heat flux convergence by the synoptic-scale eddies is destroying the low-frequency temperature variability. However, the negative correlation centres do not coincide with the maximum standard deviations of the low-frequency temperature over the land masses. Instead, belt-like structures are found for the maximum negative correlations along the two major storm tracks. This suggests that the most effective dissipation of the low-frequency temperature by the eddy heat flux occurs along the storm tracks to the south and east of the low-frequency temperature field (Fig. 2.3). This will be confirmed in Section 2.7 on the thermal variance budget. From the energetics point of view, this implies that the strongest contribution to the transfer of available potential energy from the low-frequency transients to the high-frequency transients occurs in the storm track regions.

By viewing the correlation maps at different time lags (Fig. 2.5), we can get some sense of the phase relationship between the thermal forcing and the low-frequency temperature flows. From Fig. 2.5a (lag -4 days), we see no strong correlations in the entire Northern Hemisphere, although negative correlations appear in most of the middle and high latitudes. At lag -2 days (Fig. 2.5b), the negative correlations start intensifying over the storm track regions and the northern Atlantic and Pacific oceans. The negative correlation centres reach their maximum and become well organized at zero lag (Fig. 2.5c). The negative correlations are then reduced at lag $+2$

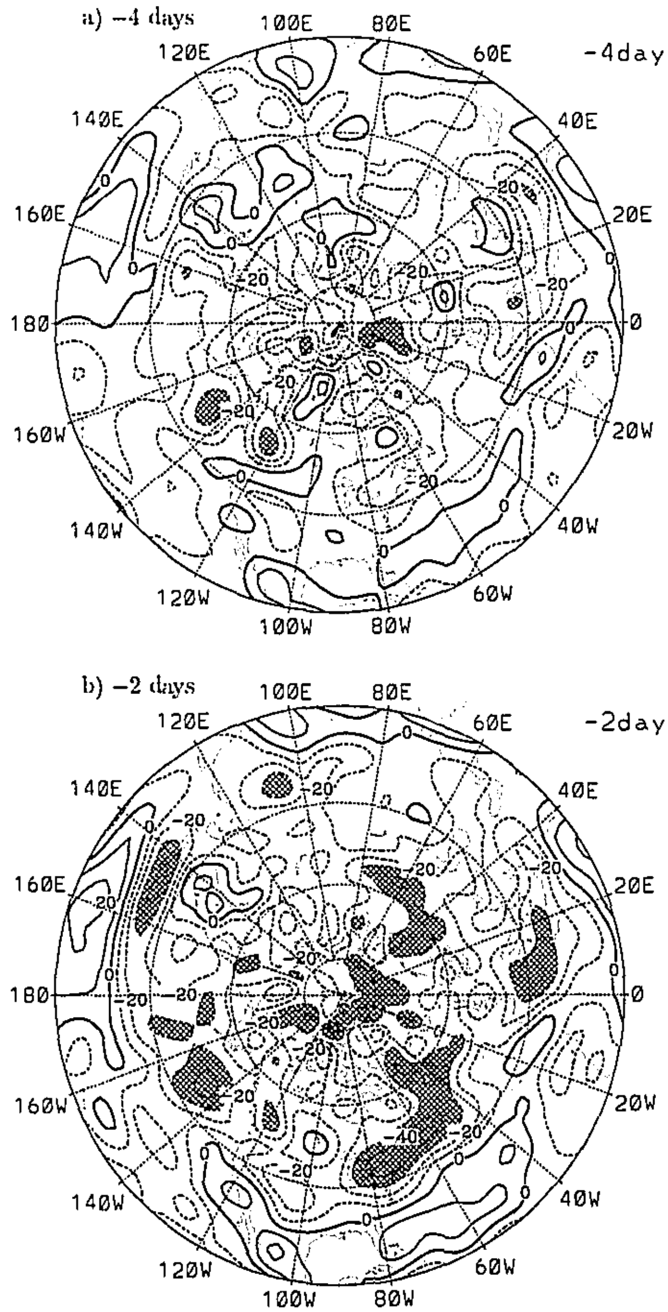

Figure 2.5: Distributions of correlation coefficients between the low-frequency T_l and $-\nabla \cdot (\mathbf{V}_h T_h)_l$ for time lags (a) −4 days; (b) −2 days, (c) 0 days; (d) +2 days; and (e) +4 days. Positive lags indicate that the phase of $-\nabla \cdot (\mathbf{V}_h T_h)_l$ is leading that of T_l. Interval 10%. Regions with values less than −30% are shaded.

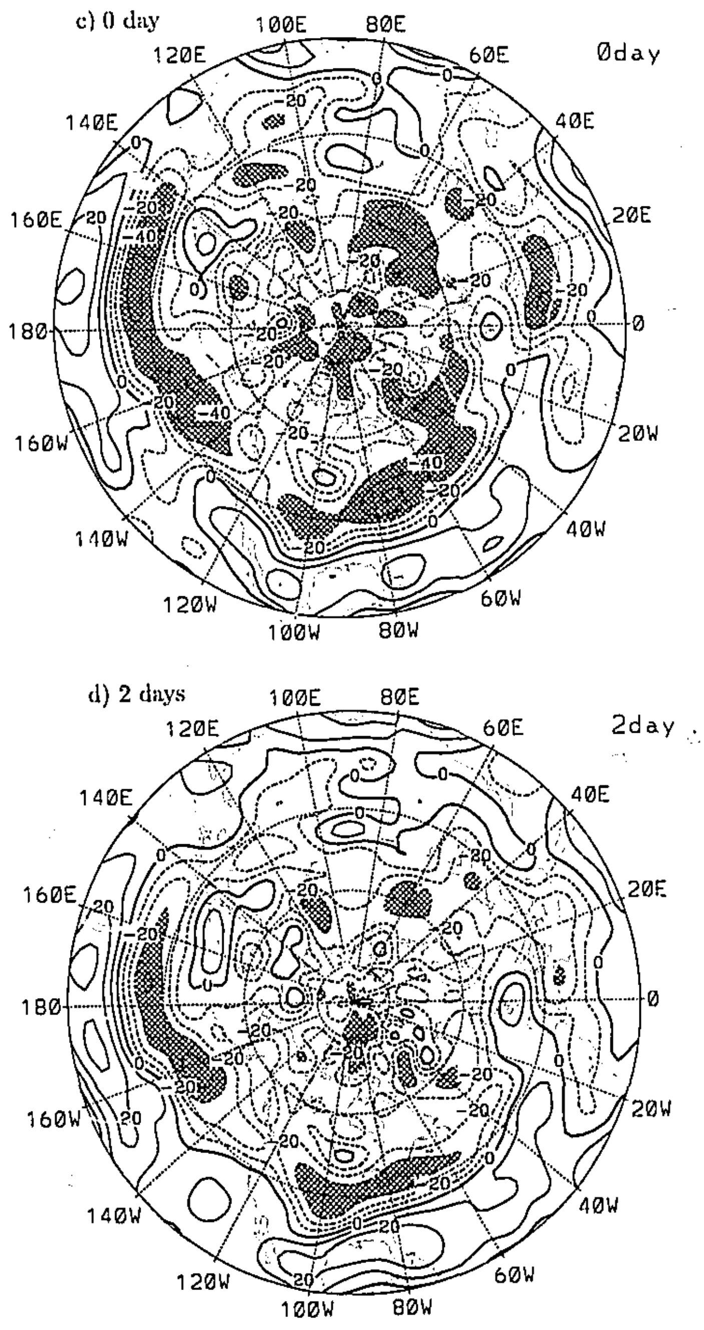

Figure 2.5: Continued.

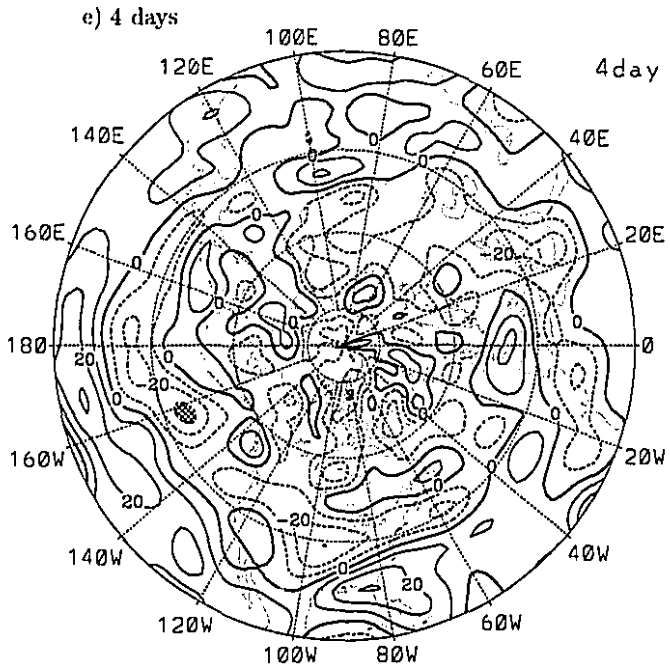

Figure 2.5: Continued.

days (Fig. 2.5d) and become weak at lag +4 days (Fig. 2.5e). The values of the correlations are seen to be strong functions of the lag, but the positions of the maximum correlations are not.

The significance test of the correlation coefficients is conducted as in Sheng and Derome (1993). The effective number of degrees of freedom, n_{eff}, which enters the significance test is determined by the following relation:

$$n_{eff} = \frac{n}{n_0}, \tag{2.7}$$

where n is the length of the time series, and

$$n_0 = 1 + 2\sum_{k=1}^{L}[1 - \frac{k}{L}]R_x(k)R_y(k).$$

$R_x(k)$ and $R_y(k)$ here are the autocorrelation coefficients of time series x and y at lag k, respectively. n_0 is calculated with $L = 40$ for every grid point. For $x = T_l$

and $y = -\nabla \cdot (\mathbf{V}_h T_h)_l$, the values of n_0 within the domain are smaller than 20. For a conservative estimate we set $n_0 = 20$ and a total of 60 effective degrees of freedom is obtained. At the confidence levels of 10% and 1%, the threshold values for the correlation coefficients are 0.21 and 0.32, respectively.

To determine more precisely the relation between the low frequency temperature changes and the eddy heat flux convergence, we present in Fig. 2.6 the correlation coefficients averaged over the areas with maximum negative values in the western Pacific and the western Atlantic oceans shown in Fig. 2.5c. The areas are $80°W - 40°W, 40°N - 50°N$ in the Atlantic, and $140°E - 180°E, 30°N - 40°N$ in the Pacific. It is seen that for both regions the maximum negative correlation occurs at a small time lag (about −0.5 day). The above results suggest that the low-frequency temperature field leads slightly the heat flux convergence by the synoptic-scale eddies. In view of the time scales of the low-frequency temperature, the lag appears to be insignificant.

To provide further information on the spatial and temporal relationship between the low-frequency temperature disturbances and the eddy heat flux convergence by the synoptic-scale eddies, we present here the correlation coefficient in a longitude-time domain. The low-frequency temperature at every longitudinal grid point along a latitudinal circle is correlated with the time series of the eddy heat flux convergence at a base point. The base point is chosen to be at the centre of the area with maximum variability of the eddy heat flux convergence in the western Atlantic and western Pacific as in Fig. 2.4d. The time series generated for the Atlantic base point is that of the eddy heat flux convergence averaged over the area of 45°–55°N, 50°–70°W, while the time series for the Pacific base point is that averaged over the area of 35°–45°N, 150°–170°E. The low-frequency temperature at every longitudinal grid point along the latitudinal circle is the average of temperature for the latitudinal band, i.e., 45°–55°N for the Atlantic and 35°–45°N for the Pacific. Fig. 2.7a and 2.7b show the longitude-time correlations for the Atlantic and the Pacific base points, respectively. The diagrams are centred at the base points, with time lags increasing downward and longitude lags increasing to the right. The negative lags in time or in longitude

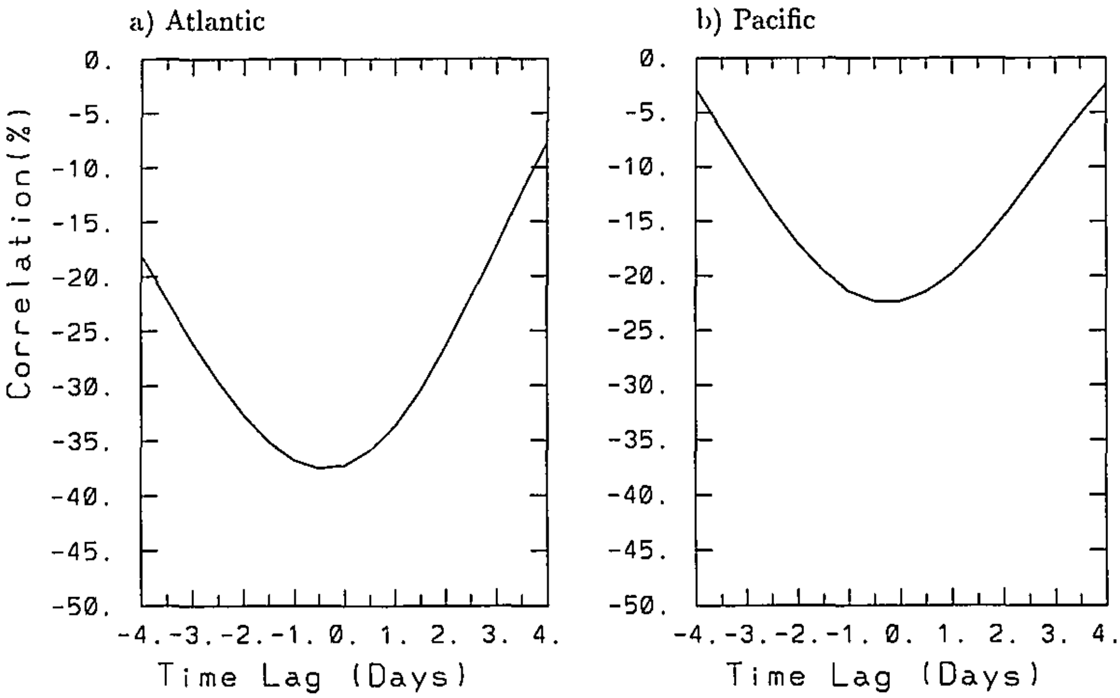

Figure 2.6: Correlation coefficients between T_l and $-\nabla \cdot (\mathbf{V}_h T_h)_l$ as a function of the time lag for (a) the Atlantic region and (b) the Pacific region.

indicate the low-frequency temperature leading the heat flux divergence. The time lag of the maximum negative correlation is such that in the Atlantic the temperature field leads the eddy heat flux convergence by about 1.5 days, while in the Pacific the lead time is a mere 0.5 day. We note also that over both oceans the low-frequency temperature is best negatively correlated with the heat flux convergence a few degrees to the east. In view of the space and time scales of the low-temperature field, these temporal and spatial lags are very small indeed.

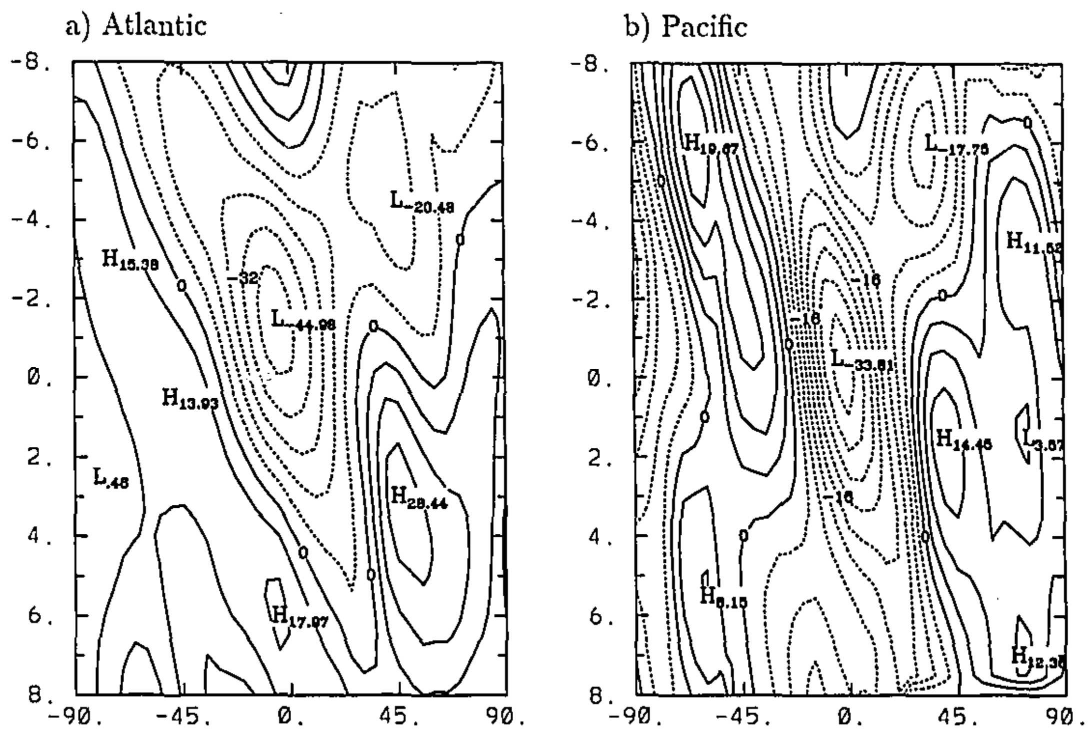

Figure 2.7: Correlation coefficient between T_l and $-\nabla \cdot (\mathbf{V}_h T_h)_l$ as a function of longitude and time lags for: a) Atlantic basepoint; b) Pacific basepoint.

2.6 Regional structures of low-frequency temperature patterns and the eddy heat flux convergence

We have seen that the geographic distribution of the eddy heat flux convergence differs from those of the low-frequency temperature field. The effect of the eddy heat flux convergence on the low-frequency temperature field is not simply dependent on the temperature, and thus not a simple mixing-type damping process. The damping effect is at least not a simple linear function of the Laplacian of the temperature field. On the other hand, from the above section it is seen that the low-frequency temperature field is indeed negatively correlated with the eddy heat flux convergence with little time and space lags. It seems that the damping effect of the eddy heat flux is not horizontally homogeneous, and different temperature patterns have different dampings. To identify the main spatial patterns of the low-frequency temperature field and their relationship with the eddy heat flux convergence, we proceed to an empirical orthogonal function (EOF) analysis. From such an analysis we obtain a set of eigenvectors (the spatial patterns) and temporal coefficients which account for a substantial fraction of the variance of the dataset. Here the EOF analysis is performed on T_l, the low-frequency temperature field. As known from Section 2.4, the maximum variability of the low-frequency temperature occurs over the land mass regions. To focus on the structure of the regions where the low-frequency temperature reaches maximum variability, the EOF analysis is performed separately for the East Asian and North American sectors. Each sector ranges from $20°N$ to $70°N$, and has a longitudinal span of 120 degrees. The East Asian sector extends from $60°E$ to 180°, whereas the North American sector extends from $140°W$ to $20°W$. In each sector 143 grid points are used with a resolution of 5° latitude by 10° longitude. The effect of unequal areas represented by different grid points is taken into account by multiplying T_l by the square root of the cosine of latitude at that grid point.

In Figs. 2.8, the spatial distributions of the three leading eigenvectors are shown for the East Asian and North American sectors. The percentage of variance explained by each mode is given at the top of each panel. The first three EOFs for the East Asian and North American sectors are denoted EA1, EA2, EA3, and AM1, AM2 and AM3, respectively. The first three eigenvectors collectively account for 43.36% of the total variance in the East Asian domain, and 48.67% in the North American domain.

The first eigenvectors for the two domains are characterized by a large pattern centred over the land masses. Not surprisingly, the EA1 and AM1 modes have shapes that are similar to those of the rms of low-frequency temperature over the two regions shown in Fig. 2.3.

The eigenvectors EA2 and AM3 are characterized by a dipole structure with the pair of extrema straddling the climatological storm track axes. The locations of the

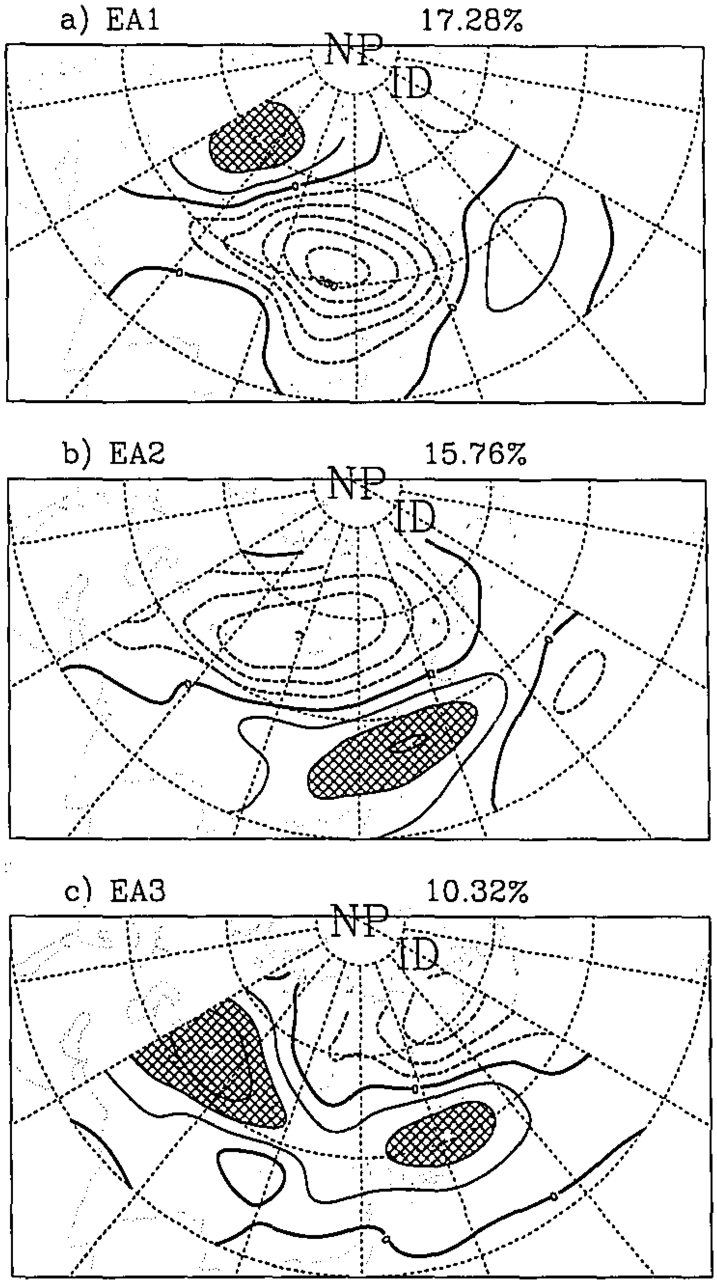

Figure 2.8: Distributions of the three leading eigenvectors of T_l for (a), (b) and (c) the East Asia; and (d), (e) and (f) the North America sectors. Extrema for negative areas are shaded. The percentage of variance explained by each eigenvector is indicated at the top of the corresponding panel. Arbitrary units.

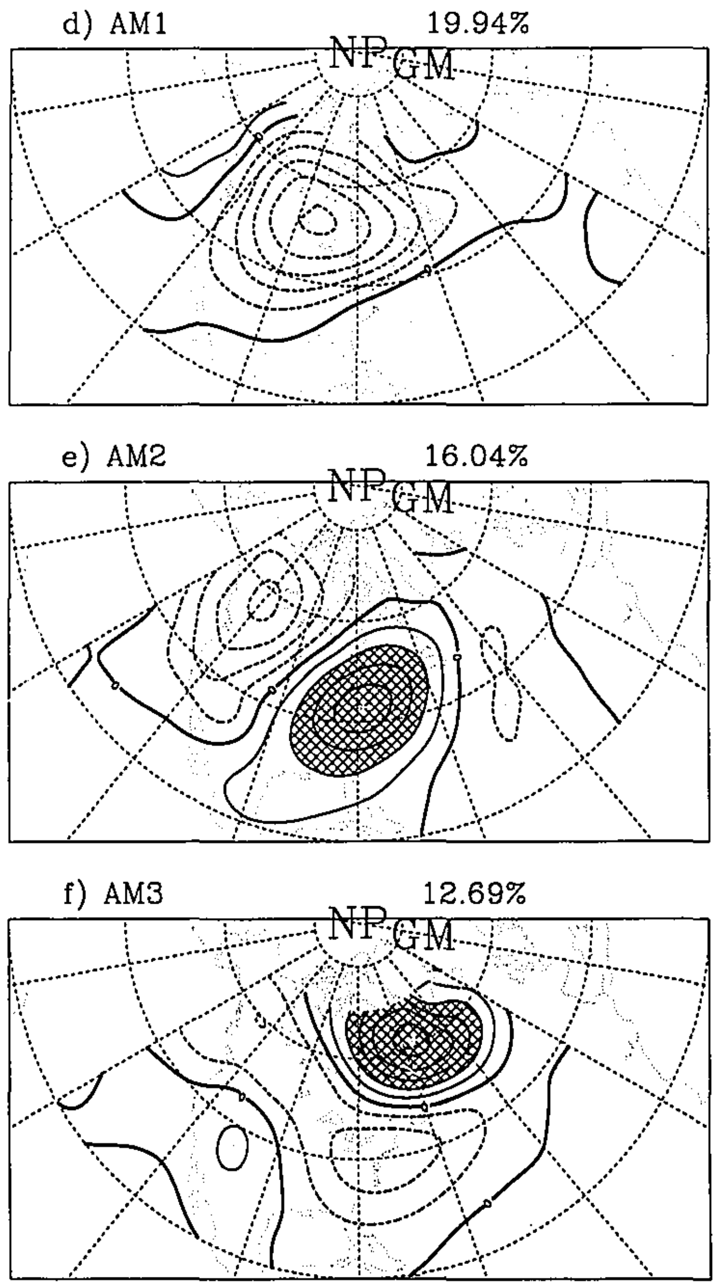

Figure 2.8: Continued.

maximum gradients of these modes correspond closely with the time-mean positions of the 700 hPa temperature gradients (Fig. 2.1). Thus these eigenvectors reflect the fluctuations in the intensity of the 700 hPa temperature gradient about the time mean, with little change in position.

The AM2 pattern has a well defined east-west dipole structure corresponding to persistent temperature anomalies of opposite signs on the east and west coasts of North America. The EA3 pattern, which represents only 10.3% of the variance, has a more complex structure, corresponding mainly to meridional fluctuations in the meridional temperature gradient, in particular over the east coast of the continent.

In summary, the first eigenvectors for the two domains are associated with the low-frequency variation of temperature only in the inland areas. The temperature fluctuations near the storm tracks, over the east coasts, are associated with the second and third modes.

In general the structure of an EOF mode exhibits large intersample variability when its eigenvalue is close to that of another mode. North et al. (1982) provided an estimate of the sampling errors of EOF analysis. Because an eigenvalue can be seen as the portion of the total variance explained by its associated EOF mode, we use here the percentage variance explained by each mode σ to evaluate the sampling errors. This sampling error is expressed as:

$$\delta\sigma = \sigma(2/N)^{\frac{1}{2}}, \tag{2.8}$$

where N is the size of the sample, which is 1200 in our case. If the sampling error is larger than or comparable to the difference between σ and the percentage variance of a neibouring EOF mode, the two modes may be close enough for mixing to occur, i.e. different samples may lead to different linear combinations of the nearby eigenvectors.

In Fig. 2.9 we show the percentage variance explained by each mode with error bars indicative of the sampling error $\pm\delta\sigma$ for the East Asian and North American sectors. We see that the first three leading modes in North American region are well separated. The first two Asian modes, on the other hand, while still resolved, are less well separated.

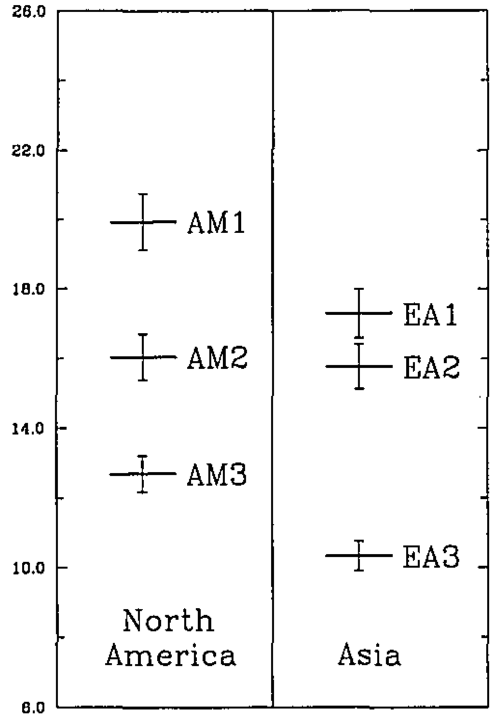

Figure 2.9: Schematic diagram of the percentage variance explained by each EOF for East Asia and North America sectors. The error bars represent one standard deviation error due to sampling.

In order to discern the spatial structure of the heat flux convergence by synoptic-scale eddies associated with the individual EOF modes of the low-frequency temperature shown above, regression patterns were constructed following Nakamura et al. (1987). For a given low-frequency temperature pattern P, the corresponding regression pattern is obtained by mapping the distribution of the linear regression coefficients between the temporal coefficients of the EOF associated with P and the eddy heat flux convergence $-\nabla \cdot (\mathbf{V}_h T_h)_l$ values at every grid points. This method provides information on the spatial distribution and the amplitude of the heat flux convergence fluctuations associated with the temperature EOF of interest.

To obtain reasonable amplitudes in the regression maps, a scaling procedure has been applied as in Lau and Nath (1991). To do so, we first construct a composite pattern of the heat flux convergence fields corresponding to 10% of the total data (1200 fields) with the largest positive EOF coefficients for P. Similarly, the composite pattern corresponding to 10% of the total data with the largest negative EOF coefficients is obtained. The difference between these two composite patterns, which describes the swing between the opposite extremes of P, is then calculated. Secondly, we multiply the EOF coefficients for P with a constant scaling factor to make the amplitudes of the resulting regression pattern comparable to the amplitudes on the difference composite map obtained in the first step. In fact the spatial patterns of the difference composite map and the regression map look very similar to each other even before any scaling is applied, so the scaling factor can be easily determined using representative ratio between the collocated extrema in these two maps. This procedure is applied separately for each pattern shown in Fig. 2.8.

Fig. 2.10a, b and c show the regression patterns of the coefficients of the EA1, EA2 and EA3 modes versus the heat flux convergence fields at 700 hPa over the Eurasian–Western Pacific area. The regression maps are associated with the positive phases of the EOF modes shown in Fig. 2.8. In general the heat flux convergence regression patterns are out of phase with the low-frequency temperature EOF patterns, which is consistent with the simultaneous correlation map shown in Fig. 2.5. The regression patterns for the North American region appear in Fig. 2.10d, e and f, and show qualitatively a similar negative relationship between the temperature field and the heat flux convergence as in Asia.

One interesting result emerges from the comparison of EOF patterns of the low-frequency temperature and the regression patterns with the eddy heat flux convergence. The regressions associated with the AM2 and AM3 modes are much stronger than that associated with the AM1. The eddy heat flux thus seems to have a smaller damping effect on the first eigenvector, which is of mainly inland structure, than on the second and third eigenvectors, which are associated with the fluctuations of temperature near the east coast (and to some extent over north-west Canada). This may be a useful information if one wants to parameterize the effect of the eddy heat flux

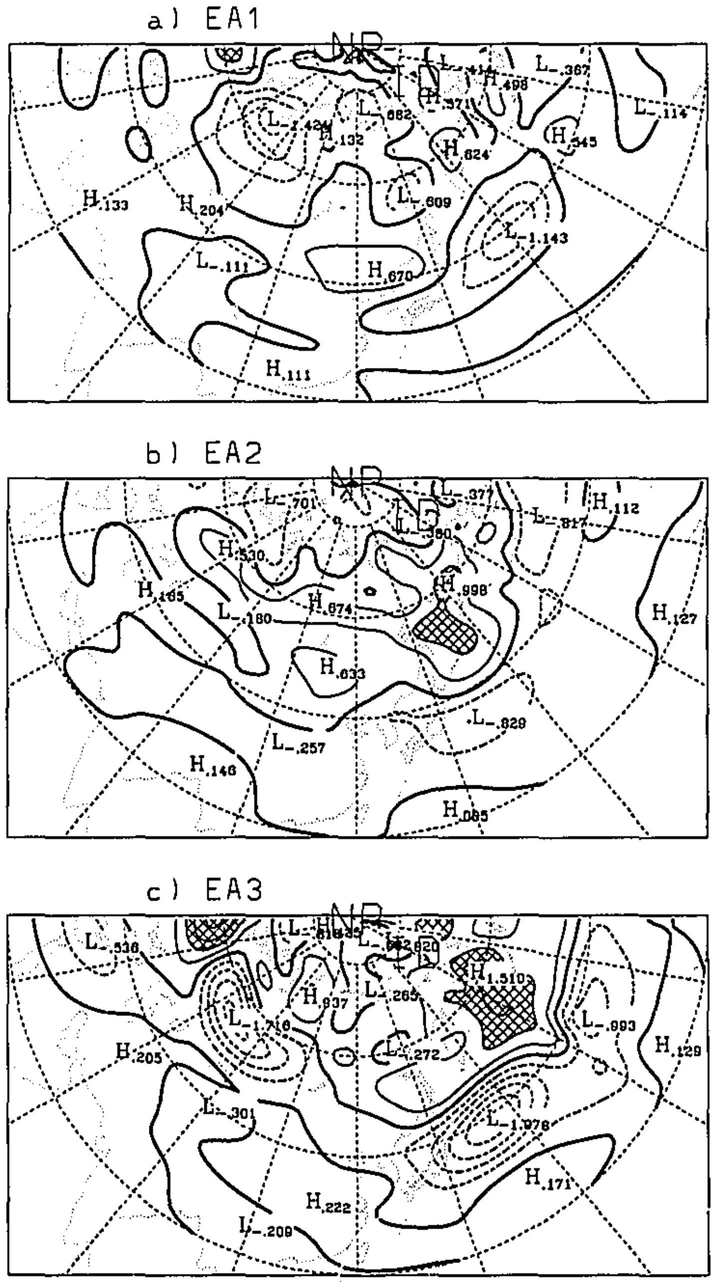

Figure 2.10: Regression patterns of the high-frequency heat flux convergence against each EOF in Fig. 2.8. Interval 0.4 K/day. The negative values are indicated by dashed lines. Areas with values greater than 0.8 K/day are shaded.

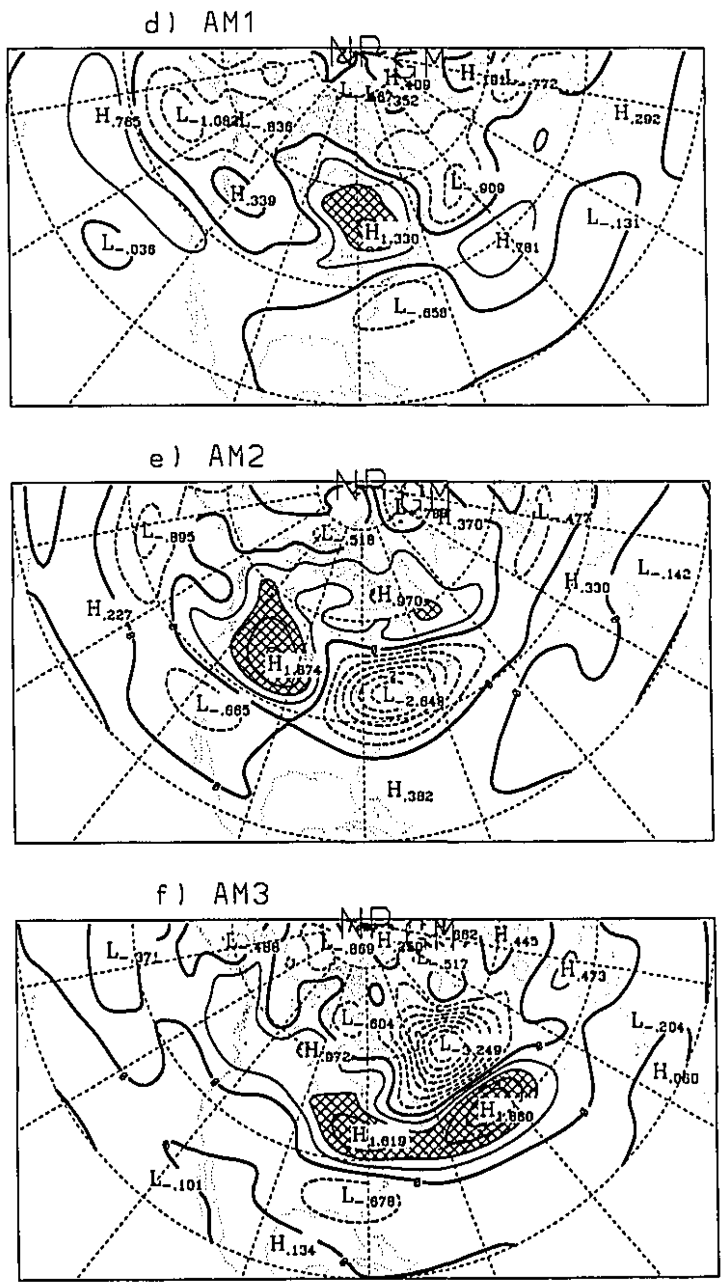

Figure 2.10: Continued.

with the low-frequency temperature field. Similar result can be found for the East Asian region. The amplitude of eddy heat flux convergence associated with EA3 is much stronger than those associated with EA1 and EA2. However there is only small difference between magnitudes on the EA1 regression map and the EA2 regression map. This may be caused by the closeness of EA2 to EA1 shown in Fig. 2.9.

The composite maps (not shown) for the eddy heat flux convergence fields corresponding to each eigenvectors have very similar structures to the regression patterns discussed above, with the extreme centres at exactly the same positions as their regression map counterparts. As was mentioned earlier, the composite maps include information for only a limited number of extreme cases (in our study, 10% of the total data with the largest negative EOF coefficients and 10% with the largest positive coefficients). It seems that the small number of the extreme cases account for the major features of the regression patterns shown in Fig. 2.10.

The out-of-phase relationship between the low-frequency temperature field and the eddy heat flux convergence confirms that the eddy heat flux convergence acts to destroy the low-frequency temperature field. The time scale associated with the dissipative effects can be roughly estimated by computing the ratio of the standard deviation of the low-frequency temperature (Fig. 2.3), to the magnitudes of the heat flux convergence (Fig. 2.4d). The time scale is found to be in a range from about 2 days over the western oceans to about 6 days over the continents. Hence, in the absence of other processes, the maxima in the low-frequency temperature transients would be destroyed by the eddy heat flux convergence in a few days. This estimate is comparable with the 3-7 days time scale given by Lau (1979) for time required for the transient eddy heat flux to dissipate the stationary temperature waves.

2.7 The low-frequency thermal variance budget analysis

We now diagnose the budget equation for the low-frequency thermal variance to see how the low-frequency temperature fluctuations are maintained, and to determine the importance of the eddy heat flux convergence compared with that of other processes.

An equation for the low-frequency thermal variance is obtained by multiplying (2.6) with T_l, the low-frequency component of the temperature, and averaging over time. As discussed in Section 2.4 term $\mathcal{D}_l$ can be neglected. Assuming there is no trend for the time-averaged thermal variance, the budget for the low-frequency thermal variance at a point can be written as:

$$\overline{T_l\mathcal{A}_l} + \overline{T_l\mathcal{B}_l} + \overline{T_l\mathcal{C}_l} + \overline{T_lQ_l} = 0. \tag{2.9}$$

Fig. 2.11a shows the geographical distribution of term $\overline{T_l\mathcal{A}_l}$, which is the covariance of the horizontal advection and the low-frequency temperature. Positive values are found over most of the Northern Hemisphere with maxima over the eastern continental areas. The positive nature of this term implies that as far as horizontal motions are concerned, the interaction of the low-frequency eddies with the time-mean flow is a source of low-frequency temperature variance. This term is dominated by $-\overline{T_l\mathbf{V}_l} \cdot \nabla\overline{T}$, which can be interpreted as the heat flux by the low-frequency transients down the time-mean temperature gradient. Thus over the eastern portions of Asia and North America, and the adjacent oceanic areas, where the largest meridional time-mean temperature gradients are observed, a northward heat transport is required to maintain the low-frequency temperature variance. In other words, since $-\nabla\overline{T}$ has a northward component, $-\overline{T_l\mathbf{V}_l}\cdot\nabla\overline{T}$ will be positive if positive (negative) values of T_l are correlated with low-frequency winds that have a northward (southward) component, which is indeed the case. From the energetics point of view, the advection term can be related to the transfer of available potential energy from the mean flow to the low-frequency disturbances. As was shown by Sheng and Derome (1991a, b), the transfer of available potential energy from the time-mean flow is the only source of available potential energy for the low-frequency transients (except for diabatic processes). The present study reveals that the transfer process occurs mainly over the eastern continental areas and near the climatological positions of the storm tracks.

The distribution of the thermal variance tendency associated with the vertical motion is shown in Fig. 2.11b. Here the dominant contribution comes from $\overline{T_l\omega_l(\frac{\partial T}{\partial p} - \frac{RT}{c_p p})}$. Clearly, the vertical motion term tends to partially offset the effect of $\overline{T_l\mathcal{A}_l}$ through the sinking of the cold air and the rising of the warm air within the low-frequency disturbances. The vertical motion term is related to the conversion of low-frequency available potential energy to kinetic energy and indeed the distribution bears considerable similarity to the AK distribution shown in Fig. 3c of Sheng and Derome (1991a).

Fig. 2.11c shows the distribution of term $\overline{T_l\mathcal{C}_l}$, in which the effect of the synoptic-scale eddies associated with horizontal heat flux $-\overline{T_l\nabla\cdot(\mathbf{V}_hT_h)_l}$ is dominant. The other contributions included in this term, $\overline{T_l\nabla\cdot(\mathbf{V}_lT_l)_l}$ + $\overline{T_l\nabla\cdot(\mathbf{V}_hT_l+\mathbf{V}_lT_h)_l}$, are relatively small. Thus $\overline{T_l\mathcal{C}_l}$ can be related to the exchange of available potential energy between the low and the high frequency eddies. In agreement with the correlation study (Fig. 2.5c) and the regression pattern (Fig. 2.9 and 2.10), the high-frequency eddies make a negative contribution to the low-frequency temperature variance. Again the largest negative values are found along the mean storm track regions, though the dissipative effect in the Pacific region is much weaker than that over the western Atlantic and Eastern North America. The contribution of the high-frequency eddies to the low-frequency temperature variance is seen to be smaller than that of the advection term and the vertical motion term, but is still significant over the eastern part of North America. The small values in the Pacific storm track region may be caused by the short data period, for longer time period the dissipative effect in the Pacific region is comparable to that in the western Atlantic as can be seen from later discussion shown in Fig. 3.12.

Robinson's (1991) study of the thermal variance of the low-frequency oscillations with a two-level primitive equation model yields results in general agreement with

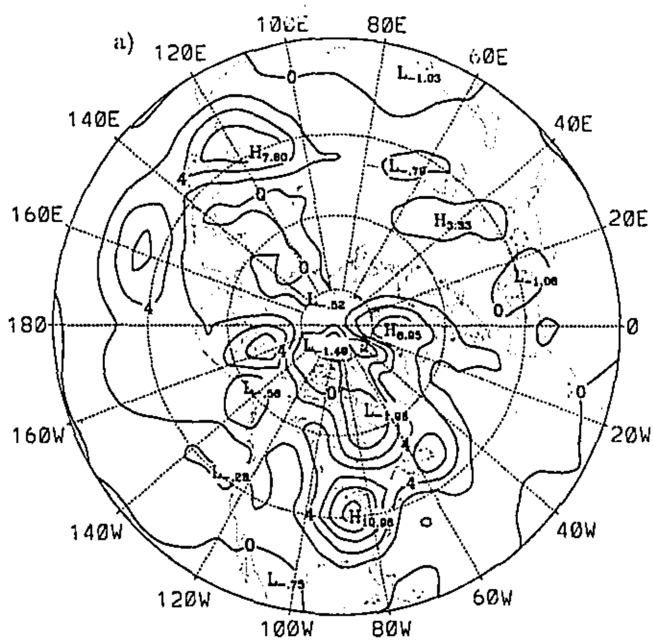

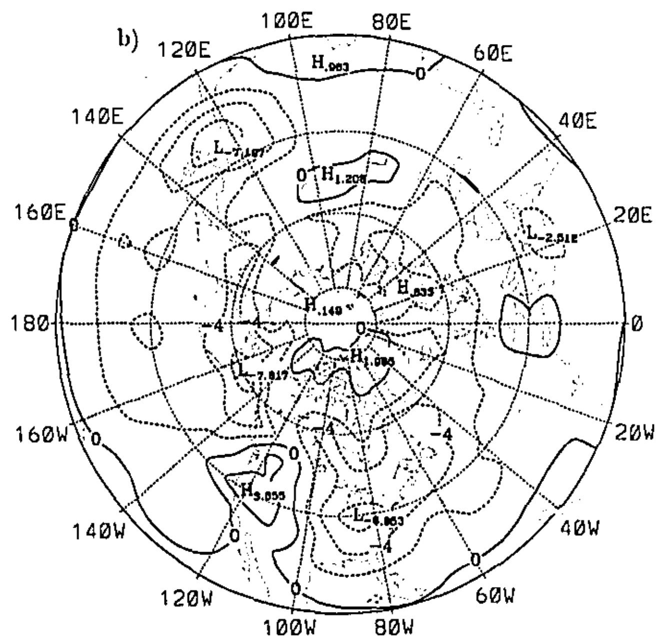

Figure 2.11: Distributions of (a) $T_l\mathcal{A}_l$; (b) $T_l\mathcal{B}_l$, and (c) T_lC_l for the low-frequency temperature variance budget equation (2.9). Interval 2 K^2 day^{-1} for (a) and (b), 1 K^2 day^{-1} for (c). Contours with negative values are dashed.

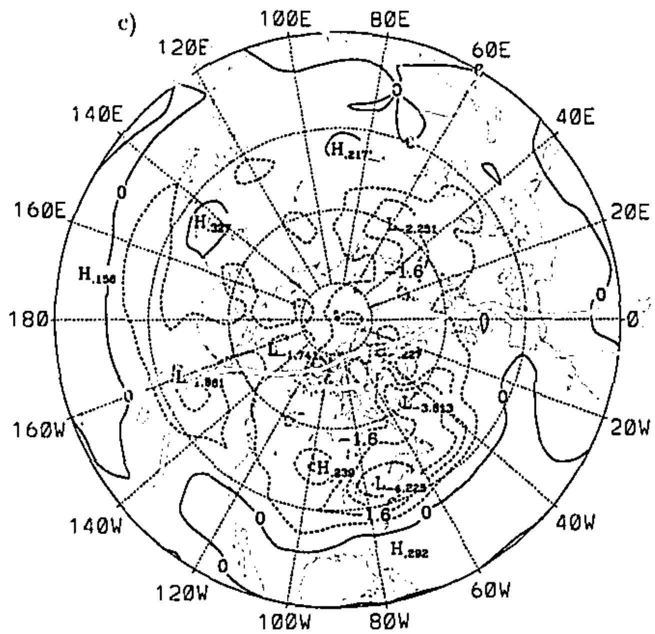

Figure 2.11: Continued.

those of our observational study. His model reproduced: (1) the positive contribution to the variance by the horizontal temperature advection associated with the time-mean flow and the low-frequency fluctuations, and (2) the dissipative effect of the heat flux convergence by the high-frequency eddies.

2.8 Discussion and conclusions

We have analyzed the atmospheric low-frequency temperature variability (periods 10 to 120 days) and its interaction with the higher-frequency synoptic-scale eddies. Calculations have been made for five winters at 700 hPa using Northern Hemisphere data with a 12-hour time resolution.

It was shown that in contrast to the low-frequency height field, which has a maximum variance over the eastern Pacific and Atlantic, the low-frequency temperature field has a maximum variance over the continental land masses of Canada and Siberia. The likely explanation is that the air-sea interactions tend to smooth out the atmospheric temperature field in the lower troposphere, thereby reducing the possibility of maintaining long-lasting temperature anomalies over oceanic areas.

The synoptic-scale eddies interact with the lower-frequency temperature field through the convergence of their heat flux, which has a low-frequency component; in other words, the heat flux convergence by the synoptic-scale eddies gives rise to a low-frequency temperature tendency that represents an interaction between the low and higher frequency components of the flow. That interaction was found to reach a maximum in the storm track regions over eastern North America and eastern Asia, whereas the maximum variance in the low-frequency temperature field itself occurred further to the west, over Canada and Siberia. In spite of this spatial phase difference in the maxima of the two fields, a significant temporal correlation was found between the low-frequency temperature fluctuations and the low-frequency component of the heat flux convergence by the faster synoptic-scale eddies over and to the west of the storm tracks. The correlation is negative, implying that the heat flux by the faster eddies tends to damp the low-frequency temperature fluctuations, just as it does for the time-mean temperature (Holopainen et al., 1982). As the maximum damping effect takes place downstream of the maximum temperature variance, a suitable parameterization of the damping is likely to be appreciably more complex than a simple diffusion mechanism.

The main horizontal structures of the low-frequency temperature have been obtained by an EOF analysis. The first modes in East Asia and North America sectors represent the intensity variation of the temperature field in the regions of its maximum variability. The second and the third eigenvectors are connected with the fluctuations of the storm tracks and with an oscillation in temperature between eastern and western North America. The eddy heat flux divergence has a smaller damping effect on the first eigenvectors than on the second and third eigenvectors.

A budget analysis was made of the low-frequency temperature variance. The results showed that the main contributor to the temperature variance over the eastern North American and Asian continents is the advection process involving the low-frequency heat flux down the time-mean temperature gradient. The vertical motion in the time-mean and low-frequency flows was found to damp the low-frequency temperature, in agreement with Sheng and Derome (1991a, b) who showed that the low frequencies convert potential energy to kinetic energy through the rising of warm air and the sinking of the cold air, clearly an energy conversion that damps the low-frequency temperature field. Finally, the damping of the low-frequency variance by the synoptic-scale eddy heat flux convergence was shown to be the third factor in importance, but still significant over the eastern part of Canada and the western North Atlantic.

Chapter 3

On the Modification of the High- and Low-frequency Eddies during ENSO Years: An Observational Study

3.1 Introduction

The understanding and proper treatment of the dynamics of the low-frequency variabilities is crucial in medium- and long-range weather prediction. The accuracy of mean-seasonal predictions, for example, depends on a proper understanding of the processes responsible for interannual fluctuations in the mean seasonal states, and a proper representation of these processes in the prediction models.

One obvious possible mechanism for the interannual variation of the extratropical atmospheric circulation is some kind of external forcing. Studies of the El Niño/Southern Oscillation (ENSO), for example, have provided strong evidence for the linkage between the anomalous tropical sea surface temperature (SST) and the interannual variability of the extratropical circulation (e.g., Bjerkness, 1966, 1969;

Horel and Wallace, 1981; Lau and Boyle, 1987). One remarkable extratropical signal corresponding to the sea surface temperature increase in the equatorial eastern Pacific in an El Niño year is the Pacific/North American (PNA) teleconnection pattern anomaly. An El Niño event is normally accompanied by below-normal geopotential heights in the North Pacific and the south-eastern United States and above-normal heights over western Canada. This linkage between the tropical SST anomalies and the PNA patterns is supported by modeling studies (e.g., Cubasch, 1985; Lau, 1985) and Rossby wave energy dispersion theory (Hoskins and Karoly, 1981; Branstator, 1985). Similarly, the relation between some northern winter climate anomalies and midlatitude SST anomalies has been observed and simulated (e.g., Palmer and Sun, 1985).

The internal dynamical processes in the atmosphere also play an important role in generating and maintaining the interannual variability. It is well known that significant low-frequency variations (including those on the interannual time scale) can be produced in atmospheric models that neglect all corresponding fluctuations in the external forcings (e.g., Robinson, 1991; Hendon and Hartmann, 1985). Lau (1981) obtained rather realistic low-frequency teleconnection patterns with a GCM model that had no time-dependent external forcing other than the annual solar cycle. The nonlinear interactions among eddies of different time scales in these models are important in determining the low-frequency behaviours. As revealed by observational studies, the synoptic-scale eddies can act as a source of energy for persistent atmospheric anomalies, such as blocking highs (e.g., Mullen, 1987; Shutts, 1983). Similarly, the Pacific/North American (PNA) anomaly pattern was found to be induced and maintained by transient eddy forcing in linear models (Kok and Opsteegh, 1985, Held et al., 1989, Hoerling and Ting, 1994, and Ting and Hoerling, 1993).

The part of the interannual variability that is potentially predictable is likely controlled by the long-lived external forcing, while the "natural" variability caused by the internal processes is probably unpredictable. It is therefore of interest to determine the conditions under which the internal processes are relatively unimportant, so that the seasonal mean flow is more dependent on the external forcing and thus potentially more predictable.

In this chapter we compare the synoptic-scale eddies, the intraseasonal fluctuations and their interactions with the seasonal mean flow during winters with El Niño events with those during winters without an El Niño. The main objective is to study the difference in the atmospheric internal dynamic processes under these two types of winter conditions. In doing so we hope to obtain some useful information on a possible relation between the predictability of the atmosphere and the PNA weather regime.

Six major El Niño events that have occured since 1965 are composited and compared with non-El Niño years. We study how the extratropical low-frequency transients respond when the background seasonal mean flow is modified during the El Niño years. The mechanisms behind the difference of the low-frequency eddy activity between El Niño and non-El Niño winters are analyzed by considering both the kinetic energy transfer from the seasonal mean flow and the synoptic-scale transient forcing. The feedbacks to the seasonal mean flow from both the intraseasonal eddies and the synoptic-scale transients are also discussed. Our goal is to shed some light on the interactions among the three frequency bands, i.e., the seasonal mean, the low-frequency and synoptic-scale flow, and also on how the interactions are modified during El Niño winters.

3.2 The dataset

The data employed in this study are the twice-daily (0000 and 1200 GMT) analyses produced by the U. S. National Meteorological Center (NMC). The variables that are available include the geopotential height at 850, 700, 500, and 200 hPa, the temperature at 700 hPa, and the wind at 850 and 250 hPa. The data were converted from an octagonal grid to a longitude-latitude grid extending from 20°N to the North Pole with a resolution of 5 degrees in both longitude and latitude. Data for 24 winters from 1965/66 to 1988/89 are used. Winter is defined to be the 90 day period beginning at 0000 GMT 1 December. The temperature and the geopotential height data cover all the 24 winters. The 850 hPa wind data for the 1965/66 and 1969/70 winters and the 250 hPa wind data for the 1969/70 winter are not available. The 850 hPa wind in the 1965/66 and 1969/70 winters is thus replaced by the geostrophic wind calculated from the 850 hPa geopotential height. The geostrophic wind is also used at 250 hPa for the 1969/70 winter, and is calculated from the 250 hPa geopotential height interpolated from the geopotential height fields at 200 and 500 hPa. Temporal data gaps within individual winters were filled using linear interpolation in time. The longest gap is about 5 days.

In order to separate the low-frequency eddies and the synoptic-scale transients, the same Fourier filters as used in Chapter 2 are applied to the twice-daily time series of data for each winter. Thus the synoptic-scale transients have a frequency range corresponding to periods between 2 and 10 days, while the low-frequency eddies have periods from 10 to 90 days.

3.3 The interannual variations

There were six major El Niño events between 1965 and 1989. The onsets of El Niño episodes occurred close to January 1965, 1969, 1972, and 1976 (Quinn et al., 1978; Rasmusson and Carpenter, 1982), Spring 1982 (Quiroz, 1983), and September 1986 (Bergman, 1987). The peaks of El Niño events along the South American coast were observed to occur about 3-6 months after their onsets. The region of anomalously warm sea surface temperature normally reached the central Pacific by the following fall or winter (Horel and Wallace, 1981).

In demonstrating the differences between El Niño and non-El Niño years, we will focus in the following subsections on the seasonal mean flow, the low-frequency variabilities and the synoptic-scale transients. The six El Niño winters are 1965/66, 1969/70, 1972/73, 1976/77, 1982/83 and 1986/87. The non-El Niño winters are the other eighteen winter seasons. A student t-test method (see Appendix A) was used to analyze the significance of the difference between the two groups. Throughout this study the discussion is mainly focused on the North Pacific area.

a) *The seasonal mean anomaly*

Fig. 3.1a shows the 500 hPa geopotential height difference between the El Niño winters and the non-El Niño winters, as is obtained by subtracting the composite of the non-El Niño winters from that of the El Niño winters. The dominant feature is the negative height anomaly in a large area of the North Pacific. The anomaly pattern is very similar to the correlation pattern derived by Horel and Wallace (1981) on the basis of correlations between 700 hPa geopotential heights and the Southern Oscillation Index. It is also consistent with the intense Aleutian low in the mean sea level pressure during El Niño winters (Quiroz, 1983). The Pacific/North American teleconnection pattern can be recognized in the seasonal anomaly diagram. As demonstrated by Horel and Wallace (1981) the wintertime PNA index is well correlated with the seasonal mean values of the Southern Oscillation Index. The t–test (Fig. 3.1b) reveals significant geopotential height differences between the El Niño and non-El Niño winters in the North Pacific where the significance level in a large area exceeds 95%, and the distribution of the significance level tends to confirm the existence of the PNA pattern.

Corresponding to the negative height anomaly in the North Pacific during El Niño years, the north-south pressure gradient in the central-eastern Pacific is anomalously large, as are the westerlies near 30°N. This phenomenon can also be viewed as the eastward extension of the westerly jet which normally appears over and east of Japan. Fig. 3.2 shows the 250 hPa zonal wind difference between the El Niño and the non-El Niño winters. The positive anomaly near 30°N in the central-eastern Pacific is clear with a maximum in excess of 10 m/s. The above-normal westerlies seem to occur around the midlatitudes with another centre in the Atlantic. Using data up to 1982-83, Quiroz (1983) showed that the 200 hPa wind anomaly at 33°N, 165–110°W in winter has a high negative correlation (−0.9) with the Southern Oscillation index in

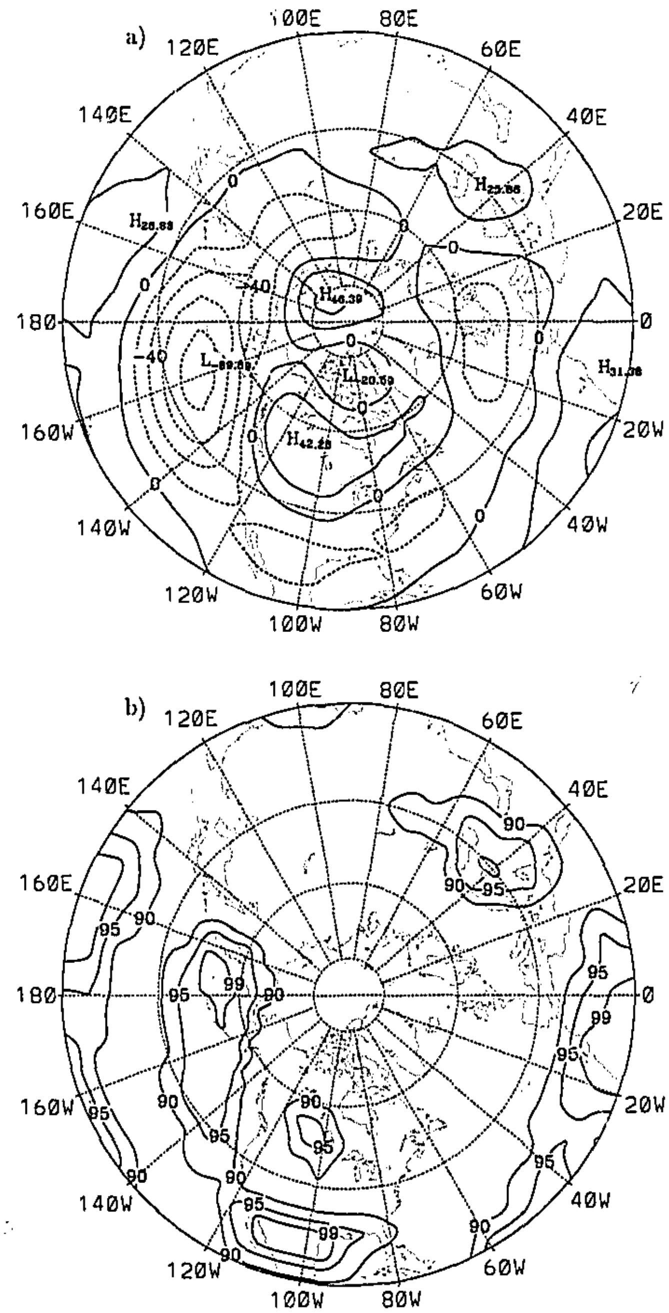

Figure 3.1: (a) Difference map obtained by subtracting the seasonal mean geopotential heights of non-El Niño winters from those of El Niño winters at 500 hPa. The contour interval is 20 m. Dashed lines indicate negative values; (b) Areas where the averaged geopotential heights of the El Niño and non-El Niño winters are different at significance levels of 90%, 95% and 99%.

that year, with a significance level of 99%.

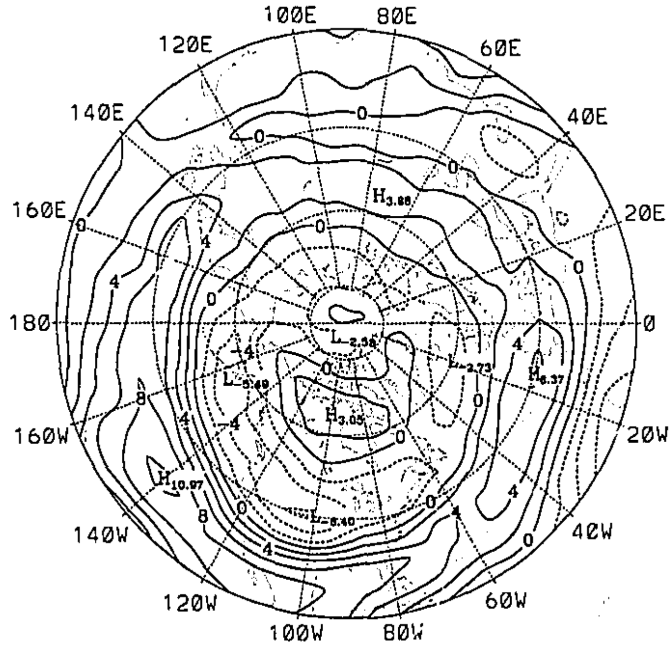

Figure 3.2: 250 hPa zonal wind difference between El Niño and non-El Niño winters. Interval is 2 m/s. Contours representing westerly anomalies are solid, and those representing easterly anomalies are dashed.

b) *The low-frequency variabilities*

In the winter season the extratropical pressure and wind disturbances with periods longer than 10 days and shorter than a season normally occur with maximum intensity over the North Pacific and North Atlantic, and over northwest Siberia, near 80°E. Among other studies, the rms calculation by Blackmon et al. (1977) and the low-frequency eddy kinetic energy study by Sheng and Derome (1991a) indicated the same observations. The centres of the low-frequency variance in the Pacific and Atlantic also correspond closely to the longitudes with the highest percentage of blocking flows, as determined by Rex (1950).

Fig. 3.3a shows the difference between the rms of the low-frequency 500 hPa geopotential height in El Niño winters and that in non-El Niño winters. The rms can be viewed as the average amplitude of the low-frequency fluctuations. It can be seen that the strength of the low-frequency variability is considerably reduced over the North Pacific in El Niño years compared with the other years. The negative centre is collocated with the maximum rms centre over the North Pacific on the climatological map. The t-test (Fig. 3.3b) indicates that in the North Pacific the significance level of the difference field exceeds 99%.

In order to see the year-to-year variation of the low-frequency eddies in the North Pacific region, the rms field has been averaged for the area 40°–70°N, 140°E–140°W for each year, and the time series is plotted in Fig. 3.3c. The years shown on the diagram refer to the beginning year of the winter season, i.e., 65 refers to the 1965/66 winter. It can be seen that the small values of the rms are well correlated with the El Niño events. The four smallest values occurred in the winters of 1969/70, 1976/77, 1982/83 and 1986/87, all of them El Niño years.

Dole and Gordon (1983) studied the characteristics of the persistent anomalies of the wintertime Northern Hemisphere, where the anomaly was the departure of the daily 500 hPa height from climatology. A persistent positive (negative) anomaly at a point was said to occur when the anomaly at that point remained equal to or greater (less) than a specified threshold value M for at least L days. As in Dole and Gordon (1983), we have calculated the number of persistent anomalies at each grid point with the criteria values of $M = +100$ m, $L = 10$ days, and $M = -100$ m, $L = 10$ days applied to the 500 hPa geopotential height. To remove possible effects of the brief transient fluctuations associated with the passing of synoptic-scale disturbances, the time series were first low-pass filtered as described in Section 2.2. Fig. 3.4a shows the difference in the total number of the positive and negative persistent anomalies between the El Niño and non-El Niño winters. The values shown have been normalized to numbers of cases per ten years. The field has also been smoothed lightly by applying a two-dimensional nine-point spatial filter as used by Dole and Gordon (1983) for display purposes. As in Fig. 3.3a, a reduction in the

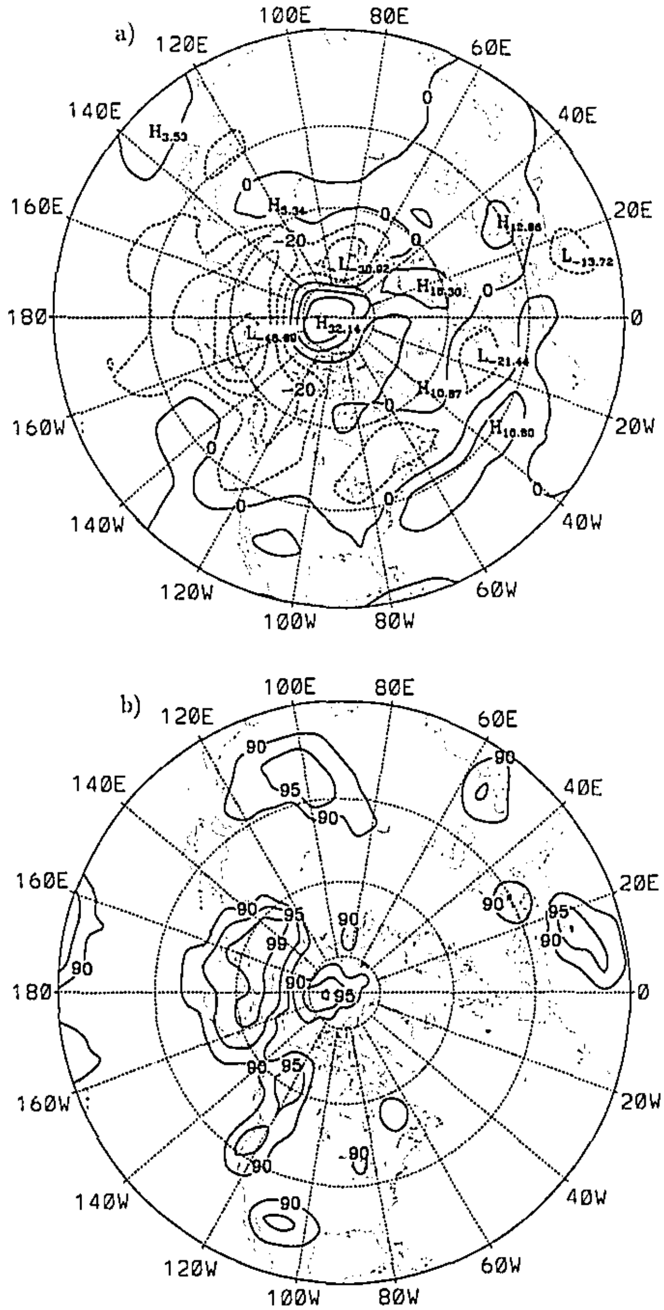

Figure 3.3: (a) Difference map obtained by subtracting low-frequency height rms at 500 hPa of non-El Niño winters from that of El Niño winters. The contour interval is 10 m. Dashed lines indicate negative values; (b) Areas where the rms of El Niño winters and that of non-El Niño winters are different at significance levels of 90%, 95% and 99%; (c) Year-to-year variation of low-frequency rms in the units of metres averaged for the area 40°–70°N, 140°E–140°W in the winter seasons. The vertical bars indicate the El Niño winters.

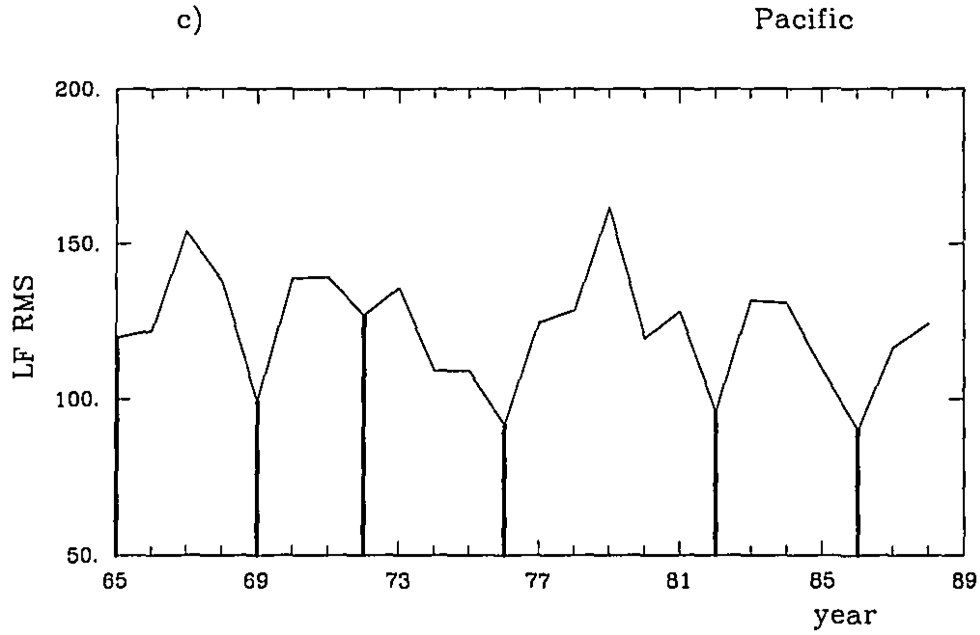

Figure 3.3: Continued.

number of persistent anomalies can be found in the North Pacific region during El Niño winters. We have also calculated the differences between the El Niño and non-El Niño years in the numbers of the positive and negative persistent anomalies separately (figures not shown). Their patterns are similar to Fig. 3.4a, so that the numbers of both positive persistent anomalies and negative persistent anomalies decrease during El Niño years. The number of blocking events over the North Pacific is thus likely to be smaller during El Niño years. The time series of the total number of positive and negative persistent anomalies averaged over 40°–70°N, 140°E–140°W is shown in Fig. 3.4c. The reduction of the number of the persistent anomalies corresponds well with the occurrences of El Niño winters.

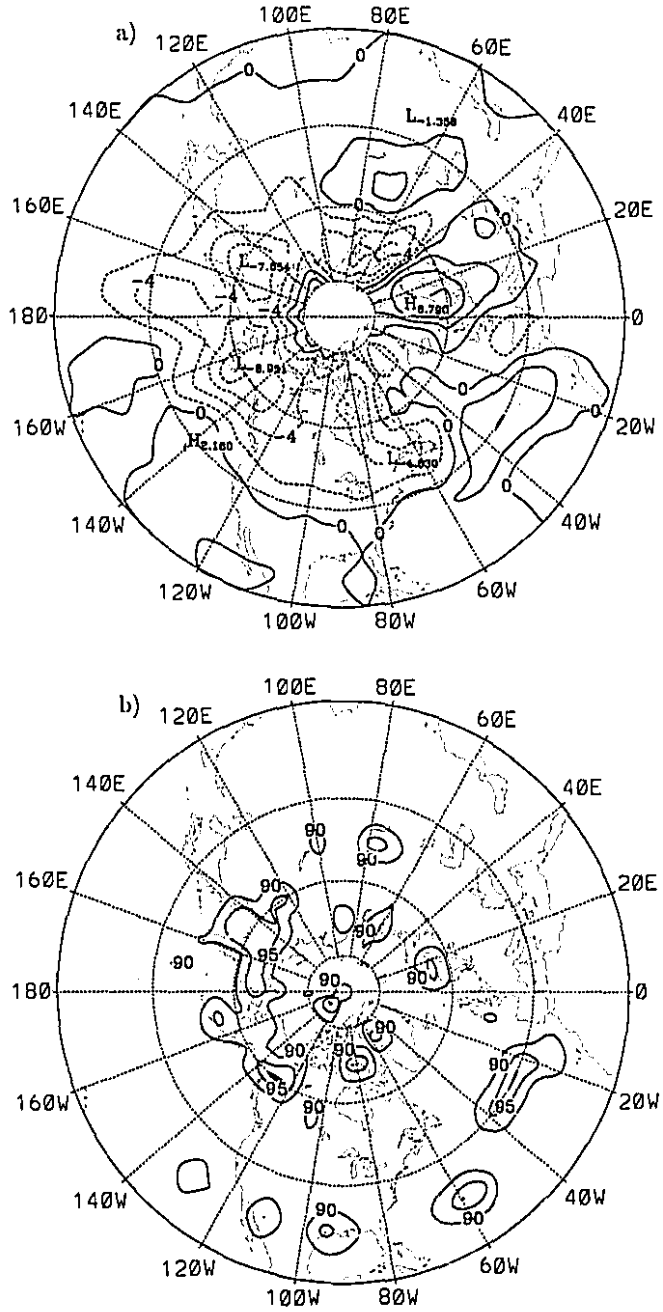

Figure 3.4: (a) Difference map obtained by subtracting the total number of positive and negative persistent anomalies in the non-El Niño winters from that of the El Niño winters. Values have been normalized as numbers per ten years. Interval is 2. Contours with negative values are dashed; (b) Areas where the difference is significant at significance levels of 90%, 95% and 99%; (c) Year-to-year variation of total number of positive and negative persistent anomalies averaged over 40°–70°N, 140°E–140°W. Values have been normalized as numbers per ten years. The vertical bars indicate the El Niño winters.

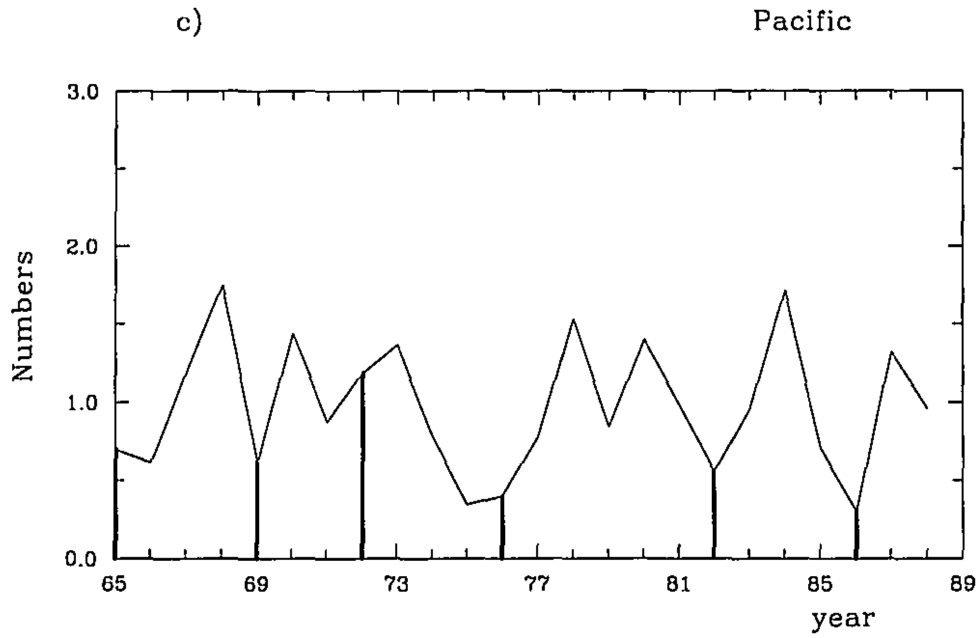

Figure 3.4: Continued.

c) *The synoptic-scale transients*

Fig. 3.5a depicts the difference in the synoptic-scale transient rms of the 500 hPa geopotential height between El Niño and non-El Niño years. A belt of positive anomaly in the rms can be found along the subtropical Pacific during El Niño years, with a major centre near 155°W and a minor centre over Japan. During these years, the axis of the Pacific storm track is thus shifted southward about 5° from its climatological position. With the enhancement of the midlatitude westerlies over the Pacific during the ENSO years, an increase of the synoptic-scale transients in this area is not surprising. The tendency for more frequent cyclone formation off the east coast of Japan during El Niño years was also discussed by Hanson and Long (1985).

From Fig. 3.5a we also note that the synoptic-scale transient activity increases in the central Atlantic, in relation with the enhanced westerlies in the subtropical

Atlantic (Fig. 3.2). It can be seen from Fig. 3.5b that the enhancement of the high-frequency eddy activity along about 35°N over the eastern Pacific and the middle Atlantic is statistically significant at the 95% in some areas.

3.4 The feedback of the high- and low-frequency transients onto the seasonal mean flow

We have seen significant differences between the El Niño and non-El Niño winters in the seasonal mean flow, the low-frequency eddies and the synoptic-scale transients. In this section, we will study the forcing of the seasonal mean flow by transient eddies, and examine the relationship between the seasonal-mean flow anomaly during El Niño winters and the feedback effect due to the modified low- and high-frequency eddies.

From the barotropic vorticity equation (1.1), the vorticity tendency of the time-mean flow can be expressed as:

$$\frac{\partial \overline{\zeta}}{\partial t} = -\nabla \cdot \overline{\mathbf{V}_h \zeta_h} - \nabla \cdot \overline{\mathbf{V}_l \zeta_l} + \overline{\mathcal{R}}, \tag{3.1}$$

where ζ is the relative vorticity, $\mathbf{V}$ is the horizontal velocity vector. The overbar represents the seasonal average and the subscripts l and h refer to the low- and high-frequency filtered data, respectively. The first and second terms on the right-hand side represent the time-mean vorticity tendency associated with the vorticity flux convergence by the synoptic-scale eddies and the low-frequency transients, respectively. $\overline{\mathcal{R}}$ includes all remaining components in the vorticity equation, such as the horizontal advection by the time mean flow, and friction.

With the geostrophic approximation the geopotential height tendency of the time-mean motion can be written as:

$$\frac{\partial \overline{z}}{\partial t} = -\frac{f}{g}\nabla^{-2}[\nabla \cdot (\overline{\zeta_h \mathbf{V}_h})] - \frac{f}{g}\nabla^{-2}[\nabla \cdot (\overline{\zeta_l \mathbf{V}_l})] + \frac{f}{g}\nabla^{-2}\overline{\mathcal{R}}, \tag{3.2}$$

where z is the geopotential height, f is the Coriolis parameter and g is the acceleration of gravity.

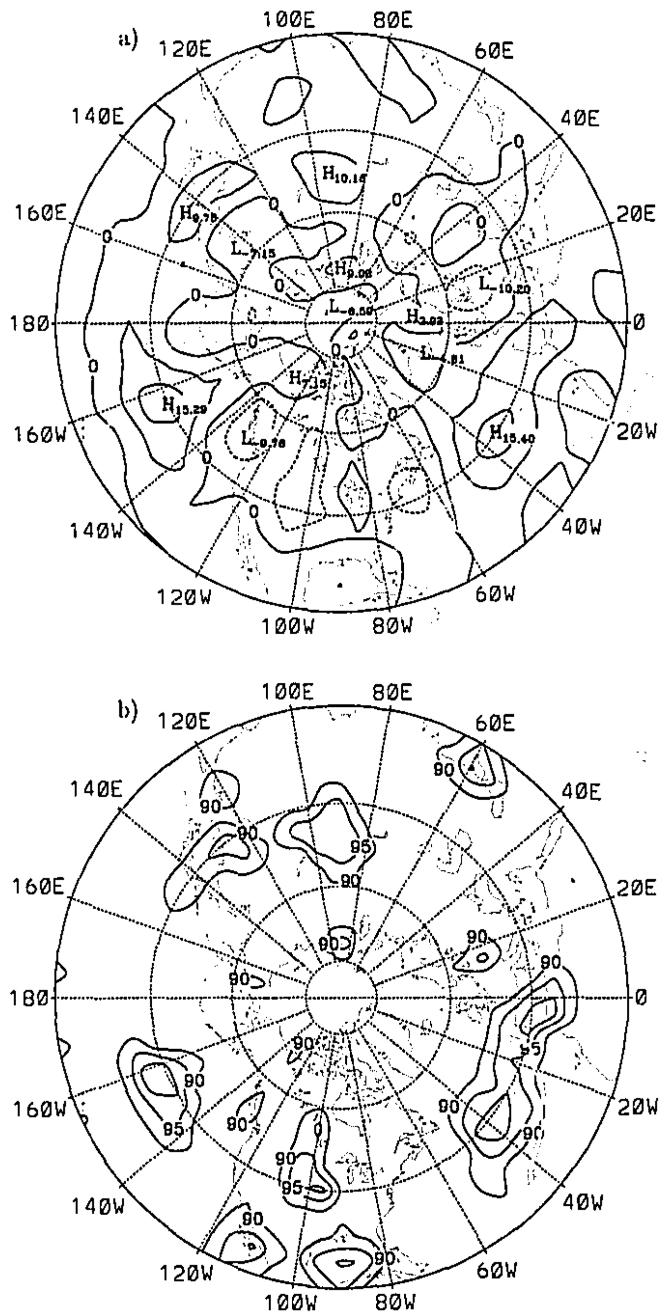

Figure 3.5: As in Figs. 3.3 (a) and (b), but for high-frequency rms of the 500 hPa geopotential height. Contour intervals are 6 m.

The transient eddies feedback onto the time-mean flow not only through their vorticity flux, but also through their heat flux. The net forcing of the time-mean flow by transient eddies should also include the geopotential height tendency caused by the heat flux convergence. Holopainen (1994) argued that in the upper troposphere the time-mean forcing of geopotential height associated with the eddy heat flux is opposite to that due to the eddy vorticity flux. As a result, the total net forcing in the upper troposphere is much weaker than that estimated from the two-dimensional (barotropic) version of the tendency method. The relative effects of the thermal and vorticity fluxes can be seen from the longitude-pressure distributions of zonal wind tendencies along 40°N, shown in Fig. 3.6 taken from Lau and Holopainen (1984). The forcing by heat fluxes changes sign from the upper to the lower troposphere, causing a westward acceleration of the time-mean flow in the upper troposphere and eastward acceleration in the lower troposphere in the storm track longitudes. The forcing by vorticity transports has the same sign at all the levels with strong eastward acceleration of the time-mean flow in the upper troposphere in the storm track longitudes.

We are here interested in the vertical integration of the net time-mean forcing by the transient eddies. From Fig. 3.6a, we can see that the thermal effect should be largely canceled out in the vertical integration of the total net forcing throughout the troposphere. Hence the vertical integral results mainly from contributions by the vorticity. Considering the wind data are available only at 250 and 850 hPa, we will use the average of the vorticity forcing at these two levels to represent the column average of the net forcing between 250 and 850 hPa. So in the following discussion in this section, the geopotential height z and the eddy forcing refer to the average of those at 250 and 850 hPa.

Let $\overline{z}_a$ be the anomaly of the seasonal mean height during El Niño winters with respect to that of non-El Niño winters, i.e.

$$\overline{z}_a = \overline{z}_e - \overline{z}_n,$$

where $\overline{z}_e$ and $\overline{z}_n$ represent the composite seasonal mean height of El Niño and non-El

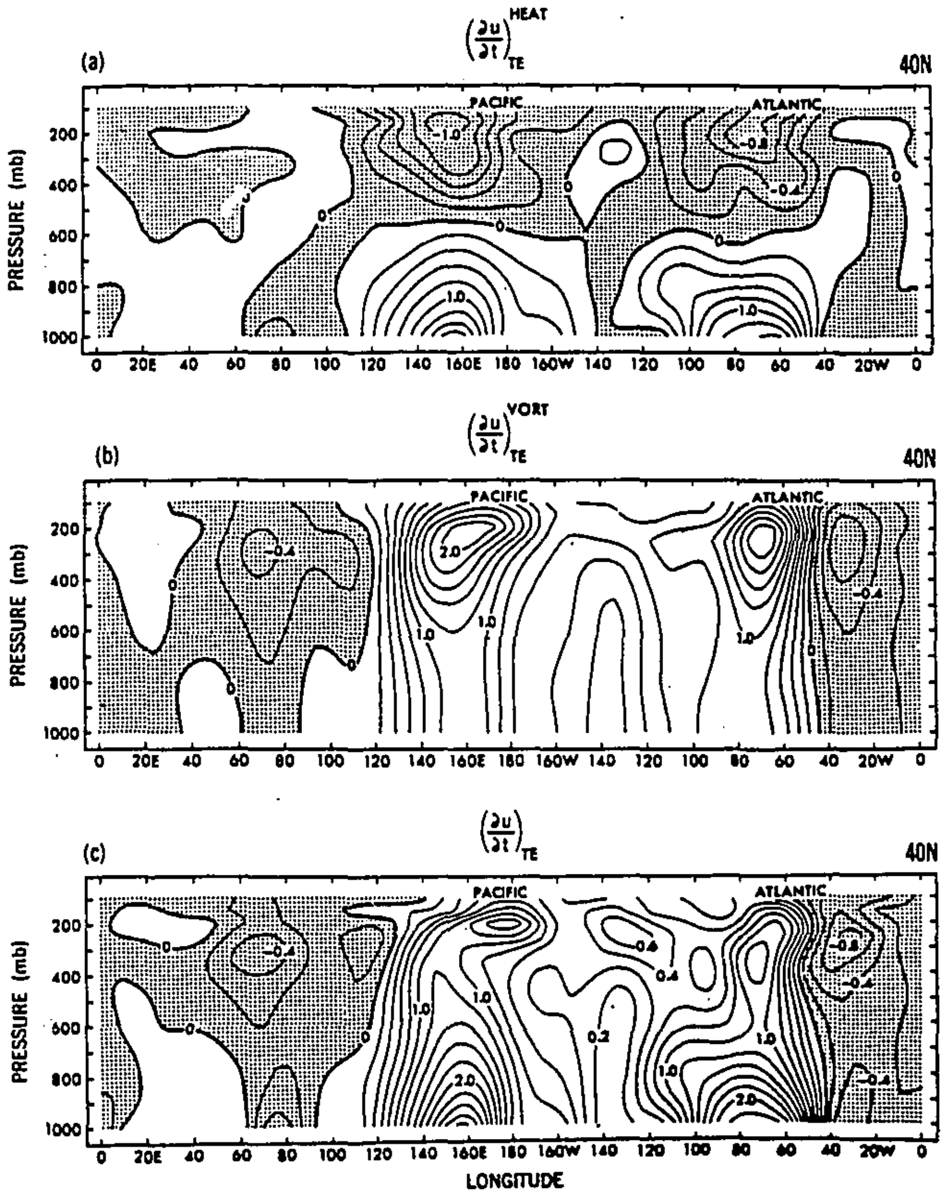

Figure 3.6: Longitude-pressure distributions at 40°N of the zonal geostrophic wind tendencies associated with (a) the high-frequency eddy heat fluxes; (b) the high-frequency eddy vorticity fluxes and (c) sum of the high-frequency eddy heat and vorticity fluxes. Contour interval is 0.2 m s^{-1} day^{-1}. Shading indicated negative values. [From Lau and Holopainen, 1984]

Niño winters, respectively. Then from (3.2) we have

$$\frac{\partial \overline{z}_a}{\partial t} = \mathcal{F}_a + \mathcal{G}_a + \mathcal{H}_a, \tag{3.3}$$

where

$$\mathcal{F}_a = \{-\frac{f}{g}\nabla^{-2}[\nabla \cdot (\overline{\zeta_h \mathbf{V}_h})]\}_e - \{-\frac{f}{g}\nabla^{-2}[\nabla \cdot (\overline{\zeta_h \mathbf{V}_h})]\}_n;$$

$$\mathcal{G}_a = \{-\frac{f}{g}\nabla^{-2}[\nabla \cdot (\overline{\zeta_l \mathbf{V}_l})]\}_e - \{-\frac{f}{g}\nabla^{-2}[\nabla \cdot (\overline{\zeta_l \mathbf{V}_l})]\}_n;$$

$$\mathcal{H}_a = \{\frac{f}{g}\nabla^{-2}\overline{\mathcal{R}}\}_e - \{\frac{f}{g}\nabla^{-2}\overline{\mathcal{R}}\}_n.$$

Terms $\mathcal{F}_a$ and $\mathcal{G}_a$ represent the anomalous high- and low-frequency forcing, respectively, that cause the anomalous height tendency. $\mathcal{H}_a$ is the anomalous height tendency associated with the different contributions of $\overline{\mathcal{R}}$ between El Niño winters and non-El Niño winters.

Fig. 3.7a is the difference of the geopotential height tendency caused by the high-frequency eddies between El Niño and non-El Niño winters ($\mathcal{F}_a$). We see that the anomalous negative height forcing pattern over the North Pacific coincides with the seasonal-mean negative height anomaly presented in Fig. 3.1a. During El Niño years the eastward extension of the synoptic-scale baroclinic waves produces a barotropic forcing that tends to deepen the Aleutian low, and accelerates the seasonal mean zonal flow to the south. By studying the synoptic-scale transient forcing of the monthly PNA pattern, Klasa et al. (1992) arrived at similar results, namely, that the eddy barotropic forcing is in phase with the height anomaly. Kok and Opsteegh (1985) and Ting and Hoerling (1993) showed that the extratropical wave train anomalies during the 1982/83 and 1986/87 El Niño winters were maintained by the transient eddy forcing.

The feedback of the intraseasonal low-frequency variabilities onto the seasonal mean flow is different from that of the synoptic-scale eddies. Fig. 3.7b shows the difference of the geopotential height tendency caused by the low-frequency eddies

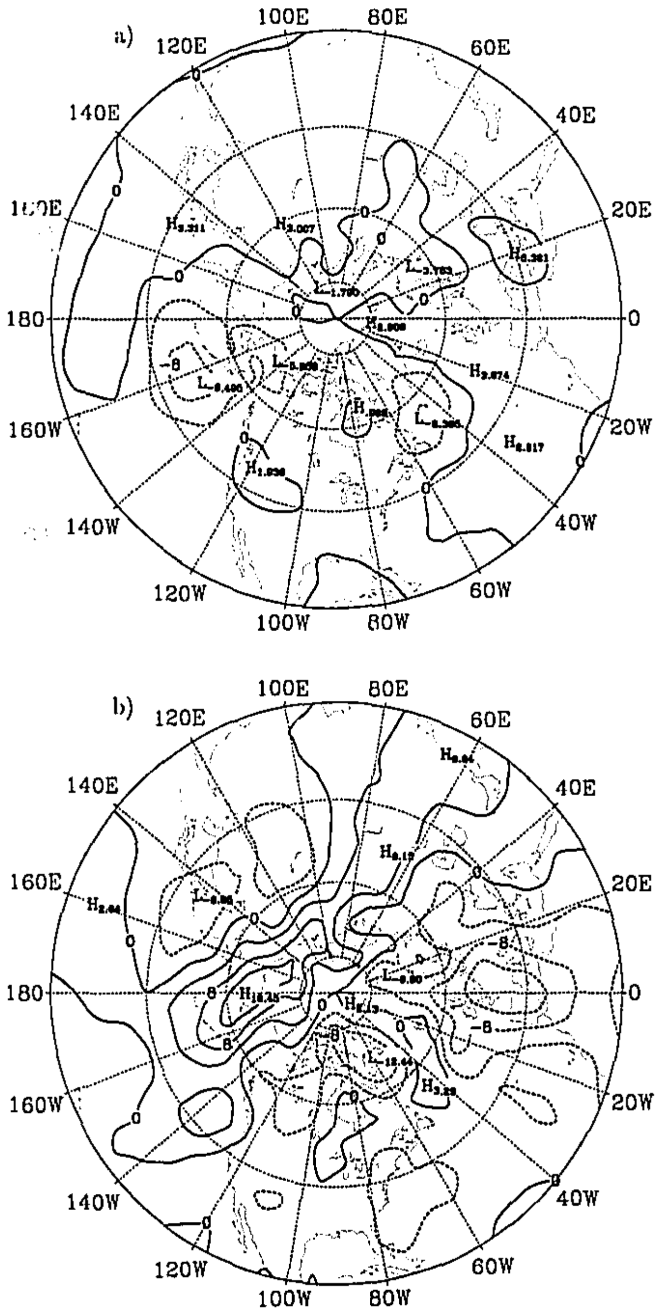

Figure 3.7: Difference map as obtained by subtracting the seasonal mean geopotential height tendency caused by (a) high-frequency eddies; (b) low-frequency eddies in non-El Niño winters from that in El Niño winters. The contour intervals are 4×10^{-5} m/s.

between the El Niño and the non-El Niño years ($\mathcal{G}_a$). An area of positive values covers the entire North Pacific. This pattern tends to be out of phase with the PNA anomalies, suggesting that the low-frequency transients act to dissipate the large-scale seasonal-mean wave pattern. Lau and Holopainen (1984) found that the geopotential tendency by the low-frequency eddies is out of phase with the stationary waves in the upper troposphere. A negative geopotential height tendency is expected in the location of the ridge in the time-averaged upper tropospheric height field over the northeast Pacific (e.g., Fig. 6b in Lau, 1979). As can be expected, in the El Niño years the values of the negative geopotential tendency tend to be weaker than those in the non-El Niño years due to the reduced low-frequency eddy activity. Thus positive values appear over the northeast Pacific on the difference map of the low-frequency forcing (Fig. 3.7b).

3.5 The barotropic energy exchange between the low-frequency and the seasonal mean flows

We have seen Section 3.3 that there is a significant reduction of the low-frequency eddy activity in the North Pacific during El Niño winters. To understand why the extratropical low-frequency variability is weaker during El Niño years, we turn to a study of the kinetic energy sources of the low-frequency transients. One energy source is the barotropic energy exchange with the background mean flow.

Following Simmons et al. (1983), the barotropic conversion of kinetic energy from the seasonal mean to the low-frequency eddies, to a good approximation, can be written as:

$$C = \mathbf{E} \cdot \nabla \overline{u} \tag{3.4}$$

where $\mathbf{E} = -(\overline{u_l}^2 - \overline{v_l}^2, \overline{u_l v_l})$ is the extended Eliassen-Palm flux which has been discussed in detail by Hoskins et al. (1983). u and v are the zonal and meridional velocity components, respectively. The overbar represents the seasonal average and the subscript l refers to the low-pass filtered data. The calculation of C is done for every winter at 250 hPa using the wind data. The equivalent barotropic structure of the extratropical low-frequency flow and the large barotropic energy conversion rate in the upper troposphere should allow the calculations at that level to capture the essential features of the kinetic energy conversion (e.g., Simmons et.al., 1983).

To see the difference in the barotropic conversion of kinetic energy between El Niño and non-El Niño winters, a comparison is made between the composites of C for these two conditions. Fig. 3.8a shows the distributions of C for the non-El Niño winters. Positive values are found over most of the extratropical regions, indicating that the low-frequency fluctuations are extracting kinetic energy from the seasonal mean flow. The maximum energy conversion occurs in the jet-exit region of the middle Pacific. Another weaker centre of energy conversion is located over the Atlantic jet-exit region. Because the 18 non-El Niño winters include the extreme negative PNA cases and more normal winters, the feature described in Fig. 3.8a should not be very different from the winter-time climatology. Actually, Fig. 3.8a is very similar to Fig. 4c of Wallace and Lau (1985) which gives the climatological kinetic energy conversion between the low-frequency transients and the mean flow averaged over eight winters.

In the case of the El Niño years, the region of barotropic energy conversion is shifted to the eastern Pacific and both its area and the maximum value of the conversion are reduced, as may be seen in Fig. 3.8b. The eastward extension of the Pacific westerly jet in the El Niño years causes a reduction of the east-west gradient of the seasonal mean zonal flow ($\partial\overline{u}/\partial x$) and the associated kinetic energy conversion in the western and central Pacific. By subtracting Fig. 3.8a from Fig. 3.8b (Fig. 3.8c), it is clearer that the low-frequency eddies extract less kinetic energy from the background mean flow during El Niño years, especially in the western and central Pacific.

Palmer (1988) examined the barotropic instability problem for the positive and negative PNA phases, and found that during the negative PNA phase the atmosphere is more unstable to the low-frequency disturbances than during the positive PNA phase. Our result is consistent with that of Palmer in that the kinetic energy transfer

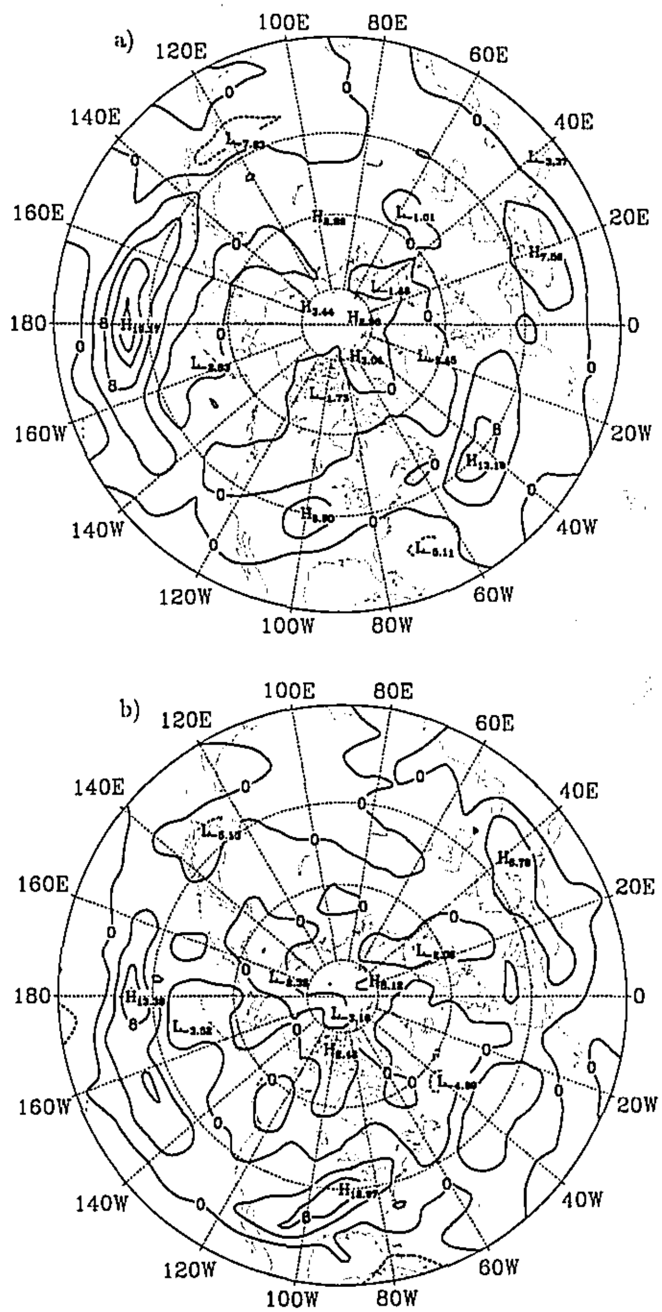

Figure 3.8: (a) C for non-El Niño winters; (b) C for El Niño winters; (c) The difference by subtracting (a) from (b). The contour intervals are 4×10^{-4}W kg^{-1} for (a) and (b) and 2×10^{-4}W kg^{-1} for (c).

c)

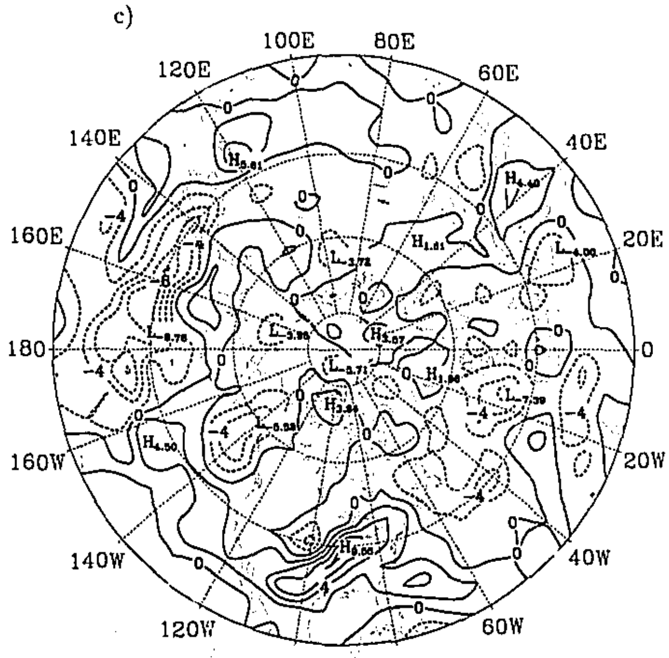

Figure 3.8: Continued.

from the mean flow to the low-frequency transients is weaker during El Niño winters, which are associated with the positive PNA phase.

We have also calculated the kinetic energy exchange between the synoptic-scale transients and the mean flow for both El Niño and non-El Niño years, by replacing u_l and v_l in (3.4) with u_h and v_h, which include periods between two and 10 days (figures not shown). In contrast to the low-frequency eddies, the synoptic-scale transients supply kinetic energy to the mean flow in the jet-exit regions. During El Niño winters, as during the positive PNA phase studied by Klasa et al. (1992), more kinetic energy is supplied to the mean flow over the eastern Pacific.

3.6 The interaction between the low- and high-frequency eddies

In addition to extracting kinetic energy from the time-mean flow, the low-frequency fluctuations can also draw kinetic energy from the high-frequency eddies. Here we analyze the interactions between the low-frequency flows and the high-frequency (synoptic-scale) transients, and examine how the interactions are modified during El Niño winters. The analysis will provide a better understanding of why the low-frequency eddy activity is weaker than normal during El Niño winters over the North Pacific. As stated earlier, the interaction between the low-frequency flow and the synoptic-scale eddies is not likely to be predictable, so it is of interest to identify flow regimes for which the interaction is relatively weak (or strong), and hence the low-frequency flow potentially more (or less) predictable.

Instead of calculating the kinetic energy exchange between the high- and low-frequency eddies, which requires an area integration and hence cannot provide unambiguous information on the geographical distribution of the conversion, here we compute the temporal covariance between the low-frequency geopotential height tendency and the barotropic high-frequency eddy forcing. The barotropic high-frequency eddy forcing is defined as the convergence of the vorticity flux by the synoptic-scale transients. As can be seen in the following derivation, this covariance gives a measure of the change of the low-frequency geopotential height variance caused by the interaction between the high- and low-frequency eddies.

The geopotential height tendency of the low-frequency variation may be written as:

$$\begin{aligned}\frac{\partial z_l}{\partial t} &= -\frac{f}{g}\nabla^{-2}\nabla\cdot(\mathbf{V}_h\zeta_h)_l - \frac{f}{g}\nabla^{-2}\nabla\cdot(\mathbf{V}_l\zeta_l)_l \\ &\quad -\frac{f}{g}\nabla^{-2}\nabla\cdot(\mathbf{V}_h\zeta_l + \mathbf{V}_l\zeta_h)_l + \frac{f}{g}\nabla^{-2}\mathcal{R}_l. \end{aligned} \tag{3.5}$$

This equation is similar to (3.2) except that the tendency is projected onto the low-frequencies here while in (3.2) the time-averaged tendency was used. The first and the second terms of (3.5) represent the vorticity flux convergence by the synoptic-scale eddies and by the low-frequency transients, respectively. The third term is the vorticity flux convergence by the interactions between the high- and low-frequency eddies.

Similar consideration as in Section 3.4 is applied here to estimate the column averaged low-frequency net geopotential height tendency and to eliminate the effect of the thermal forcing. In the following discussion z_l and the vorticity forcing refer to the average of values at 250 and 850 hPa.

By multiplying (3.5) with z_l, the two-level averaged low-frequency component of geopotential height, and then averaging over time, we obtain the covariance of the low-frequency geopotential height and the height tendency, or the tendency of the low-frequency height variance:

$$\begin{aligned} \frac{\partial}{\partial t}(\frac{1}{2}\overline{z_l{}^2}) &= -\frac{f}{g}\overline{z_l\nabla^{-2}\nabla\cdot(\mathbf{V}_h\zeta_h)_l} - \frac{f}{g}\overline{z_l\nabla^{-2}\nabla\cdot(\mathbf{V}_l\zeta_l)_l} \\ &\quad -\frac{f}{g}\overline{z_l\nabla^{-2}\nabla\cdot(\mathbf{V}_h\zeta_l+\mathbf{V}_l\zeta_h)_l} + \frac{f}{g}\overline{z_l\nabla^{-2}\mathcal{R}_l}. \end{aligned} \quad (3.6)$$

All the interactions between the high- and low-frequency eddies are included in the first and the third terms on the right-hand side of (3.6). The third term however is found to be much smaller than the first so that the latter can be taken to represent the tendency of geopotential height variance due to the barotropic interaction between the low- and high-frequency transients.

Fig. 3.9a shows the geographic distribution of the first term on the right-hand side of (3.6) for the non-El Niño winters. It is seen that the covariance between z_l and the high-frequency transient forcing is positive throughout most of the extratropics, with two major centres occuring over the North Pacific and the Atlantic, indicating that the vorticity flux convergence by the high-frequency eddies is forcing the low-frequency geopotential height variations. The distribution of the covariance is consistent with the temporal correlation coefficients between the 500 hPa monthly mean height and the height tendency by synoptic-scale eddy forcing as shown in Fig. 13 of Lau (1988), and with the simultaneous correlation coefficients between the 300 hPa low-frequency height z_l and the high-frequency eddy forcing as shown in Fig. 2c of Sheng and Derome (1993).

The covariance between the low-frequency geopotential height and the barotropic high-frequency eddy forcing for the El Niño winters is shown in Fig. 3.9b. In the North Pacific region the major positive maximum covariance centre is limited to the Pacific east of 160°W, with a much smaller area than in Fig. 3.9a. The contribution of the high-frequency transients to the low-frequency eddies over the northwest Pacific is seen to be reduced when compared to the non-El Niño years. The comparison between Fig. 3.9a and b also reveals that the positive centre over the North Atlantic is shifted to the east toward Scandinavia and northern Europe during El Niño winters.

The difference pattern obtained by subtracting Fig. 3.9a from Fig. 3.9b is mapped in Fig. 3.9c. Negative values dominate over the North Pacific, but a positive area is found off the west coast of North America, where the contribution of the high-frequency eddy forcing tends to be enhanced. This pattern indicates that the location of low-frequency forcing by the high-frequency transients is shifted eastward in the El Niño winters, resulting in reduced eddy forcing over the western and central Pacific, and enhanced eddy forcing over the eastern Pacific. Comparing Fig. 3.9c with Fig. 3.3a, we see that the patterns are quite similar. The reduction of the high-frequency eddy forcing thus seems to play an important role in the reduction of the low-frequency activity in the El Niño years.

3.7 The thermal aspects of the transients

In the above discussions, the barotropic characteristics of the transients have been examined. Now we take into account the thermal aspects of the low- and high-frequency transients. We examine how the temperature fields of the seasonal mean flow, the low-frequency and synoptic-scale eddies differ between El Niño and non-El Niño winters. As done for the barotropic effects, we also examine the interactions between the different time scales of the temperature fields. We thereby hope to obtain

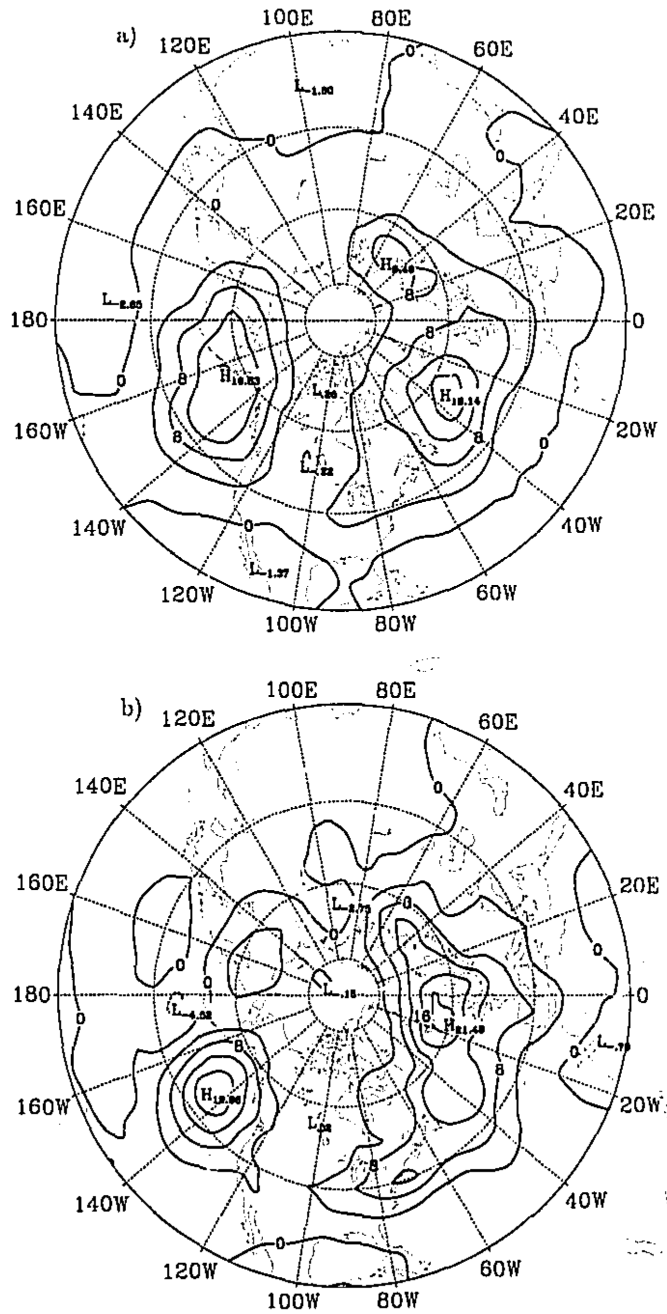

Figure 3.9: Covariance between the low-frequency geopotential height and the synoptic-scale eddy forcing at 250 hPa for (a) non-El Niño winters; (b) El Niño winters; (c) Difference by subtracting (a) from (b). The contour intervals are 4×10^{-3} m^2/s. (d) Significance levels greater than 80% at the interval of 5%, and at 99%.

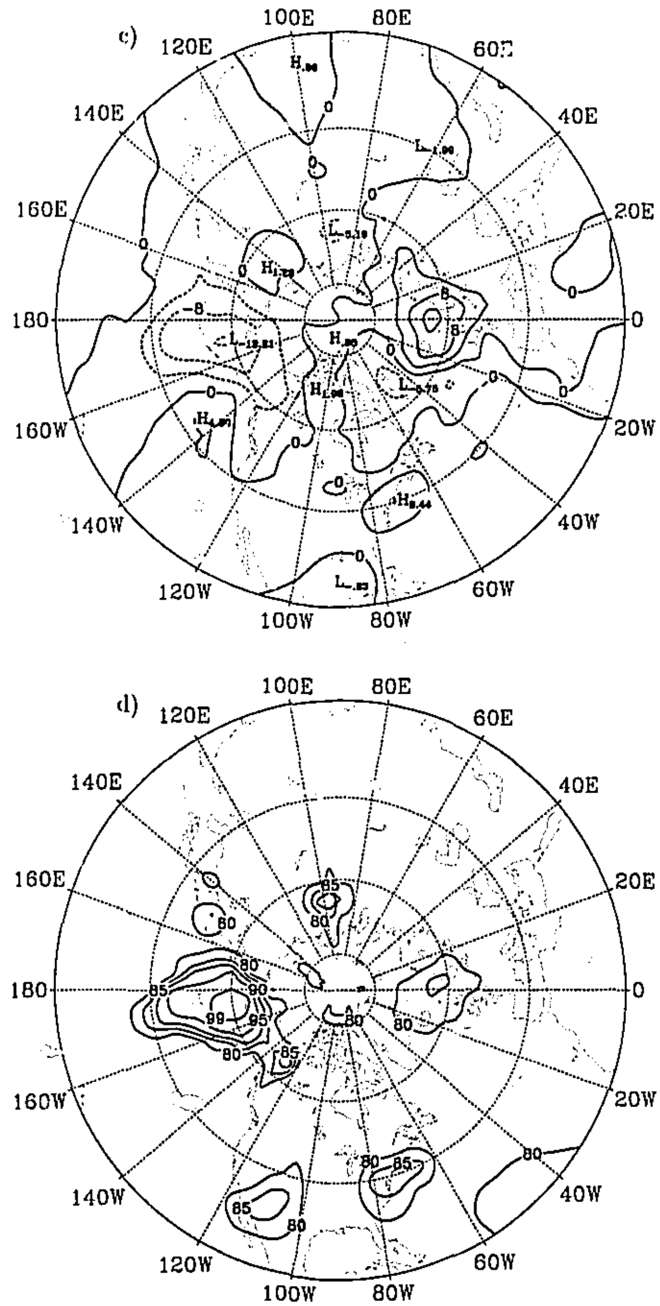

Figure 3.9: Continued.

a more complete picture of the transients and their interactions in an El Niño year.

a) *Composite seasonal temperature and variability anomalies*

The 700 hPa seasonal mean temperature difference between the El Niño and the non-El Niño winters (Fig. 3.10a) shows that there is a cold anomaly over the North Pacific during El Niño winters, which is in phase with the 500 hPa geopotential height anomaly of Fig. 3.1a. The t–test (Fig. 3.10b) reveals significant temperature differences over the North Pacific where the significance level in a large area exceeds 95%. A comparison of Fig. 3.1a and 3.10a shows that the anomalies are equivalent barotropic.

As revealed by the standard deviation calculation of the 700 hPa low-frequency temperature (Fig. 2.3), the winter extratropical temperature disturbances with periods longer than 10 days and shorter than a season are likely to happen over the North American and Siberian continents. The weakness of the low-frequency temperature variance over the oceans is due to the tendency of the oceans to warm (cool) the cold (warm) air, thus smoothing out the atmospheric temperature contrasts and reducing the possibility of persistent temperature anomalies. Fig. 3.11a shows the difference in the low-frequency rms temperature between the El Niño and the non-El Niño winters at 700 hPa. Although the temporal standard deviation of the low-frequency temperature has maxima over the land masses, the maximum change of the standard deviation between non-El Niño and El Niño winters occurs over the North Pacific, with reduced low-frequency temperature variability during the El Niño winters. This anomaly pattern looks similar to that of the reduced low-frequency geopotential height variability over the North Pacific (Fig. 3.3a), implying that the interannual variation of the low-frequency temperature field is well connected with that of the low-frequency geopotential height field.

Just as its geopotential height counterpart, the area of high standard deviation of the synoptic-scale temperature during El Niño winters is shifted south-eastward from its climatological position (Fig. 3.12a).

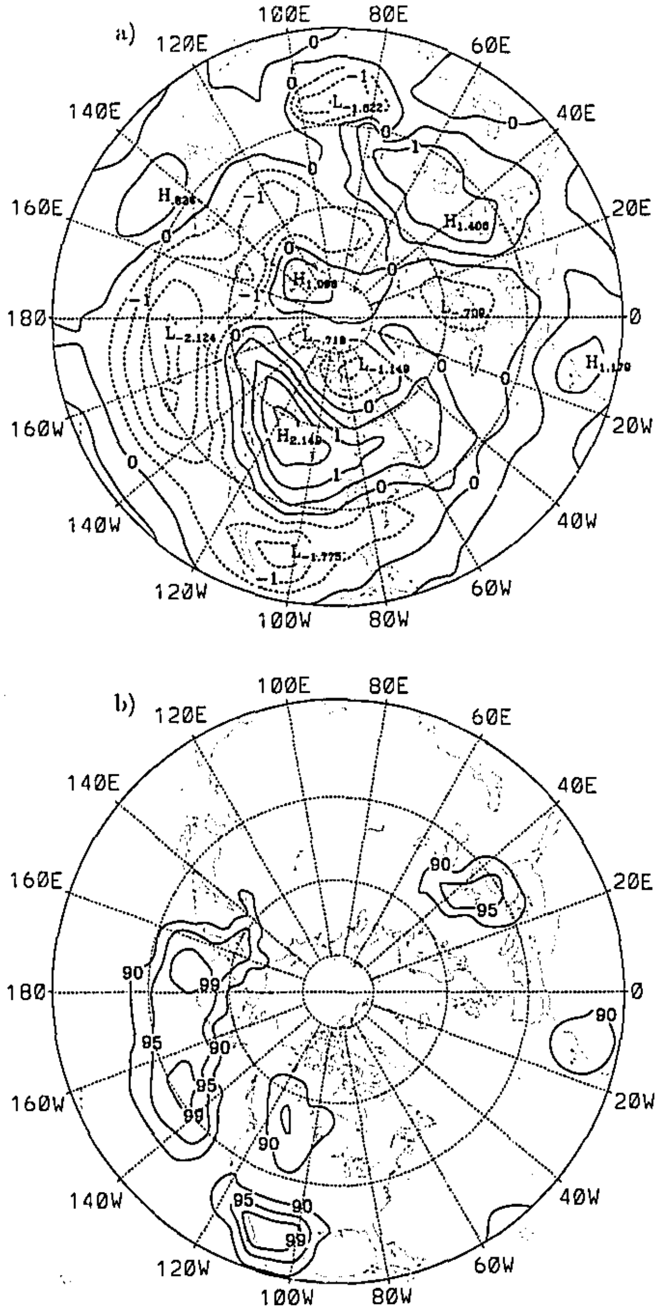

Figure 3.10: (a) Difference map obtained by subtracting the seasonal mean temperature of non-El Niño winters from that of El Niño winters at 700 hPa. The contour interval is 0.5 K. Dashed lines indicate negative values. (b) Areas where the averaged temperature of El Niño and non-El Niño winters are different at significance levels of 90%, 95% and 99%.

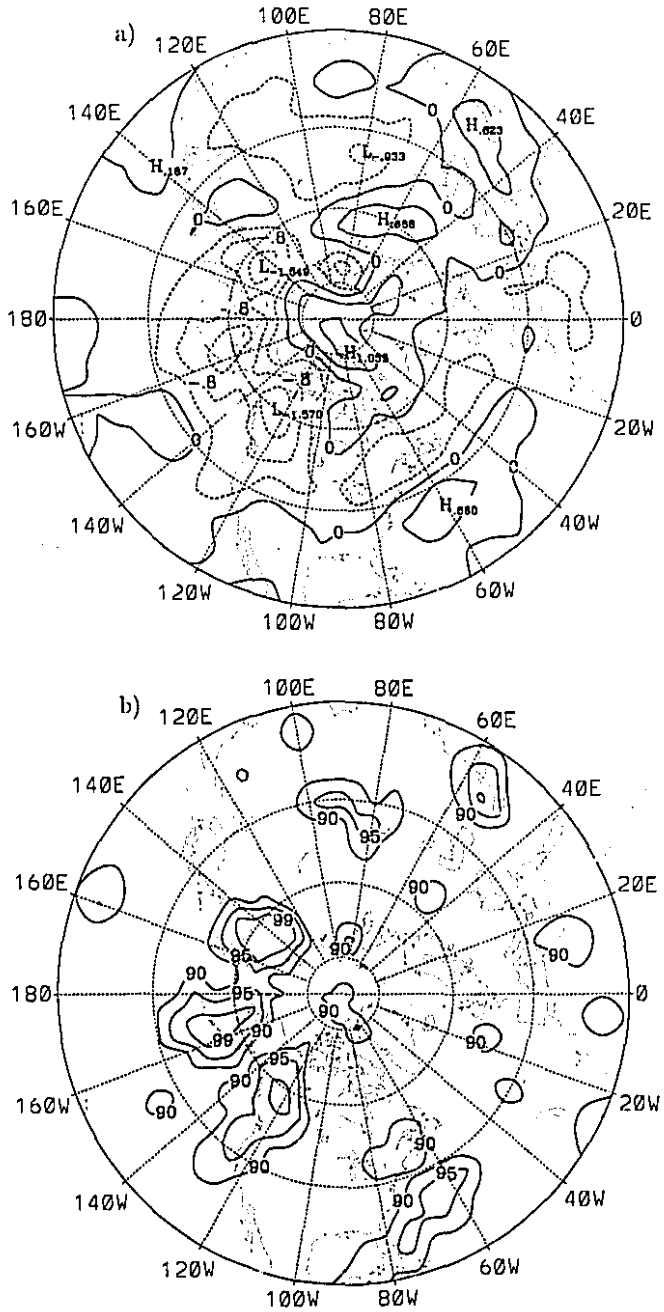

Figure 3.11: (a) Difference map obtained by subtracting low-frequency temperature rms at 700 hPa of non-El Niño winters from that of El Niño winters. The contour interval is 0.4 K. Dashed lines indicate negative values; (b) Areas where the rms of El Niño winters and that of non-El Niño winters are different at significance levels of 90%, 95% and 99%.

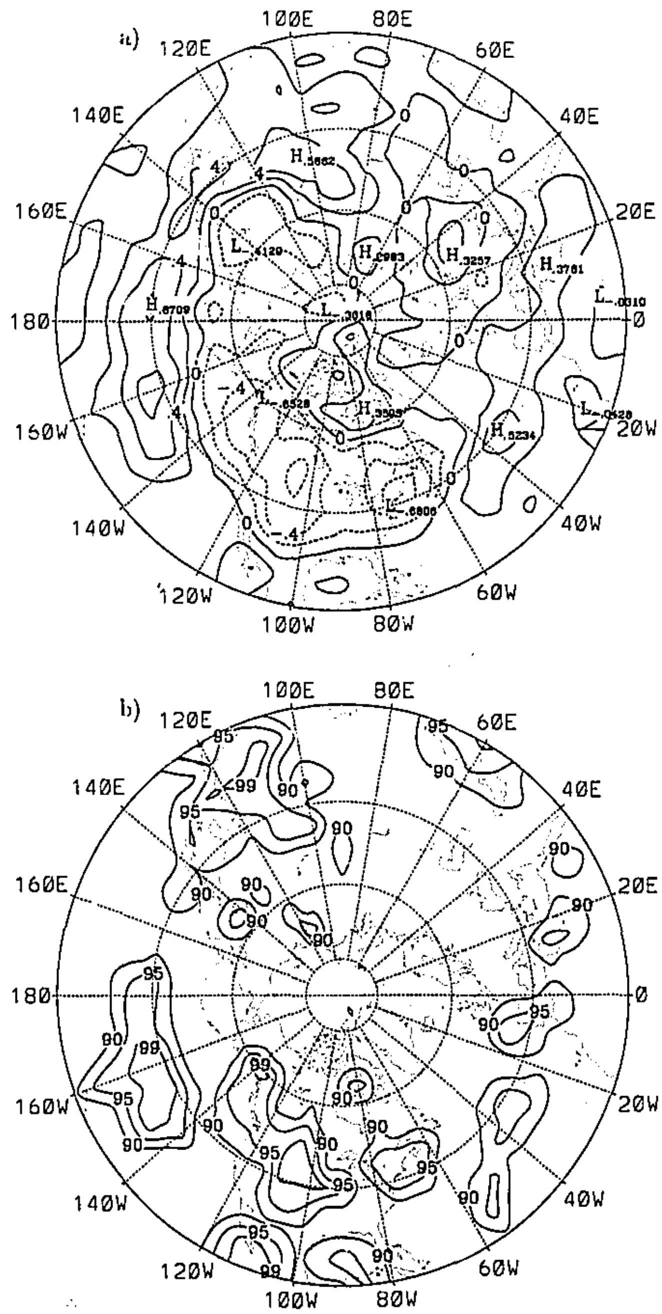

Figure 3.12: As in Fig. 3.10, but for high-frequency temperature rms. The contour interval is 0.2 K in (a).

b) *The thermal variance budget analysis for the low-frequency transients*

In order to understand why the extratropical low-frequency temperature variability is weaker over the North Pacific in El Niño years than in non-El Niño years, we examine the budget equation for the low-frequency thermal variance at 700 hPa by means of equation (2.9).

Figs. 3.13a and b show the geographical distribution of term $\overline{T_l \mathcal{C}_l}$ for the El Niño and the non-El Niño winters, respectively. The contribution by the synoptic-scale eddy horizontal heat flux $-\overline{T_l \nabla \cdot (\mathbf{V}_h T_h)_l}$ dominates in this term. It can be seen as the tendency of the low-frequency thermal variance due to the interaction between the low and the high frequency eddies. In agreement with Chapter 2, negative values are found over the middle and high latitudes, implying that the high-frequency eddies act to damp the low-frequency temperature variance. The largest negative values are found along the mean storm track regions. The difference between the El Niño and the non-El Niño winters (Fig. 3.13c) indicates that over the North Pacific the damping effect of the high-frequency eddies is weaker during El Niño winters. This may be explained by the weaker synoptic-scale eddy activity over the North Pacific due to the southward shift of the storm track during El Niño winters.

The distributions of the thermal variance tendency associated with the term $\overline{T_l \mathcal{A}_l}$ for the El Niño and the non-El Niño winters are shown in Figs. 3.14a and b, respectively. Positive values are observed over most of the Northern Hemisphere with maxima over the eastern continental areas and western oceans. This feature implies that as far as horizontal motions are concerned, the interaction of the low-frequency eddies with the time-mean flow is a source of low-frequency temperature variance. From the energetics point of view, this term can be related to the transfer of low-frequency available potential energy from the mean flow. During El Niño winters this source of the low-frequency temperature variance over the North Pacific is considerably reduced (Fig. 3.14c), which may explain why the low-frequency temperature variability in El Niño winters is weaker in this region (Fig. 3.11a).

Here we did not compute $\overline{T_l \mathcal{B}_l}$ because the vertical velocity data were not available.

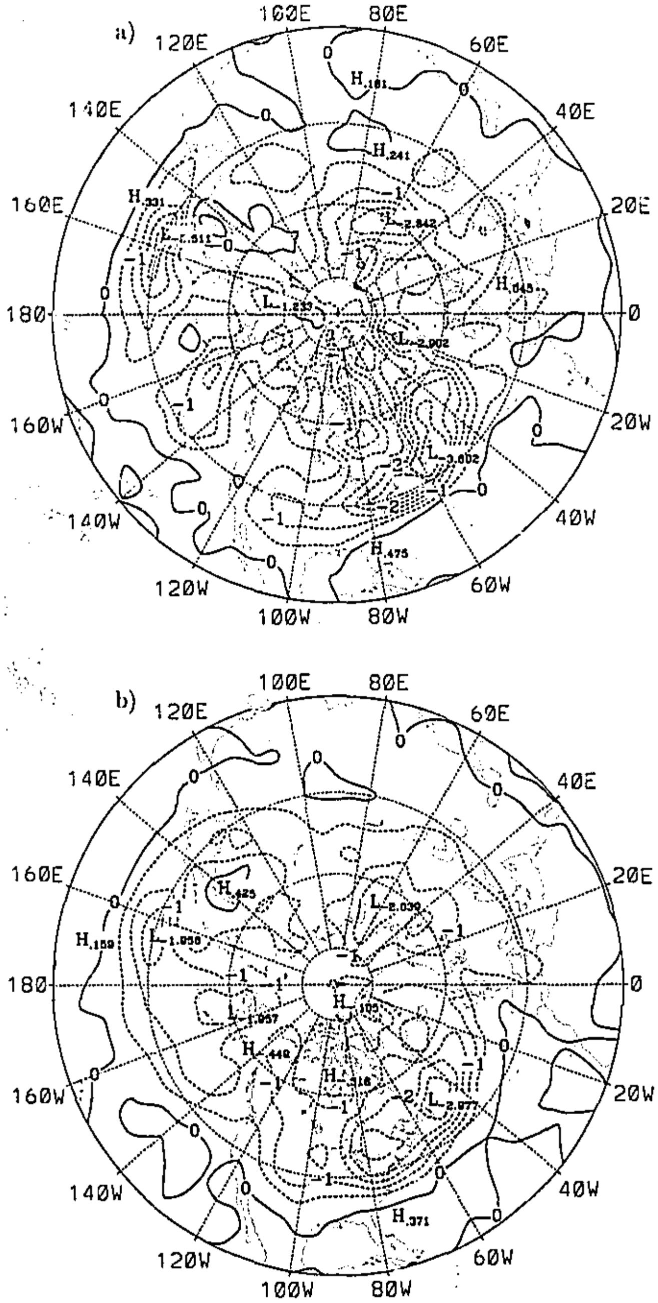

Figure 3.13: Distribution of $\overline{T_l C_l}$ for (a) El Niño winters and (b) non-El Niño winters. (c) Difference by subtracting (b) from (a). The contour intervals are 0.5 K^2/day. (d) Significance levels greater than 80% at the interval of 5%.

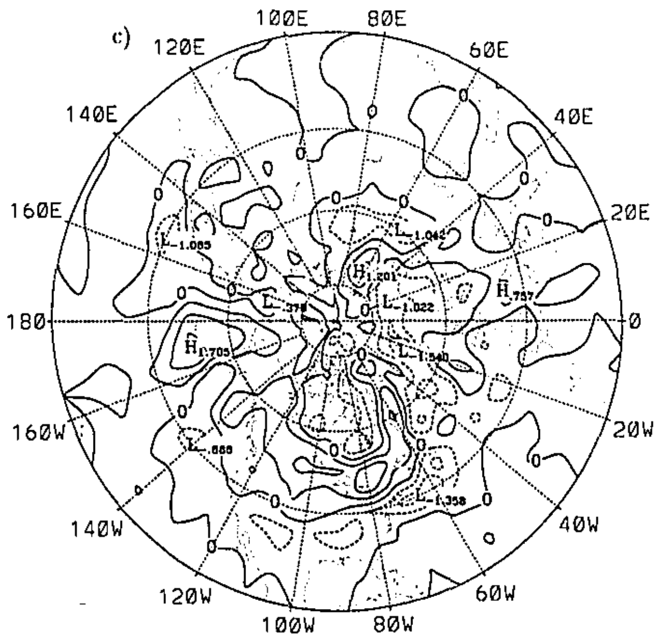

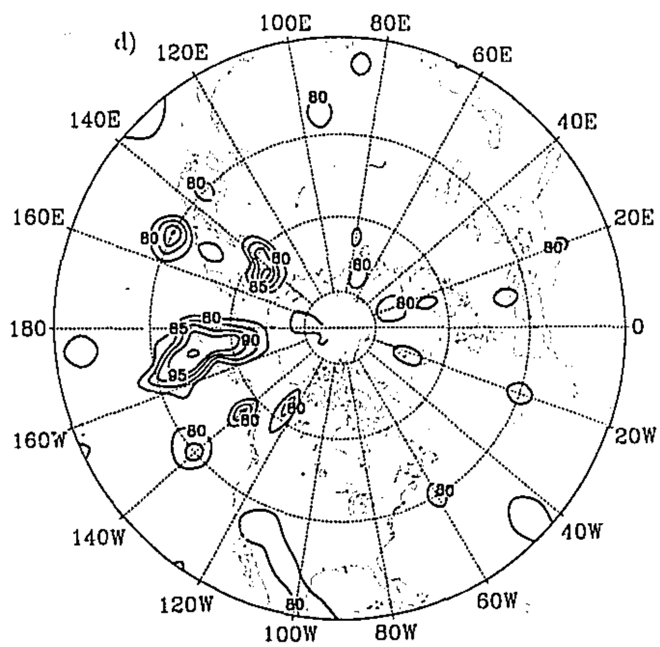

Figure 3.13: Continued.

a)

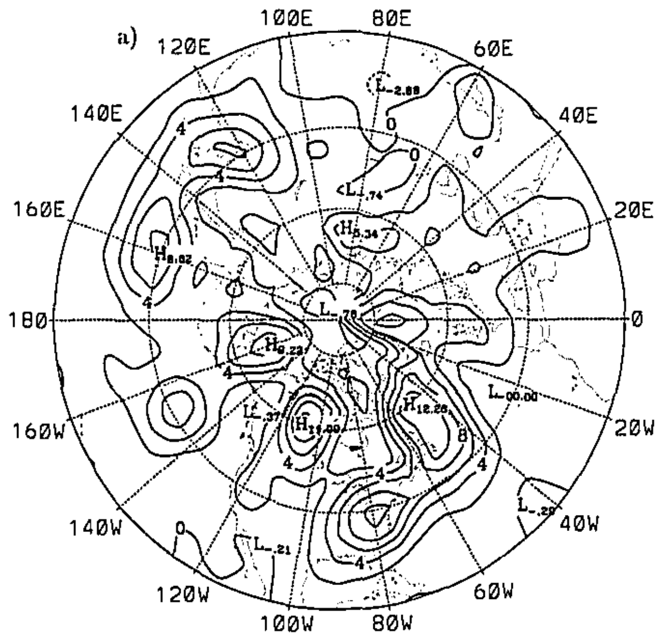

b)

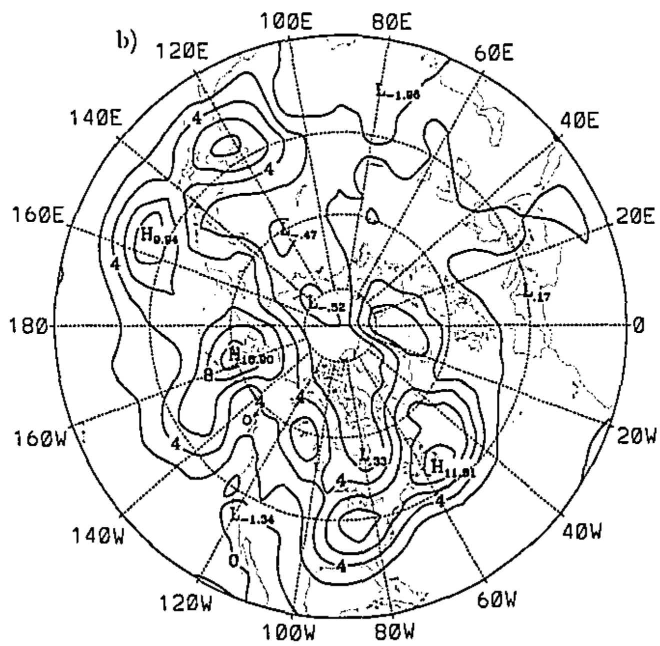

Figure 3.14: Distribution of $\overline{T_l \mathcal{A}_l}$ for (a) El Niño winters and (b) non-El Niño winters. (c) Difference by subtracting (b) from (a). (d) Significance levels greater than 80% at the interval of 5%. The contour intervals are 2 K^2/day for (a) and (b), and 1 K^2/day for (c).

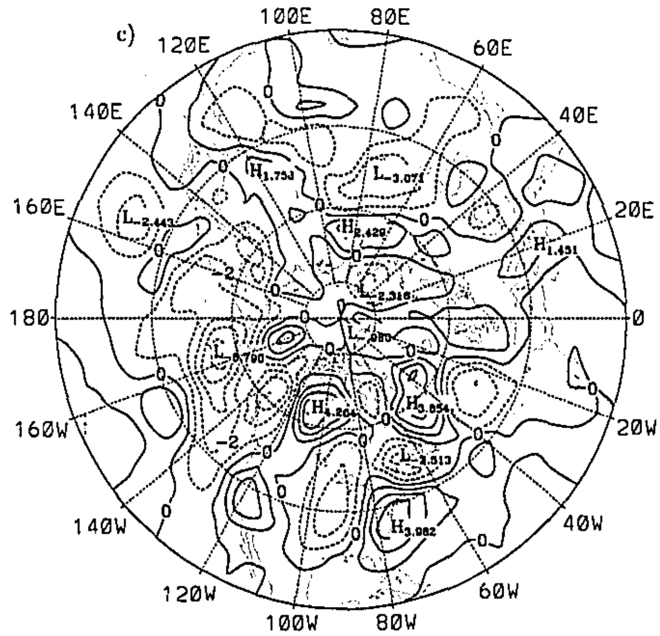

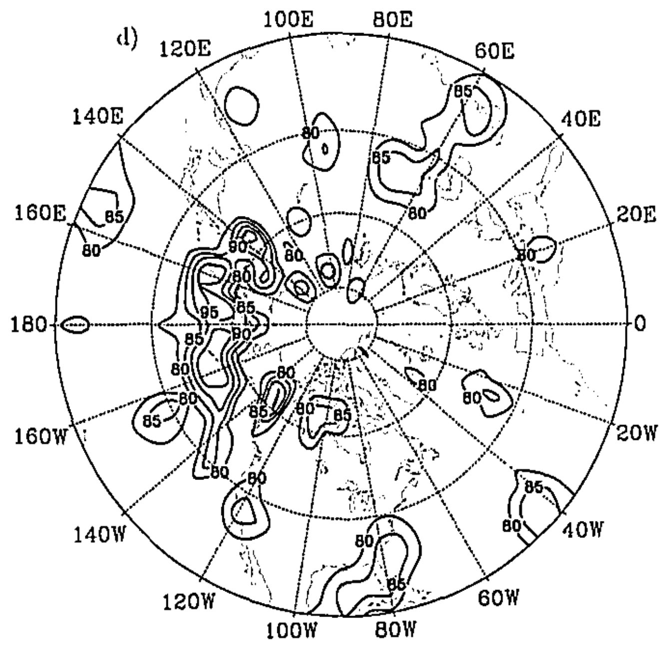

Figure 3.14: Continued.

As discussed in Section 2.7, the thermal variance tendency associated with the vertical motion $\overline{T_l \mathcal{B}_l}$ tends to partially offset the effect of the horizontal advection through the sinking (warming) of the cold air and the rising (cooling) of the warm air. This term and $\overline{T_l \mathcal{C}_l}$ together can approximately balance the generation of the low-frequency thermal variance by $\overline{T_l \mathcal{A}_l}$.

3.8 Summary and discussion

In this chapter, we have analyzed the differences between the El Niño and the non-El Niño winters. Significant differences have been found in the winter seasonal mean flow, the low-frequency eddies and the synoptic-scale transients. Special attention has been paid to the difference in the extratropical low-frequency variabilities and the mechanisms supporting them.

During the El Niño winters, the above normal eastern equatorial sea surface temperature (e.g., Rasmusson and Carpenter, 1982) is accompanied by an enhanced PNA pattern in the seasonal mean geopotential height field. The most striking feature is the deepening of the Aleutian low over the North Pacific, and the eastward extension of the subtropical Pacific westerly jet. The low-frequency eddy activity is observed to be reduced in the North Pacific during the El Niño winters. Also the persistent, large-amplitude anomalies in this area are found to be less frequent. The high-frequency baroclinic wave activity during the El Niño winters is shifted southward from its normal position along the extended westerly jet.

Two mechanisms account for the decrease of the low-frequency transient activity over the North Pacific during the El Niño winters. Normally in the region downstream of the subtropical westerly jet, the seasonal mean flow supplies kinetic energy to the low-frequency transients through barotropic processes. In addition, the low-frequency eddies extract kinetic energy from the synoptic-scale transients through their interactions over the northeastern ocean basins. When an El Niño event occurs, both the above energy supplies to the low-frequency transients are considerably reduced over the North Pacific. The reduction in the barotropic energy transfer from the mean flow appears to be related to the decrease in the longitudinal gradient of the basic zonal flow ($\partial\overline{u}/\partial x$) over the western and central Pacific. Also, during the El Niño years the strong seasonal mean Aleutian low tends to keep the baroclinic synoptic-scale eddies moving along its southern side, leading to only weak interactions between the high- and low-frequency eddies over the northern Pacific and thus to less synoptic-scale eddy forcing.

The reductions in the barotropic energy transfer and the transient eddy forcing of the low-frequency eddies imply that the interactions between eddies of different time scales are less active during El Niño winters, at least over the North Pacific region. In this case, the atmospheric internal processes which may cause anomalous seasonal mean flows become less important, and thus we may expect the atmospheric response to an external forcing to be potentially more predictable. Cubasch (1985) investigated a GCM response to the equatorial sea surface temperature anomaly related to El Niño events by a number of 150-day integrations. He found that in the presence of positive equatorial sea surface temperature anomalies in the eastern Pacific, a significant response in the extratropical Northern Hemisphere was generated which resembles the PNA pattern. However, when the model was integrated with the sea surface temperature anomalies of equal amplitude but of opposite sign, the response was not statistically significant over the North Pacific. Our result may be a possible explanation of Cubasch's findings. With a positive PNA response, or negative geopotential anomalies over the North Pacific, the atmosphere is forced to a state similar to that which we have examined in this study. On the other hand, with a positive geopotential anomaly over the North Pacific, the general circulation may be forced towards a state where more kinetic energy is converted from the mean flow to the low-frequency transients and for which there are more active interactions between the high- and low-frequency eddies. In the latter case, the atmospheric internal processes may be too strong to yield a significant time-mean forced response.

It should be kept in mind that the results presented in this study are based on data which cover a short period of two decades. Only six major El Niño events are composited for comparison with the other winters. Some degree of caution is needed in interpreting the results. Variability exists in the wintertime extratropical response to different El Niño events. Some features in the composite of the six El Niño events may be biased toward the stronger ones. However, there do exist common features among the extratropical circulations in those El Niño winters, as is shown in Figs. 3.3c and 3.4c, and the t-tests performed in the study suggest that the main features of the anomalies are statistically significant.

Chapter 4

Variation in Predictability in Relation with the Low-frequency PNA Pattern

4.1 Introduction

As pointed out by Lorenz (1963, 1969), there is a limit to the predictability of the atmosphere due to the growth of errors which results from the imperfect knowledge of the initial conditions, even if the governing equations are deterministic and are perfectly known. Charney et al. (1966) concluded, on the basis of three existing general circulation models, that the limit of predictability is about two weeks for synoptic-scale or larger-scale flows.

Efforts have been made to reduce the influence of the initial errors on predictions. As suggested by Charney (1960), the limit of predictability may be extended by taking a spatial or temporal average of the predictions. This can be explained by the fact that the large-scale field does not change rapidly, and that the initial errors grow less rapidly for lower frequency components (Lorenz 1969). Epstein (1969) proposed the use of a stochastic-dynamic forecast to predict the state of the atmosphere and to measure the uncertainty in the forecast. Leith (1974) discussed the Monte Carlo approach which takes an average of several perturbed forecasts. Recently a two-member ensemble method was used to improve the quality of the forecasts (Toth and Kalnay, 1992; Houtekamer and Derome, 1994).

In the last chapter, we have seen that the atmospheric internal processes that cause the slowly-varying fluctuations in the atmosphere vary in intensity from year to year. This may lead to an interannual variation in the atmospheric predictability. We have seen that the interactions between the eddies are weaker over the Northern Pacific during the El Niño winters and we may then summarize that the atmospheric response to an external forcing is more stable and thus more predictable than during non-El Niño winters.

It would be interesting to study how the growth of initial errors depends on the weather regime. From the assessment of the extended range forecasts of Mansfield (1986) and Miyakoda et al. (1986), and from the medium range forecasts at the ECMWF, Palmer (1988) noted that the skill of numerical forecasts is strongly influenced by the amplitude of the PNA (Pacific/North American) mode of low-frequency variability. He further argued on the basis of barotropic instability that the growth of the initial errors was stronger in a basic flow having a negative PNA index (positive height anomaly over Aleutian Islands) than in a basic flow with a positive PNA index.

Difficulties exist if one wants to use the forecast data from operational models to study objectively the relationships between forecast skill (error) and the low-frequency modes of variability. Although medium range forecasts have been run operationally in some NWP centres such as the ECMWF for several years, a homogeneous dataset covering many years is still not available. Usually the forecast systems in NWP centres are modified from time to time, which makes it very difficult to separate the effect of low-frequency variability from that of model improvements on the forecast skill.

In this chapter we use a simple three-level quasi-geostrophic model which allows us to perform a large number of forecast experiments. Our primary objective is to examine the growth of errors in different weather regimes. The Pacific/North American (PNA) pattern (Wallace and Gutzler, 1981) is one of the most important low-frequency modes in the atmosphere. We will compare the predictability and the systematic error pattern in its positive and negative phases. We will also investigate the physical explanation for the error growth by analyzing the development of the transients with time scales of 10–90 days.

4.2 The model

The model used in this study is the spectral, three-level quasi-geostrophic model developed by F. Molteni at the ECMWF (Marshall and Molteni, 1993). It has a global domain and pressure as the vertical coordinate. The horizontal resolution of the model is triangular 21 (T21). The prognostic equations for the quasi-geostrophic potential vorticity at 200, 500 and 800 hPa are in the form of

$$\frac{\partial q_i}{\partial t} = -J(\psi_i, q_i) - D_i + F_i, \tag{4.1}$$

where the index i=1, 2 or 3 indicates the 200, 500 and 800 hPa pressure levels, respectively. The potential vorticity is defined as:

$$\begin{aligned} q_1 &= \nabla^2\psi_1 - R_1^{-2}(\psi_1 - \psi_2) + f; \\ q_2 &= \nabla^2\psi_2 + R_1^{-2}(\psi_1 - \psi_2) - R_2^{-2}(\psi_2 - \psi_3) + f; \\ q_3 &= \nabla^2\psi_3 + R_2^{-2}(\psi_2 - \psi_3) + f(1 + \frac{h}{H_0}), \end{aligned}$$

where $f = 2\Omega sin\phi$, R_1(=700 km) and R_2(=450 km) are the Rossby radii of deformation for the 200-500 hPa layer and the 500-800 hPa layer, respectively. h is the orographic height and H_0 a scale height (9 km).

The dissipative terms D_1, D_2, and D_3 include the effects of a Newtonian relaxation of temperature, linear drag on the 800 hPa wind, and horizontal diffusion of vorticity and temperature. The temperature relaxation has an e-folding time scale of 25 days. The linear drag on the lower-level wind has a time scale of 3 days over the oceans, 2 days over the low-altitude land and 1.5 days over mountains above 2 km. A scale-selective horizontal diffusion in the form of $c_d\nabla^8 q_i$ damps harmonics of total wavenumber 21 on a 2 day time scale.

The potential vorticity forcing terms F_1, F_2, and F_3 are chosen so that the model has a reasonable climatology. To do so, we presume that the model can reproduce both the mean flow and transients of the real atmosphere, and use observations to compute the forcing field. Doing a time average of equation (4.1), we get

$$\overline{\frac{\partial q_i}{\partial t}} \;=\; -\overline{J(\psi_i, q_i)} - \overline{D_i} + \overline{F_i}, \tag{4.2}$$

where i=1, 2, 3, and the overbar represents the time average. Over a significantly long period of observations, one would expect the average potential vorticity tendencies to vanish, so that the external forcing can be obtained through:

$$\overline{F_i} \;=\; \overline{J(\psi_i, q_i)} + \overline{D_i}. \tag{4.3}$$

The F_i fields are computed from the daily (12 GMT) analyses of the European Centre for Medium-Range Weather Forecasts (ECMWF) at the three pressure levels for a period of 9 winter seasons from 1980/81 to 1988/89, where the winter is defined as December, January and February. We then computed the time average of the F_i fields and assume, in (4.1) that $F_i = \overline{F_i}$, that is, we use a time-independent forcing.

4.3 Control run and the "interannual" variability

With the external forcing obtained from the winter observations, a "perpetual winter" integration is performed. After an initial spin-up period of 360 days, model output data are saved once per day for 31485 days. This long-time integration is called the control run. These 31485 days are divided into 300 independent "winters" of 90 days by omitting the 15 days between consecutive 90 day periods. Also the long-time integration will serve as a reference atmospheric state which is also called the "truth". It is against this reference state that all predictability experiments discussed in the later sections will be compared. The model output in streamfunction is converted into geopotential height using the linear balance equation.

4.3.1 The model climatology

If the time-independent external forcing F_i in (4.1) is defined appropriately, we should expect the long-time integration of the QG model to reproduce the observed wintertime mean flow and transients in a realistic way. It is important in our study that the model can reproduce a reasonably realistic climatology, especially the planetary-scale troughs over the east coasts of Asia and North America, which lead to localized regions of instability. Then the low-frequency circulation patterns which resemble those of the atmosphere to some extent may be expected.

Figs. 4.1a and b show the simulated and the observed mean 500 hPa streamfunction fields for the Northern Hemisphere, respectively. The distribution patterns are generally in agreement. The model is able to simulate the planetary-scale stationary waves in quite a realistic way, except that the amplitude of the North European trough is overestimated.

In order to discern the low-frequency eddies and the synoptic-scale transients, the same Fourier filters as described in Section 2.2.1 are applied to those time series of data for each 90-day "winter". The synoptic-scale transients have a frequency range corresponding to periods between 2 and 10 days, while the low-frequency eddies have periods from 10 to 90 days. Fig. 4.2 shows the standard deviations of the geopotential height at 500 hPa for the low- and high-frequency eddies from the model and the observations. From Figs. 4.2a and b, it is seen that the distribution of the simulated low-frequency standard deviation is in general agreement with the observations. The two maxima over the northeast Pacific and the north Atlantic are reproduced well. However, the large values of the model low-frequency rms are somewhat too localized. From the distributions of the high-frequency standard deviation (Figs. 4.2c and d), we see that the two storm tracks have been simulated. The shape of the Pacific storm track is reasonable, but its eastern extension is too strong. The high-frequency

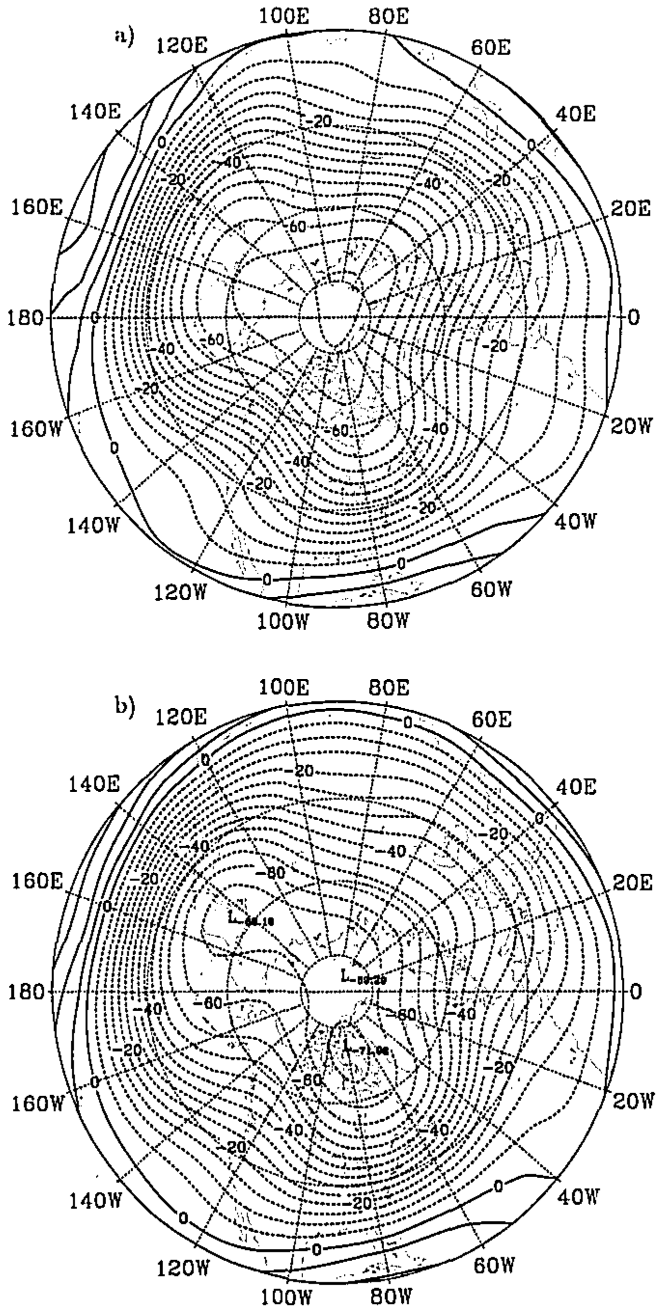

Figure 4.1: (a) Streamfunction at 500 hPa averaged for 300-winter integrations of the QG model; (b) Observed 500 hPa streamfunction averaged for nine winters from ECMWF data. The contour intervals are $5 \times 10^6 \mathrm{m}^2\ \mathrm{s}^{-1}$.

variability in the Atlantic is located too far to the northeast. The distributions of the standard deviation of the total transient for the model and the observations are presented in Figs. 4.2e and f, respectively. Here the effect of the low-frequency eddies is dominant.

We conclude that the model has realistic stationary planetary waves and that the broad climatological characteristics of the transients are generally in agreement with the observations. We consider that the differences between the model results and the observations are relatively minor and acceptable, since it is not our purpose to reproduce perfectly every aspect of the observed climatology.

4.3.2 Simulated "seasonal" anomalies

Our purpose is to study some aspects of atmospheric predictability in different circulation patterns. It will be important that the model be able to simulate the main features of important anomaly patterns that are observed in the atmosphere.

The PNA pattern describes one of the most significant teleconnections in the atmosphere (Wallace and Gutzler, 1981). As discussed in Chapter 3, the PNA pattern is well correlated with the ENSO. In this study we will focus on the PNA pattern to investigate the dependence of the predictability on the evolution of this circulation pattern.

One way to describe the variability of the PNA pattern is to use the PNA index. The PNA index is calculated for the "seasonal" mean flow (90 day average), and is defined following Wallace and Gutzler (1981) as

$$\begin{aligned} \text{PNA Index} \; = \; & \frac{1}{4}[z^*(20°\text{N},160°\text{W}) - z^*(45°\text{N}, 165°\text{W}) \\ & + z^*(55°\text{N},115°\text{W}) - z^*(30°\text{N},85°\text{W})], \end{aligned} \tag{4.4}$$

where z^* represents a departure of a particular "winter" season (90 days) from the 300 "winter" mean 500 hPa height for that grid point, normalized by the local standard deviation of that departure. The positive (negative) PNA index is associated with negative (positive) height anomalies over the North Pacific and Florida and positive

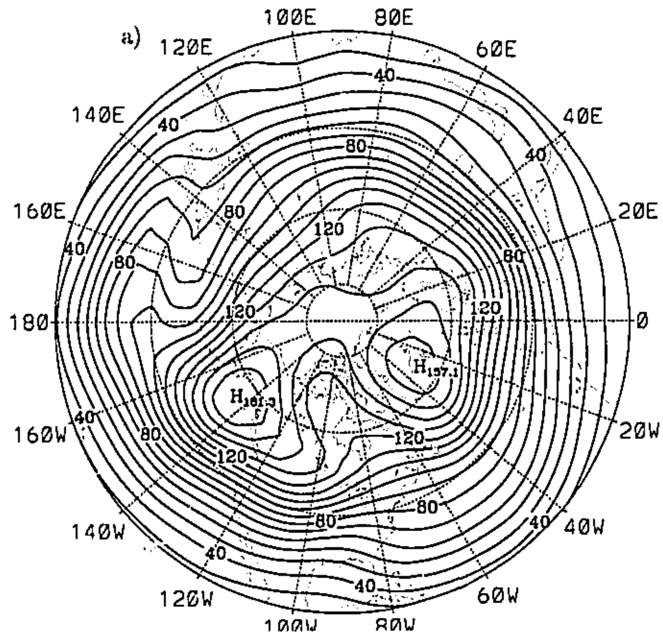

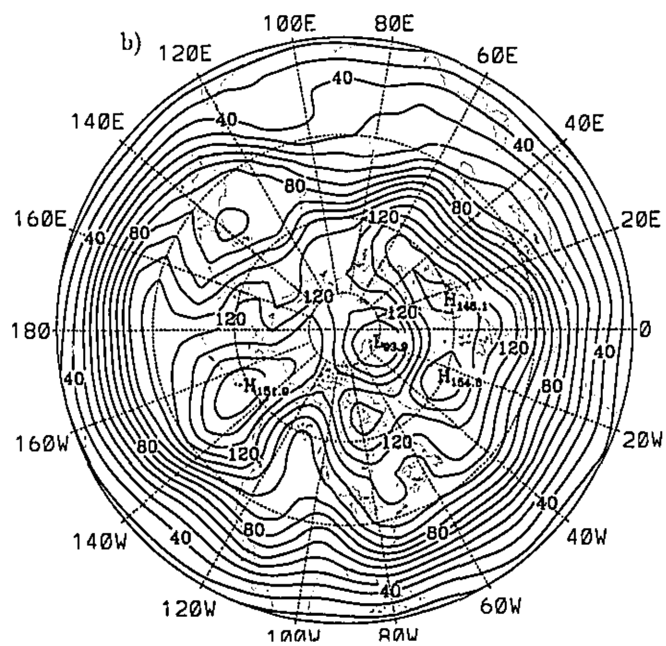

Figure 4.2: Standard deviation of the low-frequency height field computed from (a) the QG model, and (b) the observations. (c) and (d) as in (a) and (b) but for the high-frequency height field. (e) and (f) are for the total transient. Intervals are 8 m for (a)-(d) and 16 m for (e) and (f).

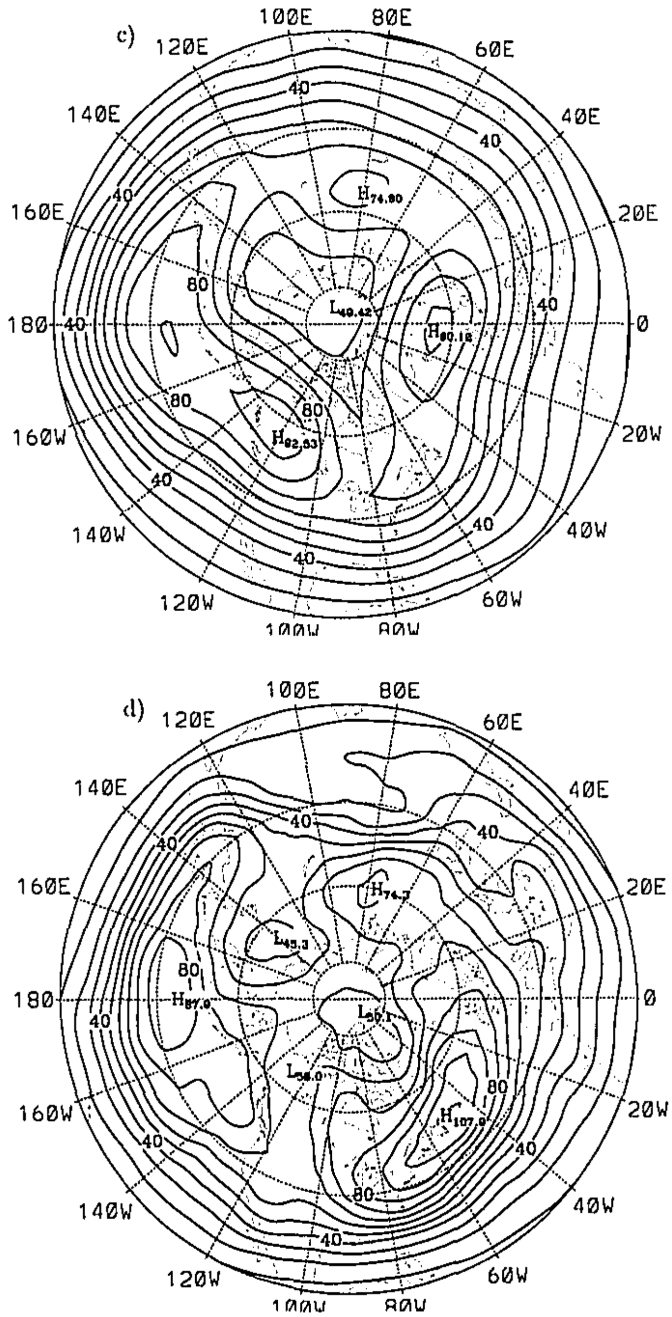

Figure 4.2: Continued.

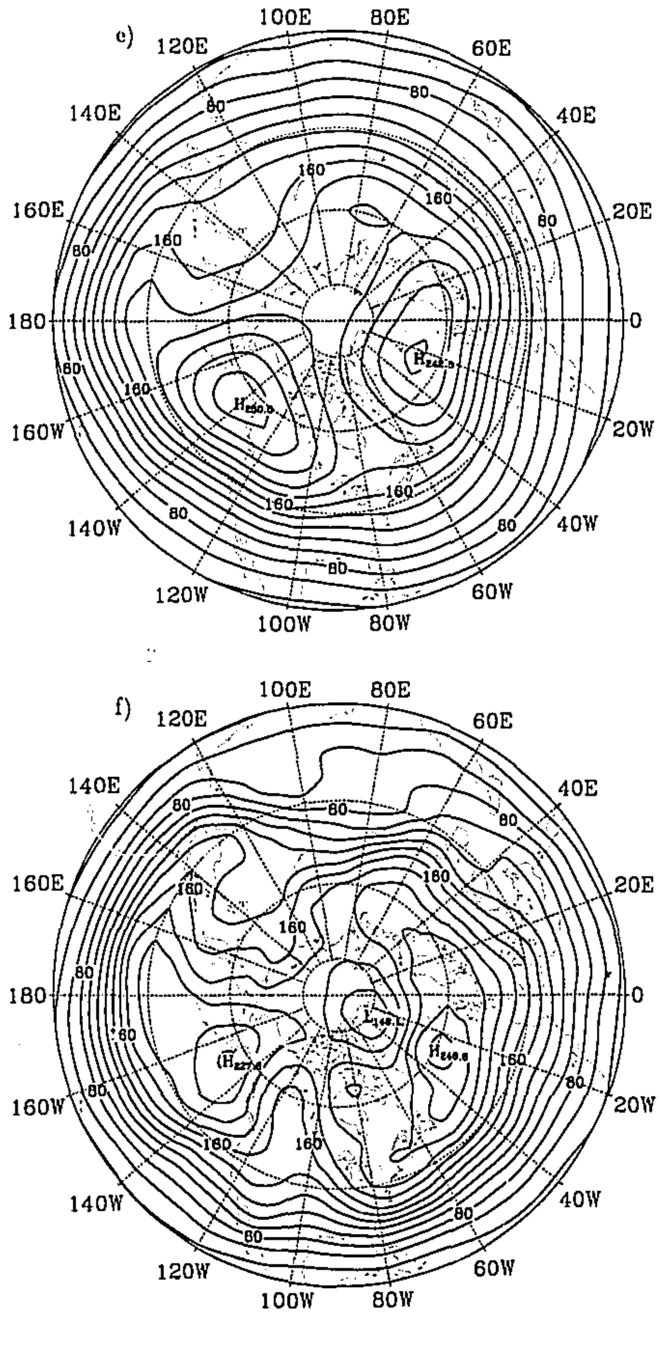

Figure 4.2: Continued.

(negative) height anomalies over Hawaii and Alberta. The time series of the PNA index is displayed in Fig. 4.3. We can see a strong interannual variability of the PNA index over the 300 "winters".

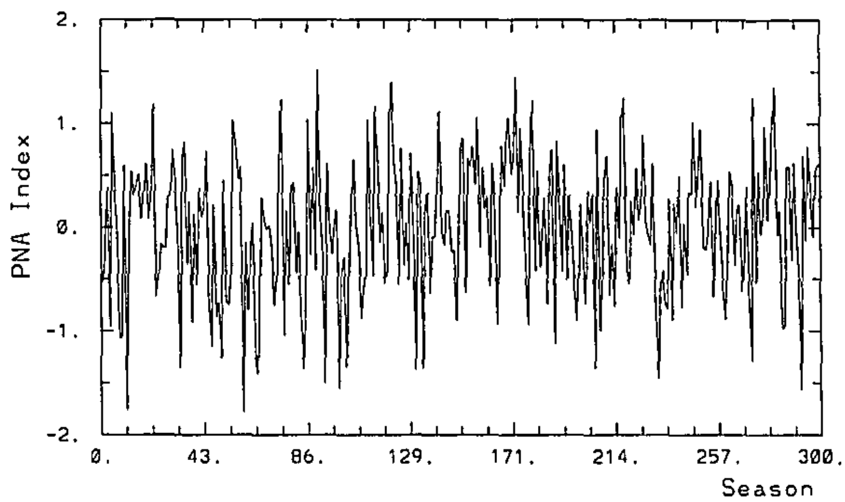

Figure 4.3: The interannual variation of PNA index calculated from a 300 perpetual winter integration.

In order to demonstrate the difference of the atmospheric states between the "winters" with positive and negative PNA indices, in the following we present the differences between them in the seasonal mean flow, the low-frequency variabilities and the synoptic-scale transients. Separate composites are made for the "winters" with extreme positive and negative PNA indices. The "winters" chosen for the composites are those with the PNA indices larger than $+\sigma$ and those smaller than $-\sigma$, where σ is the standard deviation ($\sigma = 0.68$) of the PNA index time series. We will refer to those "winters" with a PNA Index $> \sigma$ and a PNA Index $< -\sigma$ as those with positive and negative PNA anomalies, respectively. There are 43 "winters" with a positive PNA anomaly and 49 "winters" with a negative PNA anomaly according to this criterion. A student t-test method as used in Chapter 3 is used here to analyze the significance of the difference between the two groups.

Fig. 4.4 shows the difference maps resulting from subtracting the composite of the negative PNA phase from that of the positive phase for the "seasonal" mean 500 hPa geopotential height, the low-frequency (10–90 days) height rms, the high-frequency (2-10 days) rms and the rms of the total transients. The difference map of the composite 500 hPa geopotential height (Fig. 4.4a) clearly shows a PNA pattern, with very high t–test significance level (Fig. 4.4b). During the "winters" with a positive PNA index (negative height anomaly over the Aleutian Islands), the low-frequency eddy activity is weaker in the North Pacific than during "winters" of a negative PNA index, and the high-frequency baroclinic waves are shifted to the east and south of their normal position in the Pacific. The difference map of the composite rms of the total transient (Fig. 4.4g) looks similar to that of the low-frequency rms (Fig. 4.4c), indicating that the low-frequency eddies play a dominant role. The results are consistent with the comparison between the observed El Niño and the non-El Niño winters discussed in Chapter 3, indicating that the "interannual" variability can be reasonably well generated internally.

4.4 The forecast experiments

We have seen that the model can produce a reasonably realistic climatology and "interannual" variabilities. The PNA teleconnection pattern on the seasonal time scale has been well simulated. The modifications of the transients with different time scales during the positive and negative PNA phase resemble those in the observations. Thus this model provides a good tool to study the relationship between the predictability and the PNA circulation anomaly.

A "perfect model" approach is used in this study. The perpetual winter control run discussed above will serve as a proxy for the atmospheric observations. Thus 300 independent "winters" are available for the forecast experiments.

Forecast experiments are performed for every "winter". Fig. 4.5 shows schematically the design of the experiment for one "winter". Starting from t_1, each experiment

a)

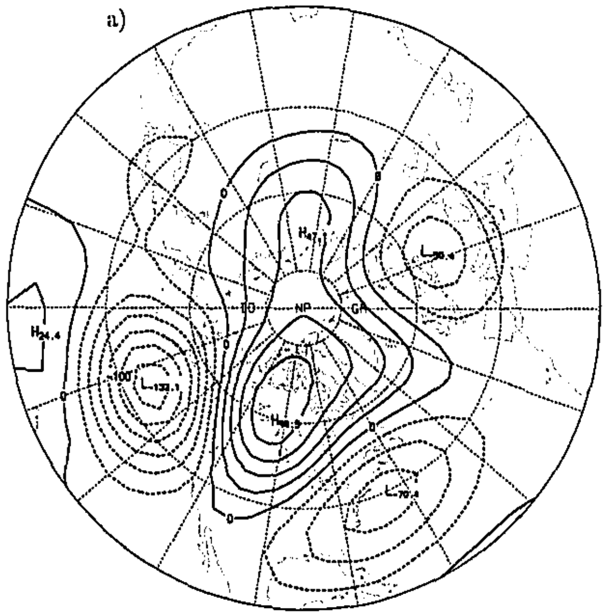

b)

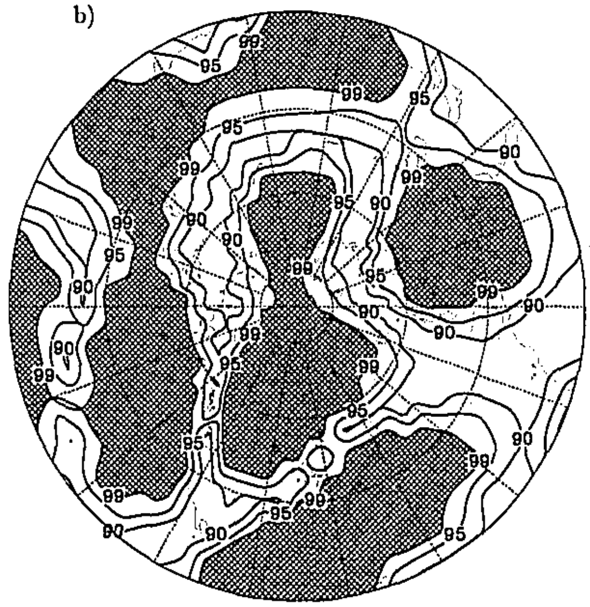

Figure 4.4: Difference maps obtained by subtracting the statistics of model-produced 500 hPa geopotential heights of the negative PNA phases from that of the positive PNA phases for (a) the "seasonal" mean field; (c) the low-frequency standard deviation; (e) the high-frequency standard deviation; (g) the standard deviation of the total transients; (b), (d), (f) and (h) are the significance levels for (a), (c), (e) and (g) from student t-test.

c)

d)

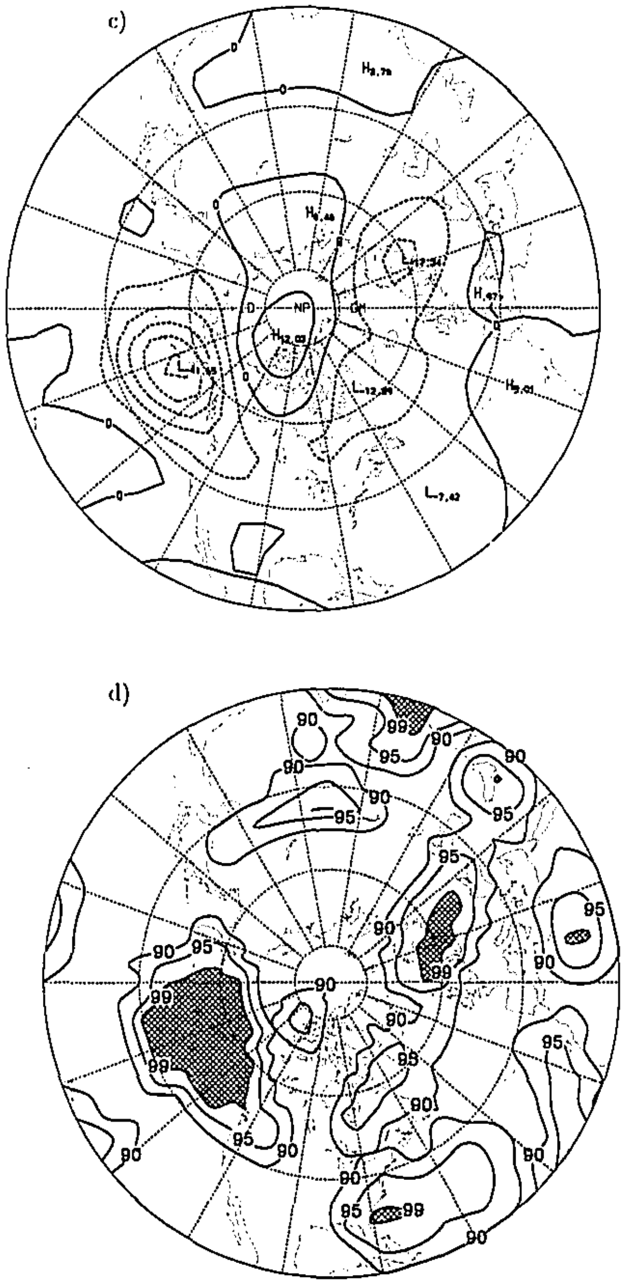

Figure 4.4: Continued.

e)

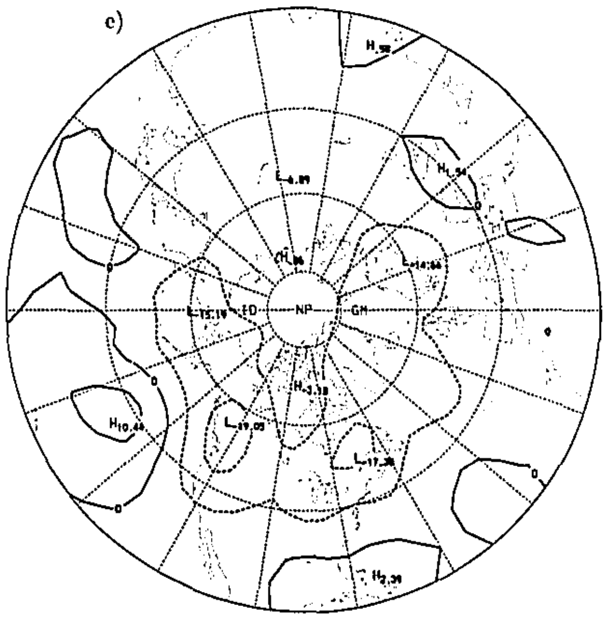

f)

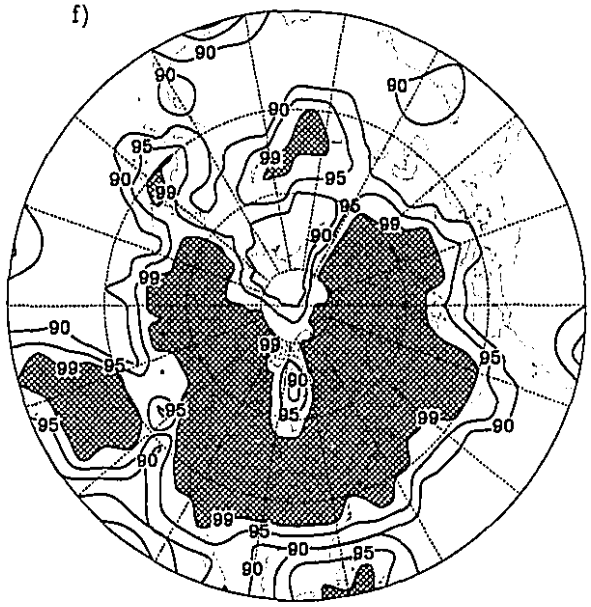

Figure 4.4: Continued.

g)

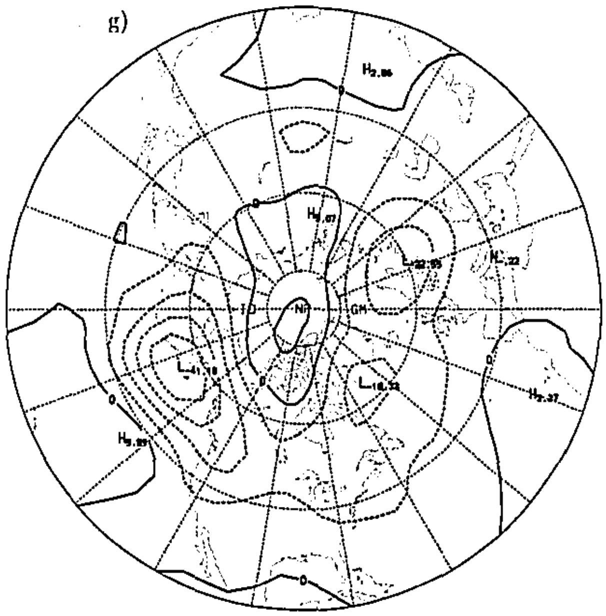

h)

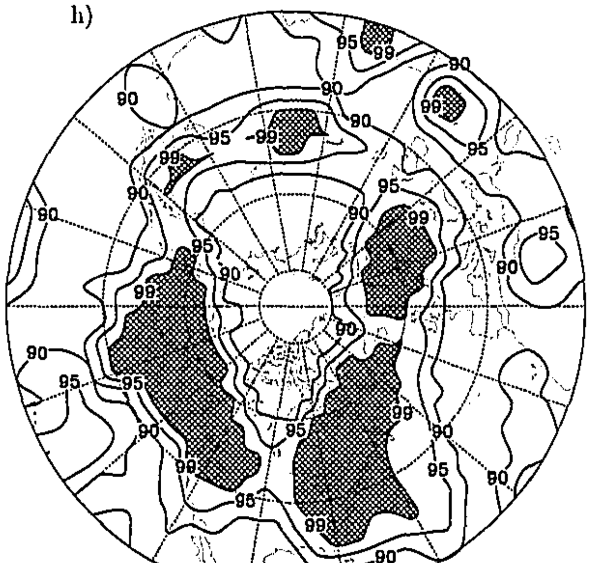

Figure 4.4: Continued.

lasts 15 days. For each "winter" of 90 days, t_1 =day 21 and t_1 =day 65 are chosen. From each t_1, two integrations are performed after adding different perturbation errors to the initial conditions. Thus there are four independent forecast experiments for every "winter". We refer to the two integrations starting from t_1 =day 21 as E1 and E2, and the two experiments starting from t_1 =day 65 as E3 and E4. The number of total forecast experiments is 1200 for the 300 "winters", of which there are 172 predictions for the positive PNA phase and 196 predictions for the negative PNA phase according to the criterion described in the last section.

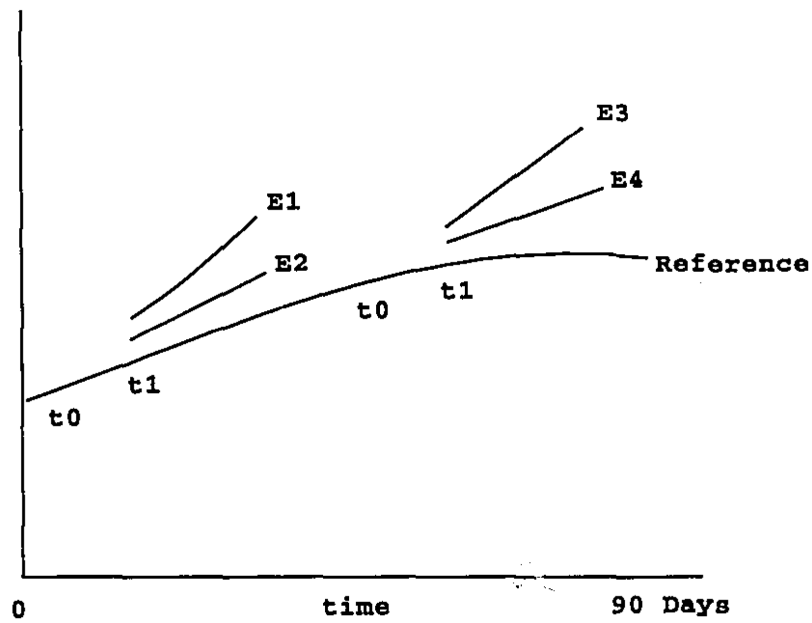

Figure 4.5: Schematic representation of the forecast experiments.

To obtain the initial errors, the breeding method described by Houtekamer and Derome (1994) is used. Starting from t_0, a tangent linear model is initialized with random numbers given to the amplitudes of the spherical harmonic coefficients and integrated to t_1 to obtain the "bred" perturbation. The tangent linear model, which was developed by Houtekamer and Barkmeijer, is the same model used to generate the reference orbit, but now linearized about the reference, time dependent atmospheric state. For each "winter", t_0 is set to be day 1 for t_1 =day 21 and day 45 for

t_1 =day 65, respectively. Thus to obtain the bred mode, the tangent linear model has been integrated for 20 days. The nature of the bred modes have been discussed by Houtekamer and Derome (1994). By the introduction of random perturbations at t_0 and integrating for 20 days, the bred modes are the fastest growing perturbations in the model over that 20-day period.

The "bred" perturbation streamfunction is scaled to have a globally and vertically integrated rms value equal to 10% of the model climatological rms value of the transient part of the streamfunction. The latter was obtained from a previous 5-year integration of the model and found to be 2.5×10^{-3} in the units of $2\Omega a^2 = 0.59\times10^{10}\text{m}^2/\text{s}$, where Ω is the angular velocity of the earth and a the earth's radius. At t_1, the perturbation is added to the reference state to yield the initial condition for a perturbation experiment. If ψ_T represents the "true" value of the streamfunction, as given by the reference orbit in Fig. 4.5, and ψ_E is the analysis error which is simulated by the bred mode, the initial state for the forecast experiment is then given by

$$\psi_F(t=0) \;=\; \psi_T(t=0) + \psi_E. \tag{4.5}$$

As for the control run, the forecast streamfunction is saved once per day.

4.5 Mean forecast error

In order to give a general comparison of the forecasts and the "observations", we first present the error features averaged for the 1200 forecasts. Because a "perfect model" approach is used, a systematic modeling error averaged for the 1200 forecasts should not exist. A common way to measure the error growth is the error variance of the forecasts, which is defined as:

$$E \;=\; <(\psi_f - \psi_o)^2>, \tag{4.6}$$

where ψ_f is the forecast streamfunction and ψ_o is the corresponding "observed" streamfunction, the angle brackets indicating a global and vertical average.

Fig. 4.6 shows the forecast error variance averaged over the 1200 forecasts as a function of time. The vertical bars represent the standard deviation among the 1200 forecasts. The model forecasts show considerable variability in the forecast skill. The horizontal dashed line represents the climatological variance value of the transient part of the streamfunction. It can be seen from the figure that the forecast error variance reaches the climatological value at about 12.5 days.

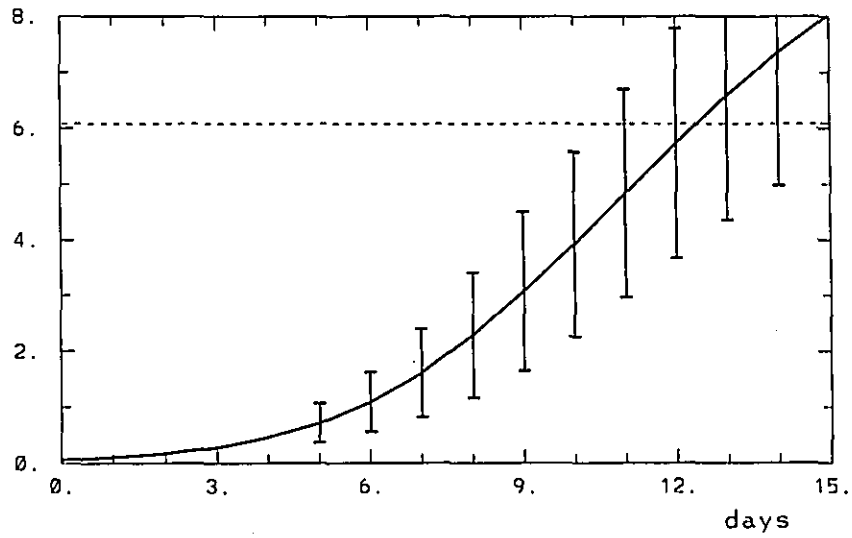

Figure 4.6: The streamfunction forecast error variance in units of 10^{-6} averaged over 1200 forecasts as a function of the forecast length. The vertical bars represent the standard deviation among the experiments at that time. The horizontal dashed line is the climatological variance value of the transient part of streamfunction.

To see the distribution of the forecast error, the rms of the 500 hPa geopotential height error is calculated. At a grid point at 500 hPa, the rms error is defined as:

$$E_{rms} = \left(\frac{1}{N-1} \sum_{i=1}^{N} (\overline{Z_f} - \overline{Z_o})^2 \right)^{\frac{1}{2}}, \tag{4.7}$$

where $\overline{Z_f}$ is a 5-day averaged forecast geopotential height at 500 hPa and $\overline{Z_o}$ is the corresponding "observed" geopotential height, $N = 1200$ is the total number of experiments.

Fig. 4.7 is the distribution of rms error of the 500 hPa geopotential height averaged over day 6 through 10. The maximum error occurs over the northeast Pacific and north Atlantic. The pattern of the rms error looks similar to the distributions of the low-frequency and the total transient geopotential height standard deviation (as in Fig. 4.2a and e). The low-frequency variability is usually associated with slowly changing systems or persistent anomalies such as large storms that have entered the dissipating stage and become quasi-stationary, slowing moving upper air lows with closed height contours around their centres, and blocking ridges, etc. In other words, the areas of large forecast errors are located in the same regions as blocking ridges and the slowly changing systems. The ability of numerical models to predict such low-frequency systems is in general very poor.

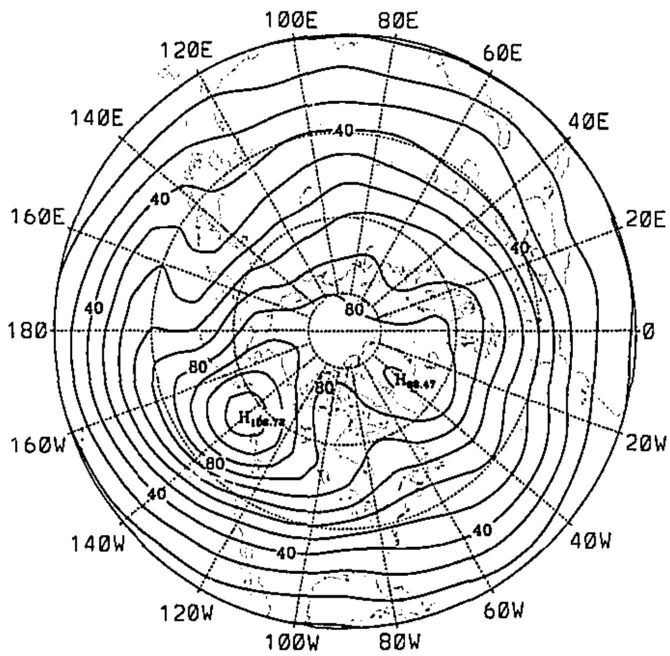

Figure 4.7: Distribution of rms error of 500 hPa geopotential height of 5-day averages for days 6–10. Contour interval is 8 m.

4.6 Error growth in the positive and negative PNA phases

As can be seen from the standard deviation of the error variance among the 1200 forecasts in Fig. 4.6, the model forecasts show considerable variability in forecast skill. Now we turn to investigate the dependence of the forecast skill on the phase of the PNA pattern.

4.6.1 Composite analyses

To show the difference in the error growth between the positive and the negative PNA phases, the forecast error variances are composited for the two conditions. As stated earlier, from the control run of 300 independent "winters", 43 of them are identified as having a positive PNA phase and 49 as having a negative phase.

We have performed 4 forecast experiments (E1, E2, E3 and E4) for each "winter". Composites of the forecast error variance are computed separately for E1, E2, E3 and E4 (each has 300 forecasts). Fig. 4.8 shows the forecast error variances in ψ as a function of time, which is again a globally and vertically averaged quantity as in Fig. 4.6. The solid lines represent the composites for the positive PNA phase, while the dashed lines represent the composites for the negative PNA phase. The thin lines represent the composites of the forecast error variance for E1, E2, E3 and E4, and the thick lines are their averages. Thus the thick dashed and thick solid lines are the composites of the 196 forecasts for the negative PNA phase and of the 172 predictions for the positive PNA phase, respectively. From the thick lines, we see that during the first 6 days the two curves are almost identical. Therefore, for short range forecasts the error growth does not seem to be noticeably dependent on the PNA phase. At about day 6 the two curves start to separate, and their difference develops as time increases. This feature is true for all of E1, E2, E3 and E4 (thin lines). Thus even for a global average, the skill of the medium-range forecasts made during the positive PNA phase is higher than that made during the negative PNA phase.

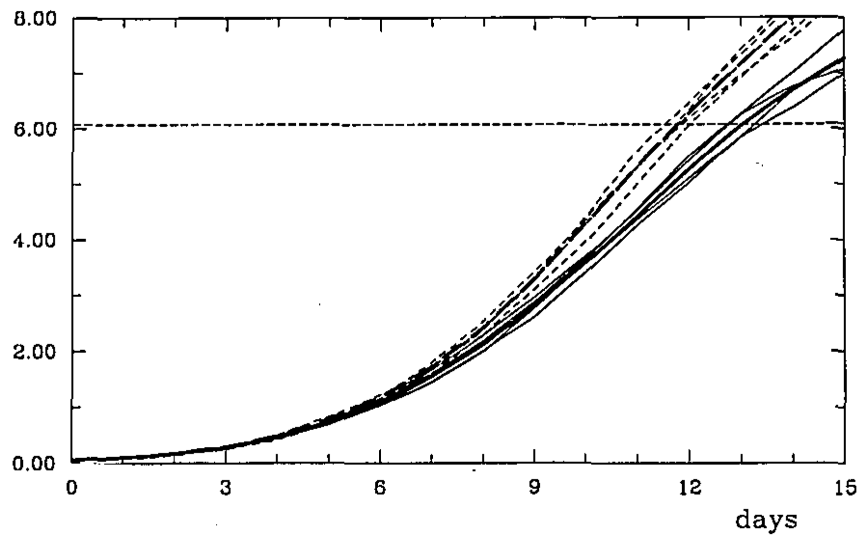

Figure 4.8: The streamfunction forecast error variance in units of 10^{-6} as a function of forecast day for the positive PNA phase (solid lines) and the negative PNA phase (dashed lines). The thin lines represent the composites for E1, E2, E3 and E4, and the thick lines are their averages.

To show the local features of the difference in the error growth between the positive PNA and negative PNA phases, Figs. 4.9a and b depict the rms error distributions of the 500 hPa geopotential height averaged over days 6–10 composited for the positive and negative PNA index winters, respectively. The shaded areas are those where the rms error exceeds 64 m. It can be seen that the rms errors over the North Pacific and adjacent areas are larger during the negative PNA phase than during the positive PNA phase. Also the shaded area which indicates the high rms error over the Northeast Pacific–Alaska is much larger during the negative PNA phase. The difference map (Fig. 4.9c) is obtained by subtracting Fig. 4.9b from Fig. 4.9a. In Fig. 4.9c negative values are found over most of the middle and high latitudes, indicating that the forecast error is smaller during the positive PNA phase than during the negative phase. The maximum difference is located along the latitude belt of 40°–60°N, with two negative centres of high significance levels (Fig. 4.9d) located over the North Pacific and North America.

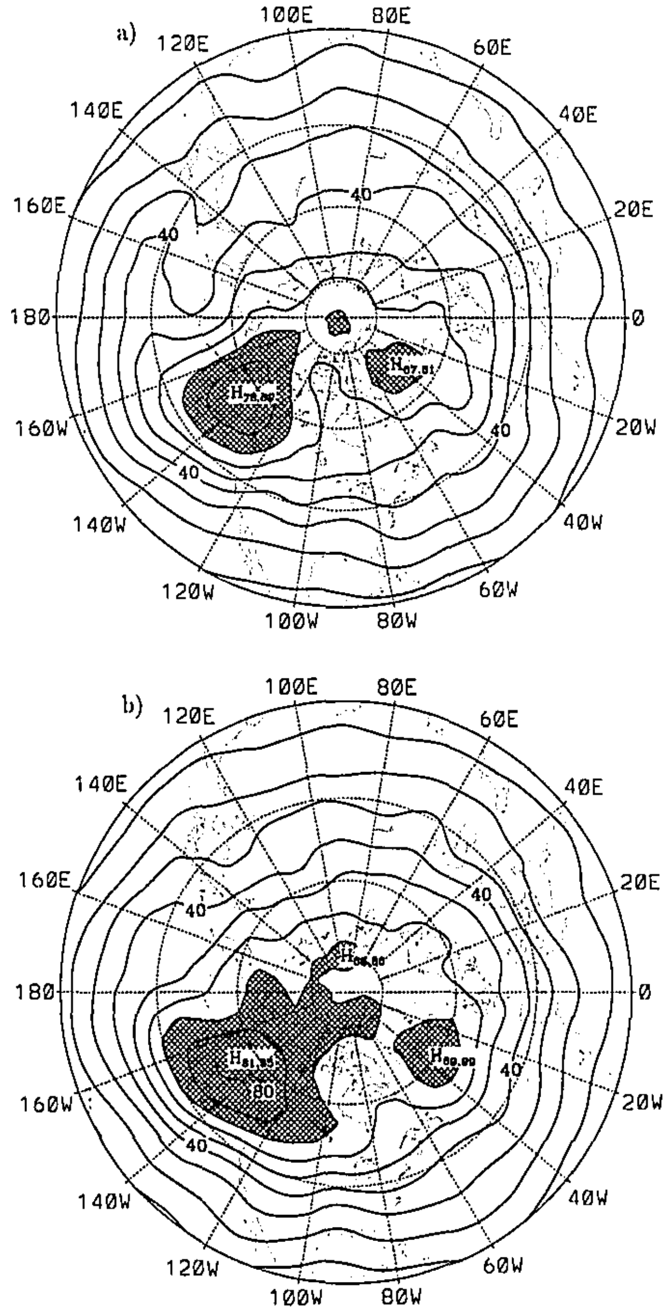

Figure 4.9: Distribution of rms error of 500 hPa geopotential height averaged over days 6–10 for (a) positive PNA phase; (b) negative PNA phase. The shaded areas represent regions with rms error exceeding 64 m. (c) Difference by subtracting (b) from (a). (d)Areas where the systematic errors are different at significance levels of 90%, 95% and 99%. Contour intervals for (a), (b) and (c) are 8 m.

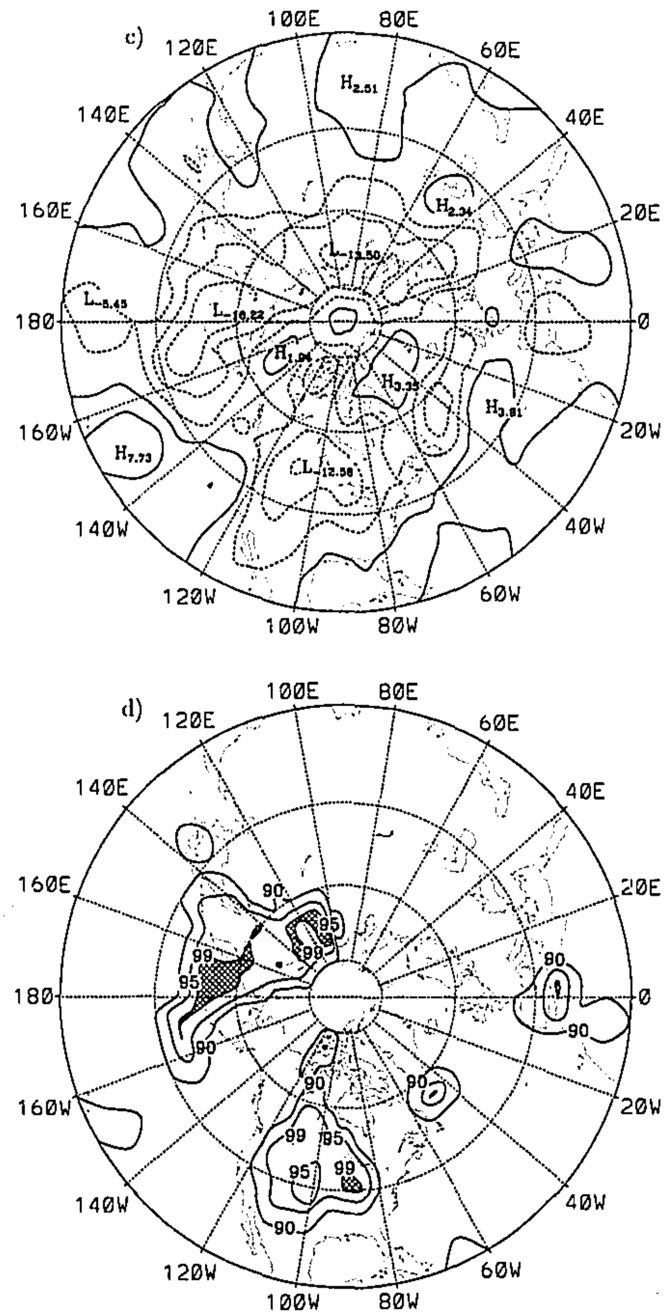

Figure 4.9: Continued.

At later times the error keeps growing. Fig. 4.10 is identical to Fig. 4.10 except that it is for days 11–15. Here the areas where the rms error exceeds 120 m are shaded. The difference between Fig. 4.10a and Fig. 4.10b is more obvious than the difference between Fig. 4.9a and Fig. 4.9b. The shaded areas are much larger in Fig. 4.10b than that in Fig. 4.10a, implying larger forecast error for the predictions during the negative PNA phase. Fig. 4.10c is obtained by subtracting Fig. 4.10b from Fig. 4.10a. From Fig. 4.10c it is seen that the rms error difference has been intensified from Fig. 4.9c and is better organized and has larger scales. A major negative centre is located over the North Pacific, and another one can be found over the North Atlantic. An area of positive values can be found south of 50°N off the west coast of North America, where the forecast error is larger for the predictions during the positive PNA phases than that during the negative PNA phases. The significance levels for the negative centres over the North Pacific and North Atlantic are quite high (Fig. 4.10d).

When the same rms error composites as in Fig. 4.9 and Fig. 4.10 are made for the forecast error averaged for days 1–5 (not shown), almost no difference can be found between the positive and the negative PNA phase. The PNA low-frequency variation indeed has little influence on the short range forecasts. This is in agreement with Palmer and Tibaldi (1986) who found no correlations between the short range forecast skill over the PNA region and the quasi-stationary PNA-like mode of variability of the forecast flow.

We have seen that the error growth depends on the geographical locations. Comparisons are made for the growths of the forecast error variances averaged in four areas. These four areas are referred to as Area I, Areas II, Area III and Area IV, that are indicated in Fig. 4.11. Areas I and IV are located over the North Pacific and North Atlantic, respectively. Area II is over the eastern Pacific off the west coast of North America. Area III is over the North American continent. As can be seen, the four areas cover most of the midlatitude Pacific/North American region and its downstream North Atlantic region, where the PNA mode has the strongest signal.

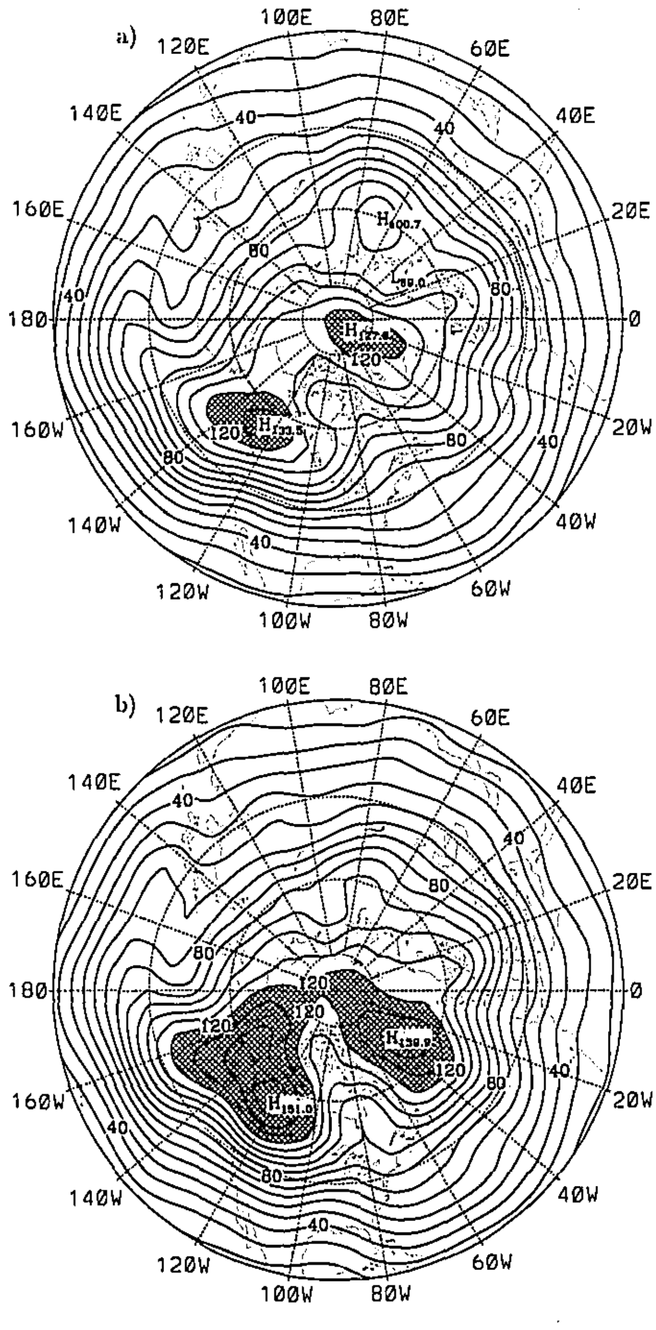

Figure 4.10: As in Fig. 4.9, but averaged over days 11–15. The shaded areas represent regions with rms error exceeding 120 m.

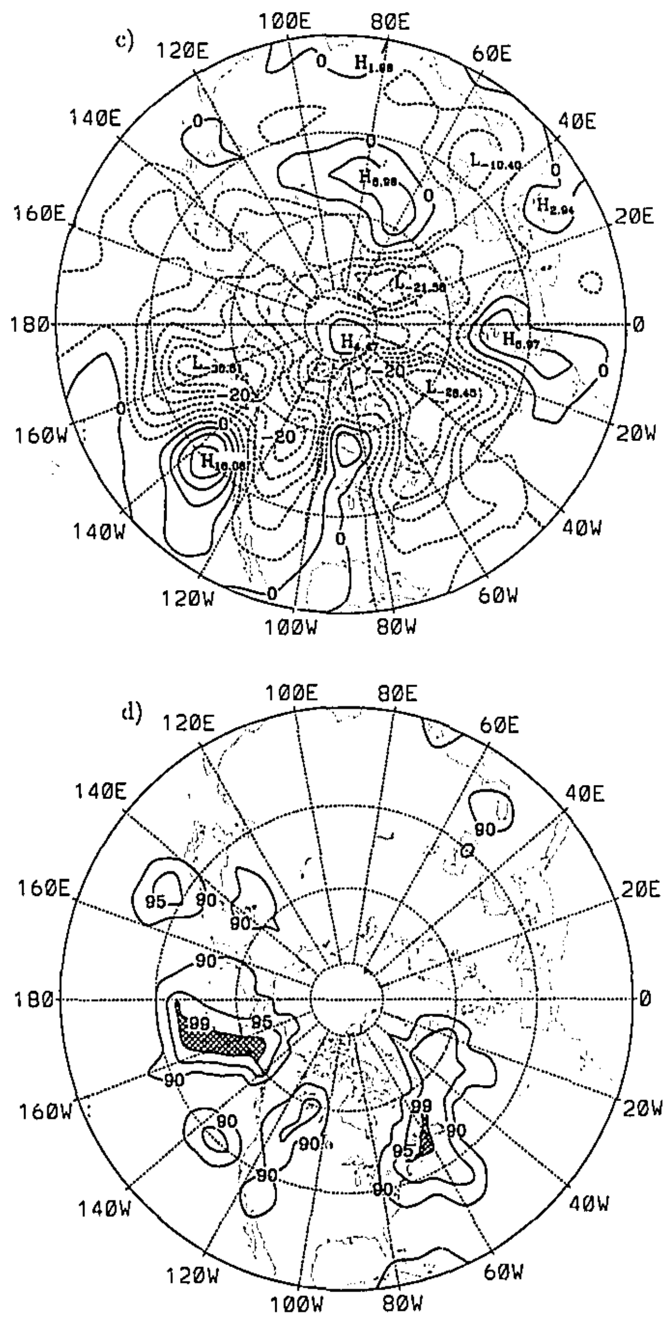

Figure 4.10: Continued.

Comparing with Fig. 4.10c, it is seen that the negative centres in Fig. 4.10c over the North Pacific and North Atlantic are in Areas I and IV, respectively. Area II includes the area of positive values observed off the west coast of North America. The forecast error variance of the streamfunction averaged vertically and over a given area is defined by

$$\psi_{var} = \frac{1}{3N_p}\sum_{k=1}^{3}\sum_{i=1}^{N_p}(\psi_f - \psi_o)^2, \tag{4.8}$$

where N_p is the number of grid points in the given area. The summation over k =1–3 is for the vertical three levels, and the summation over i =1–N_p is for the grid points in the given areas. Composites of the forecast streamfunction error variances are computed separately for experiments E1, E2, E3 and E4 in the four areas. The forecast streamfunction error variances as a function of time in Area I, II, III and IV are shown in Figs. 4.12a, b, c and d, respectively. As in Fig. 4.8, the solid lines represent the composites for the positive PNA phase, while the dashed lines represent the composites for the negative PNA phase.

In Fig. 4.12b, the dashed and solid lines show no clear separations, indicating that in Area II the forecast skill does not seem to have a good relation with the phase of the PNA pattern. The signal related to the positive values in this area in Fig. 4.10c may have been offset by the negative values in the other part of this region.

From Figs. 4.12a, c and d, similar features as in Fig. 4.8 are found. Obviously, the medium-range forecasts after about a week during the negative PNA phases are worse than those during the positive PNA phases. In general, the four experiments E1, E2, E3 and E4 show similar characteristics, reflecting that the result is quite significant. The four solid lines in each figure are quite close to each other. However the dashed lines show large divergence after about day 12. This suggests that the medium-to-long range forecasts are more stable during the positive PNA phases than those during the negative PNA phases.

We conclude that the growth of initial error for the forecasts after about a week is correlated with the PNA phase of the slowly-varying circulation. The forecast error

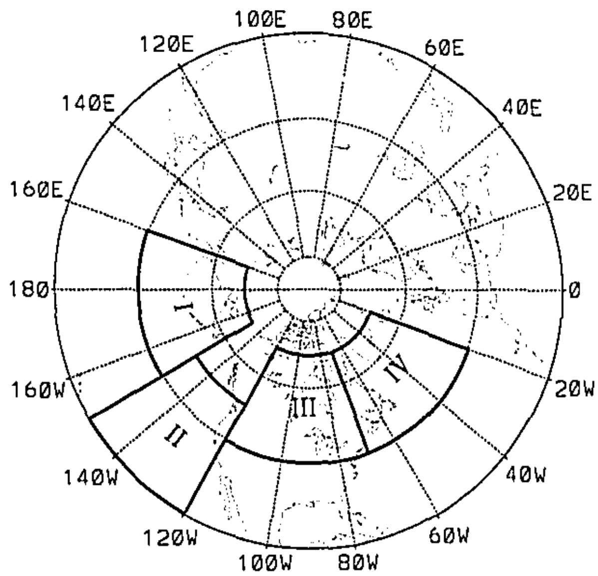

Figure 4.11: Areas to do the comparisons. I: 40–70°N, 160°E–150°W; II: 20–50°N, 150°W–120°W; III: 40–70°N, 120°W–70°W; and IV: 40–70°N, 70°W–20°W.

grows faster during a negative PNA phase than during a positive phase. Thus the forecast skill is better during a positive phase than during a negative PNA phase. This relation is good in the regions of the North Pacific, North America and the North Atlantic. Although some areas have less significance, or may behave differently, there is a signal of the relationship on the global scale.

The above result is consistent with that of Palmer (1988) who analyzed the ECMWF forecast data and found that the skill of the medium range forecasts (day 9) over the Pacific/North American region is strongly correlated with the signed amplitude of the PNA mode.

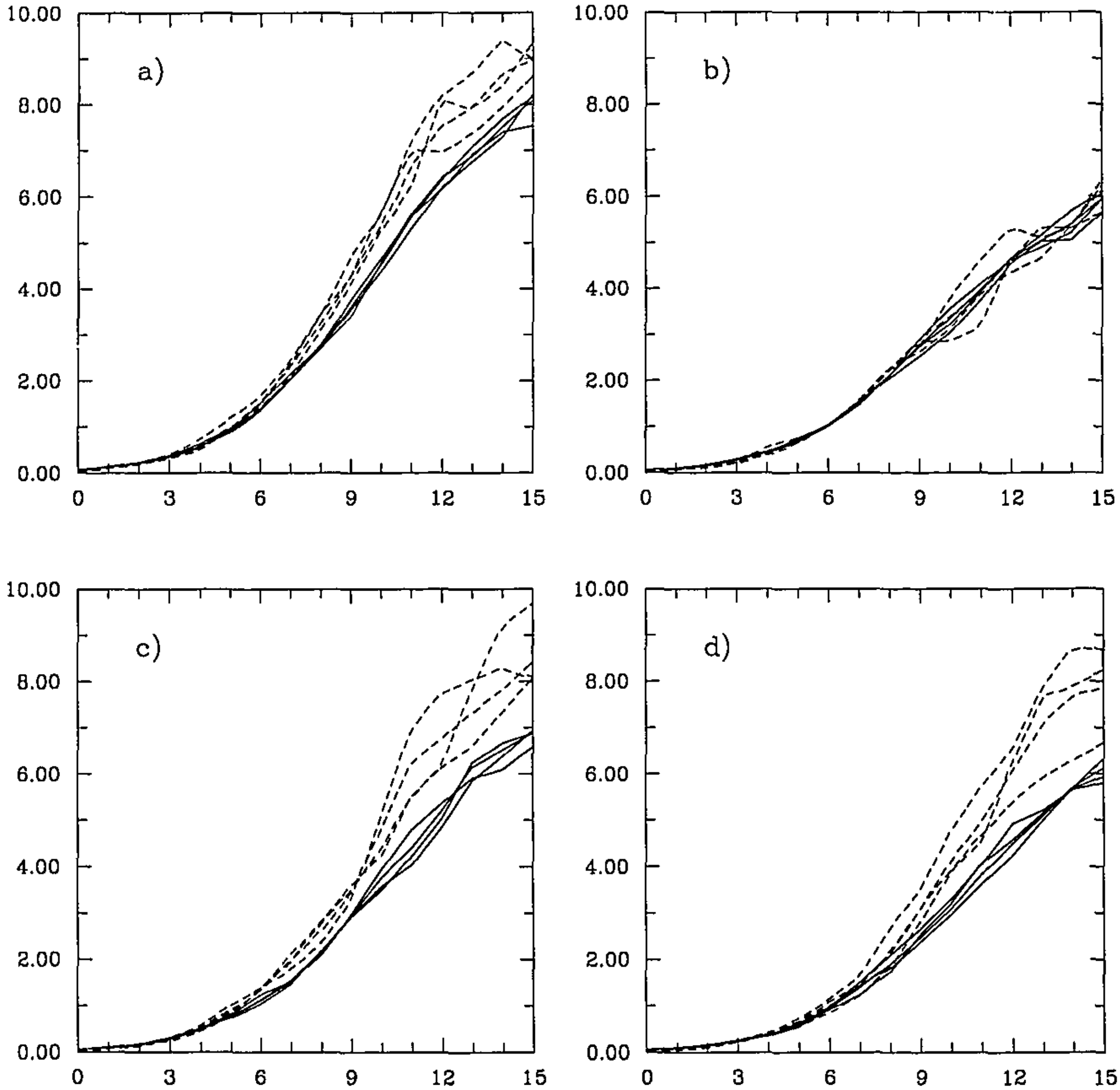

Figure 4.12: The streamfunction forecast error variance in units of 10^{-6} as a function of forecast day for positive PNA phases (solid lines) and negative PNA phases (dashed lines). a), b), c) and d) are for Areas I, II, III and IV, respectively. Composites of E1, E2, E3 and E4 are shown for each area.

4.6.2 Discussion

Considering that the difference between the forecast errors of the positive the negative PNA phases emerges after about 6 days, it is reasonable to believe that the development of the low-frequency eddies plays an important role. Comparing Fig. 4.10c with Fig. 4.2b, it is clear that the difference map of the error patterns between the positive PNA phase and the negative phase is similar to that of the corresponding low-frequency transient rms, suggesting that the weaker intraseasonal fluctuations during the positive PNA phase are related to the smaller rms errors. In the following we discuss the mechanisms behind the "interannual" variability of the low-frequency eddy activity. By understanding why the low-frequency eddy activity is weaker during a positive PNA phase than during a negative PNA phase, we can better understand why the forecast errors are smaller in one situation than in the other.

The output of the 300 "winter" control run is used here to do the analysis. As mentioned in Section 4.3, Fourier filters are used to obtain the low- and high-frequency components of the transients. Thus for a "winter" of 90 days, the flow is decomposed into three parts: the seasonal mean, the low-frequency part and the high-frequency part. The calculations are performed at 500 hPa using the geostrophic relationship to obtain the wind field.

Similar approaches are used here as in Chapter 3 to explain the reduction of the low-frequency eddy activity during the positive PNA phases, i.e. the interactions of the low-frequency fluctuations with the seasonal mean flow and with the high-frequency eddies. In doing so we can also evaluate the internal interactions among eddies of different time scales in the Q-G model and compare them with the observations.

a. Barotropic energy exchange with the seasonal mean flow

One kinetic energy source for the development of the low-frequency eddies is the barotropic energy exchange with the background mean flow. Eq. (3.1) is used here to calculate the barotropic conversion of kinetic energy from the seasonal mean flow to the low-frequency transients.

To see the difference of the barotropic conversion of kinetic energy between the positive and the negative PNA "winters", comparison is made for the composites of C defined in (3.1) for these two cases. Fig. 4.13a shows the distribution of C for the negative PNA "winters". Positive values are found over most of the extratropical regions, indicating that the low-frequency fluctuations are extracting kinetic energy from the seasonal mean flow. The maximum energy conversion occurs in the jet-exit region of the middle Pacific. Another centre of energy conversion is located over the Atlantic jet-exit region. In the case of positive PNA "winters", the maximum barotropic energy conversion in the Pacific is shifted a little to the east and its magnitude is reduced, as may be seen in Fig. 4.13b. The eastward extension of the Pacific westerly jet accompanying the positive PNA causes a reduction of the east-west gradient of the seasonal mean zonal flow ($\partial\overline{u}/\partial x$) in the central Pacific, and therefore results in a reduction in the energy conversion. By subtracting Fig. 4.13a from Fig. 4.13b (Fig. 4.13c), it is clearer that the low-frequency eddies extract less kinetic energy in the central and north Pacific from the background mean flow when the PNA index is positive. A positive area in Fig. 4.13c in the eastern Pacific off the west coast of North America can be found, where the kinetic energy supply from the mean flow to the low-frequency eddies is stronger during the positive PNA phase. The distribution of the kinetic energy transfer difference over the Pacific areas is quite similar to Fig. 4.10c. This suggests that the difference in the kinetic energy transfer from the mean flow contributes to the low-frequency eddy activity difference between the positive and negative PNA phases, and hence to the forecast error difference.

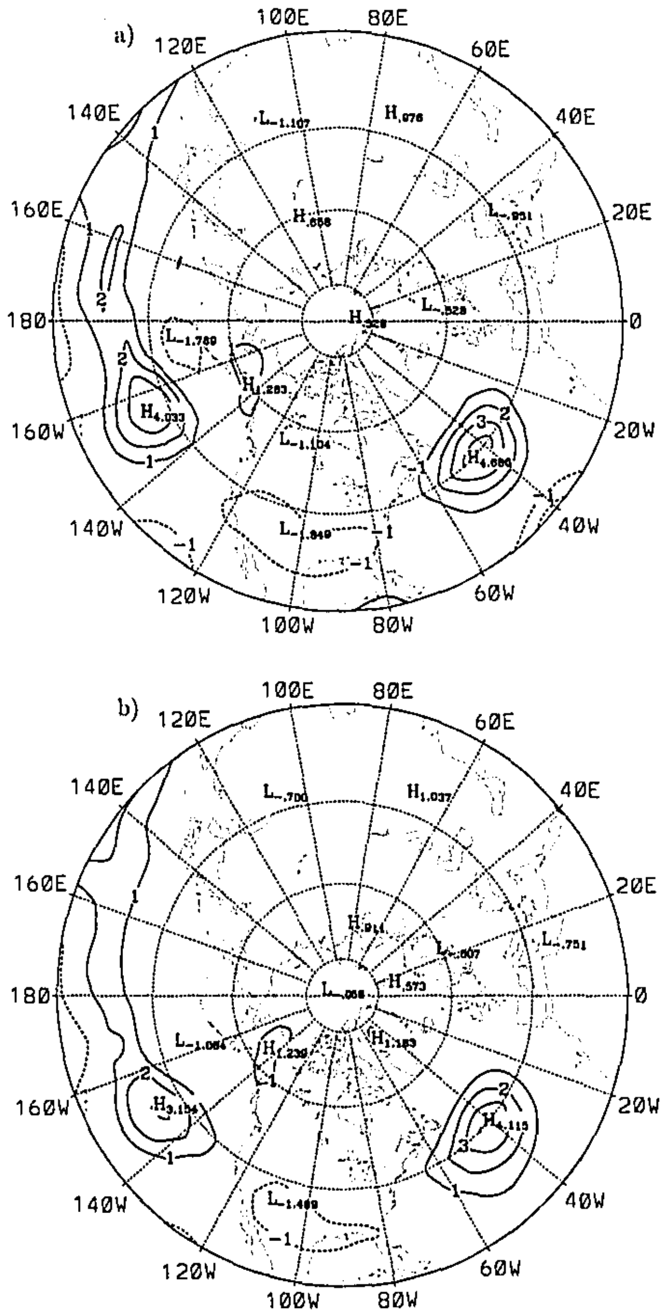

Figure 4.13: Barotropic energy conversion calculated from the 300 winter QG model integration (a) for the negative PNA phases; (b) for the positive PNA phases. (c) The difference by subtracting (a) from (b). The contour intervals are 1×10^{-4} W kg^{-1} for (a) and (b) and 0.5×10^{-4} W kg^{-1} for (c).

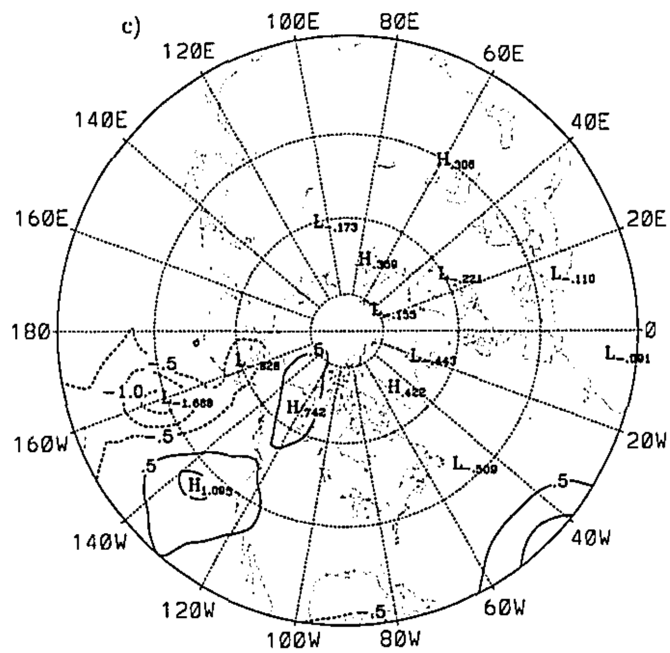

Figure 4.13: Continued.

b. Barotropic high-frequency eddy forcing

Another important mechanism for the development of the low-frequency eddies is their interaction with the synoptic-scale transients. The first term on the right-hand side of Eq. (3.4) is the covariance between the low-frequency geopotential height and the height tendency caused by the vorticity flux convergence by the synoptic-scale eddies, which represents the tendency of geopotential height variance by the barotropic interactions between the low- and high-frequency transients. Here we use this term to express the high-frequency eddy forcing on the low-frequency flows, which can be written as:

$$\overline{z_l \frac{\partial z_l}{\partial t}} = -\frac{f}{g}\overline{z_l \nabla^{-2}\nabla \cdot (\mathbf{V}_h \zeta_h)_l}. \qquad (4.9)$$

Here the calculation is made at 500 hPa. From Fig. 3.6a we can see that the high-frequency thermal forcing is very weak at this level. Therefore, the high-frequency eddy vorticity forcing can approximately represent the net forcing at this level.

The geographic distributions of the covariance between the low-frequency geopotential height and the height tendency caused by high-frequency eddy forcing are shown in Fig. 4.14a and Fig. 4.14b for the negative and positive PNA "winters", respectively, at 500 hPa. It is seen that the covariances are positive throughout most of the extratropics, with two major centres of maximum occuring over the North Pacific and Atlantic, indicating that the vorticity flux convergence by the synoptic-scale eddies is forcing the low-frequency fluctuation. Comparing Fig. 4.14a with Fig. 4.14b, we find that the forcing is stronger in the North Pacific and North Atlantic during the negative PNA "winters". The difference pattern obtained by subtracting Fig. 4.14a from Fig. 4.14b is mapped in Fig. 4.14c. Negative values dominate in the North Pacific and North Atlantic, indicating the high-frequency eddy forcing is reduced during the positive PNA "winters". Over the eastern Pacific an area with positive values is located south of 45°N, implying that the location of the low-frequency forcing by the high-frequency transients is shifted southeastward. Referring to Fig. 4.10c, the negative centres over the North Pacific and North Atlantic and the positive value area in the eastern Pacific all have their similarities in Fig. 4.14c.

We have seen that two mechanisms may be involved to explain the weakness of the low-frequency activity, and the slower growth of errors over the North Pacific, the North American and the North Atlantic areas in medium- to long-range predictions during the positive PNA phase. Firstly, less kinetic energy is supplied to the low-frequency eddies from the large-scale seasonal mean flow because of its modified structure. This mechanism seems mainly to contribute over the Pacific area. Secondly, the strong seasonal mean Aleutian low tends to keep the baroclinic synoptic-scale eddies moving along its southern side, causing only a weak interaction with the low-frequency eddies in the Northern Pacific, and thus less synoptic-scale eddy forcing. During a positive PNA phase, the above normal geopotential heights over North America and the below normal heights to the southeast cause a reduction in the baroclinicity over the east coast of North America and the North Atlantic (Fig. 4.4a).

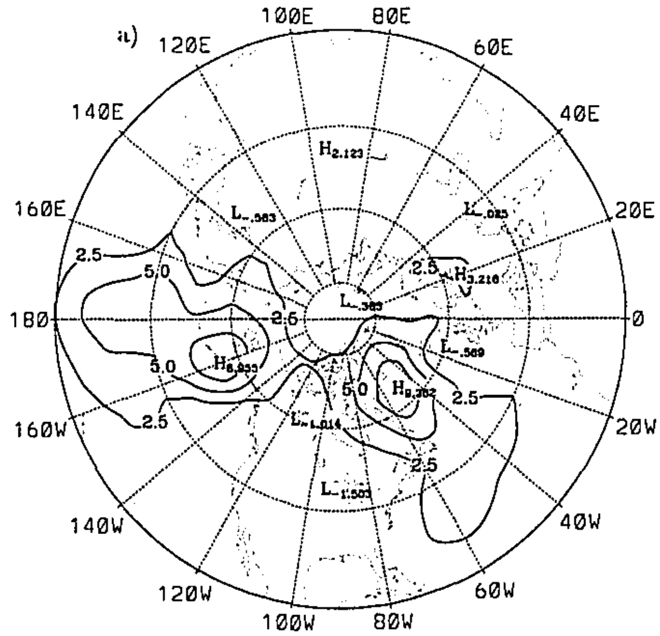

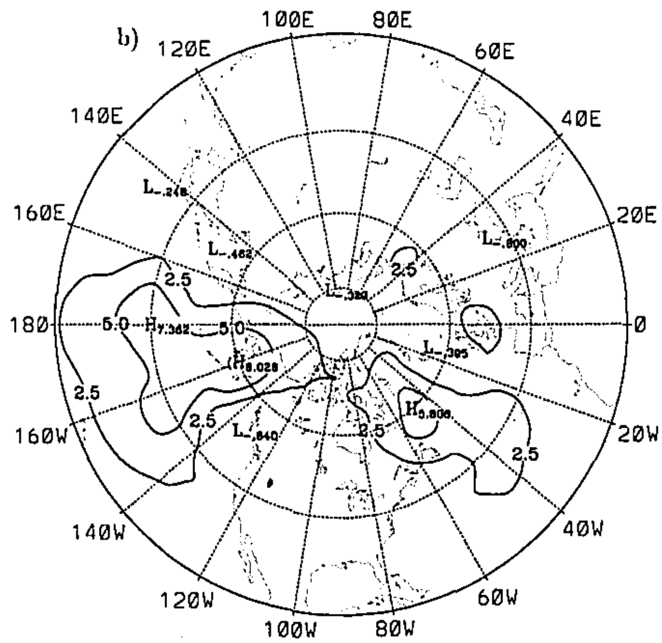

Figure 4.14: Covariance between the low-frequency geopotential height and the synoptic-scale eddy forcing at 500 hPa for (a) the negative PNA phases; (b) the positive PNA phases. (c) Difference by subtracting (a) from (b). The contour intervals are 2.5×10^{-3} m^2/s for (a) and (b) and 1×10^{-3} m^2/s for (c).

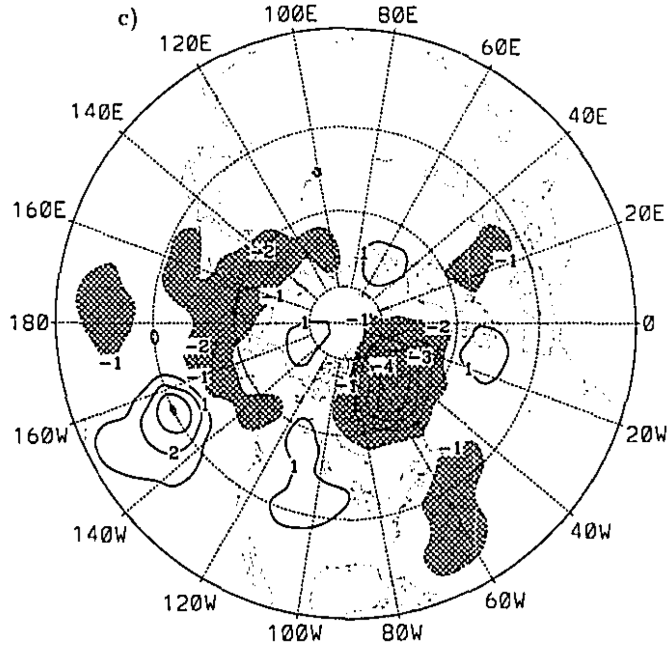

Figure 4.14: Continued.

Thus less active synoptic-scale eddies are expected over the North Atlantic (Fig. 4.4c), and less synoptic-scale eddy forcing to the low-frequency flows. In the case of weak synoptic-scale eddy forcing, an initial perturbation in the low-frequency eddies would develop less fast and lead to smaller forecast errors.

Palmer (1988) investigated the barotropic instability problem for the positive and negative Pacific/North American (PNA) phases, and found that during the negative PNA phase the atmosphere is more unstable to low-frequency disturbances. Medium range forecast errors are therefore more likely to develop during the negative PNA phase. This is in agreement with our first mechanism discussed above in that the kinetic energy transfer from the seasonal mean flow to the low-frequency transients is stronger over the central and northern Pacific during the negative PNA phase than that during the positive PNA phase. From the present study we know that the interaction between the high- and low-frequency eddies is also important for the interannual variability of the low-frequency eddies and the error growth in the forecasts.

Our result is able to reveal and explain the distribution of the error difference between the positive and negative PNA phases. Over the eastern Pacific off the west coast of North America, the kinetic energy supply from the mean flow to the low-frequency eddies is stronger during the positive PNA phases. Also stronger synoptic-scale eddy forcing is observed in this region. These two mechanisms tend to be responsible for a stronger activity of the low-frequency eddies in that region. Indeed the medium-range forecast errors appear to be larger in this area during the positive PNA phases than that during the negative PNA phases (Fig. 4.10c).

The above discussion is in agreement with the results of Chapter 3 where the reduction of the low-frequency fluctuations during El Niño winters using observational data was studied. It can be inferred that the medium range weather forecasts made during El Niño winters, when the circulation pattern tends to be in the positive phase of the PNA, are likely to be more skillful over the North Pacific and North American region than those made during non-El Niño winters. This is of practical importance because the interannual variability of the extratropical circulation related to the El Niño is potentially predictable. Thus making skill predictions of numerical forecasts according to weather regimes seems possible to some extent.

4.7 Systematic error patterns in the positive and negative PNA phases

In this section we compare the systematic error patterns in the 500 hPa height fields during the positive and negative PNA phases. It would be interesting to know the relationship between the systematic error and the phase of PNA pattern, in which case the forecast error could be corrected if we know the amplitude and phase of the PNA pattern during which the prediction is made.

4.7.1 The error pattern

Figs. 4.15 a and b show the systematic error patterns averaged for days 11–15, as obtained from 172 predictions in the positive PNA phase and 196 predictions in the negative PNA phase, respectively. We observe that the error patterns are opposite in sign to the PNA pattern of the reference state, i.e., when predictions are made during the positive (negative) PNA phase the error tends to be a negative (positive) PNA pattern. The difference map (Fig. 4.15c) shows a clear negative phase PNA pattern, with positive errors over the North Pacific and negative errors over the northwest part of North America. The difference is significant at the 99% significance level at two of the centres of the teleconnection pattern (Fig. 4.15d). The systematic error patterns averaged for days 6–10 (not shown) reveal very similar features as in Fig. 4.15, except for weaker amplitudes.

Similar results have been reported by earlier studies from operational forecast data. Using the medium range forecast data set of the U.S. National Meteorological Center (NMC) for 7 years, O'Lenic and Livezey (1988) showed the dependence of the systematic error of the numerical forecasts on some of the low-frequency 700 hPa height patterns. They noted the tendency for the error patterns to be in opposite phase to the observed PNA. From a sample of the European Centre for Medium Range Weather Forecasts (ECMWF) operational 10-day forecast data, Molteni and Tibaldi (1990) also found that a regime-dependent component exists in the systematic error fields, with its pattern opposite to the anomaly of the observed flow regime.

From the present analysis of the large set of forecast experiments, and by the use of "perfect model" approach in which we consider the systematic error not to be influenced by the model's imperfection, we can confirm that there is a negative correlation between the systematic error and the slowly-varying PNA pattern. This error pattern depends only on the weather regime phase. The negative correlation of the error and the flow pattern suggests that the forecasts tend to underestimate the amplitude of the slowly-varying circulation pattern.

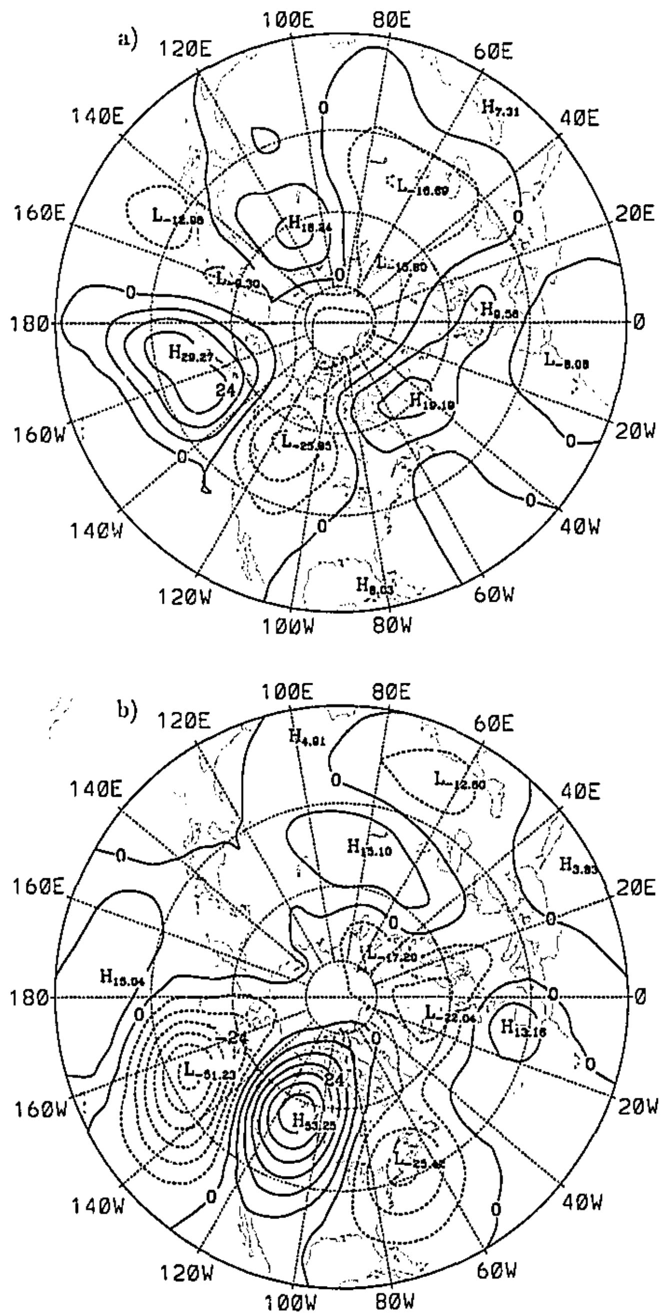

Figure 4.15: Distribution of systematic error of 500 hPa geopotential height of 5-day average for days 11–15 for (a) positive PNA phases; (b) negative PNA phases. (c) Difference by subtracting (b) from (a). (d) Areas where the systematic errors are different at significance levels of 90%, 95% and 99%.

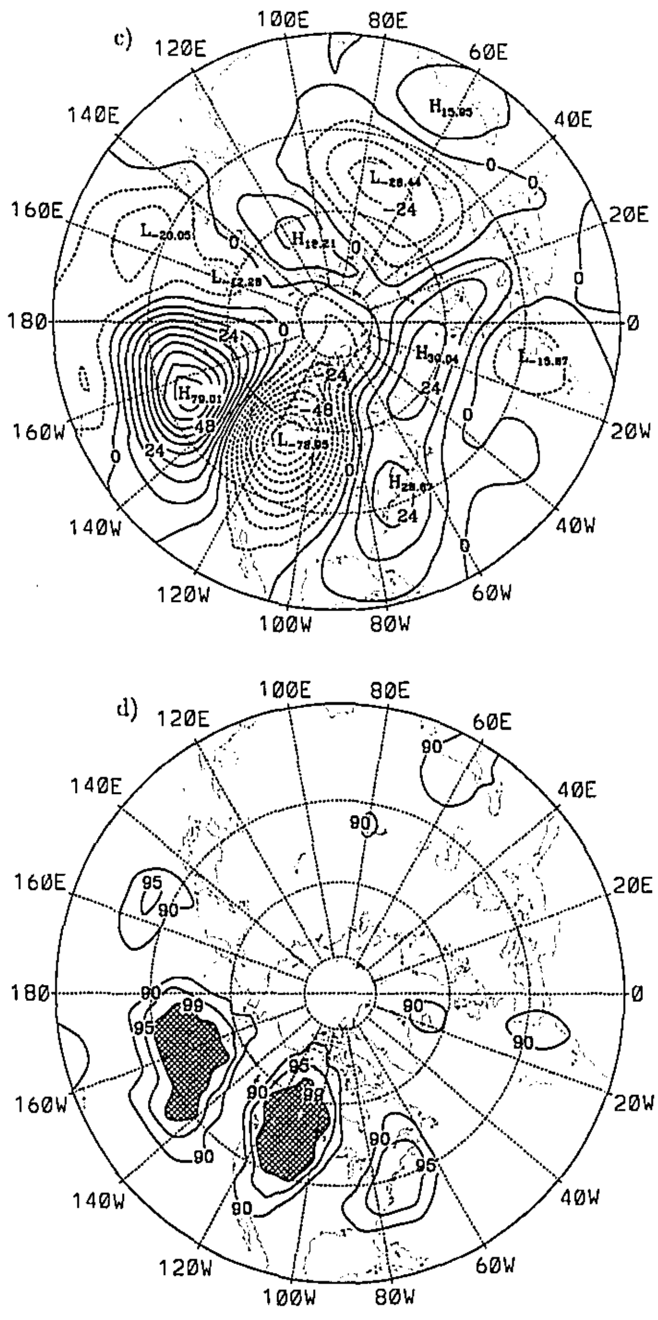

Figure 4.15: Continued.

4.7.2 The explanation

Molteni and Tibaldi (1990) explained the regime-related error in the framework of a stochastically-perturbed dynamical system. From the fact that even the most sophisticated general circulation models (GCMs) are not able to represent properly all sources of variability in the real atmosphere, they studied the Fokker–Planck equation, and showed that the reduction in the variance of stochastic perturbations causes a further increase of the frequency of the regime corresponding to the highest density maximum, and a decrease of the frequency of others. Thus numerical models tend to relax the flow towards its most densely populated regime.

In our study, because the model used for the forecasts is exactly the same as that used to obtain the "truth", there is no reduction in the variance of stochastic perturbations and a model deficiency cannot be blamed for the regime-related systematic error. The only explanation is from the internal dynamics of the nonlinear system.

The model we used is a nonlinear system with a stationary external forcing. All the variabilities produced are caused by the internal processes of the nonlinear interactions. On the other hand, the external forcing is designed in such a way that the model can have a reasonable climatology. A set of integrations of the model for a sufficient long time should yield the same climatology no matter what initial conditions are used. In other words, the climatological behaviour of the system will be independent of the initial conditions after some time, i.e., the details of initial conditions will be forgotten.

Keeping the above points in mind, let us discuss how the regime-related systematic error happens in our experiments. Assume we conduct a set of forecasts during the positive PNA phase. If each forecast is done for such a long time that the average state of the forecasts has no memory of its individual initial conditions, the average of these forecasts will not be different from the average of a single long-time integration which is the climatology. For the medium range forecasts the states of atmosphere should lie between the initial state which is in a positive PNA phase and the climatology with a zero PNA index. Therefore, for the forecasts during the positive PNA phases, a systematic error (forecast−truth) with a negative PNA pattern is obtained. Similarly the systematic error with a positive PNA pattern is expected for those medium range forecasts performed during the negative PNA phase.

4.7.3 Discussion

We have seen that the systematic error of medium range forecasts is negatively correlated with the slowly-varying flow pattern. It seems that we can use this result to make corrections to medium range forecasts if we know the PNA phase during the forecast period. However, this step is very difficult unless we know, *a priori*, the amplitude and phase of the PNA pattern. First of all, we need to predict the slowly-varying flow pattern (interannual variation in our case), which may not be possible. In a model with a time-independent external forcing like the one we are using in this study, the "interannual" variability is caused by nonlinear interactions and we can see little potential predictability for this variability. That the forecasts tend to relax to the climatology also indicates that the model is not able to predict the persistent anomaly.

Perhaps it is more useful to estimate the possible error pattern of forecasts by using the time-averages forecast data. In our experiments, because of the "perfect model" approach, the forecast and the "truth" can be switched into each other. Using the same idea as presented in our discussion of the regime-related systematic error, if the time-averaged forecast field is in an extreme anomalous flow situation, i.e., a persistent anomaly occurs in the forecast field, the "truth" must relax to the climatology in a statistical sense, and thus the forecast tends to overestimate the "truth" anomaly. Therefore, to reduce the systematic error one may subtract an error pattern similar to that of the time-averaged forecast field.

We have explained the regime-dependent systematic error based on the assumption that all the variabilities are caused by internal nonlinear processes and that the system has a single climatology. Let us consider another extreme situation in which the PNA anomaly is caused only by some external forcing. Obviously the systematic error pattern will then not be negatively correlated with the PNA pattern. In this case the the external forcing is no longer time-independent. Because the positive and negative PNA phases are associated with different external forcings, we cannot expect the forecast to relax to a single climatology. As can be expected, the forecasts made during the positive (negative) PNA phase tend to relax to the climatology determined by its own external conditions, and this climatology could be a response to the forcing and have a positive (negative) PNA phase. Therefore little or no systematic error will occur in the absence of model errors. In a more realistic GCM, both internal and external processes are present to generate the slowly-varying PNA anomaly. From the results of the NMC and ECMWF models (O'Lenic and Livezey, 1988; Molteni and Tibaldi, 1990), significant regime-dependent errors have been observed. This suggests that there are important signatures of internal variability in these two models.

4.8 Summary and conclusions

In this chapter, we have used a 3-level Q-G model to conduct a large number of forecast experiments. The relationship between the forecast behaviour and the "interannual" variation of the PNA anomaly has been investigated. The main purpose was to identify those cases that are more predictable than the others.

The Q-G model was forced by a time-independent external forcing to produce a realistic climatology. A control run was performed for 300 "winters". The "interannual" variability of the seasonal mean flow were investigated. We found that the model was able to produce significant "interannual" variability.

A "perfect model" approach was used where the perpetual winter control run served as a proxy for the atmospheric observations. Forecast experiments were made from the initial conditions by adding to the reference state some analysis errors, which were simulated by a bred mode.

A comparison of the forecast error growth during the positive PNA phase and the negative PNA phase was made by composite analysis. Little difference of the error growth can be seen before about a week. Subsequently the error grows faster when the forecasts are made during the negative PNA phase. The forecast skill for the medium- and long-range predictions over the North Pacific, North American and the North Atlantic regions is higher during the positive PNA phases than that during the negative PNA phases. The physical mechanism for the difference in the error growth was discussed. We found that the weaker intraseasonal fluctuations during the positive PNA phase are responsible for the smaller rms errors. The intraseasonal fluctuations develop by extracting kinetic energy from the seasonal mean flow and through the barotropic interaction with the high-frequency eddies. By analyzing the data from the control run, we have seen that during the positive PNA phase the low-frequency transients extract less kinetic energy from both sources.

We have also compared the average error patterns in the 500 hPa height fields during the positive and negative PNA phases. A negative correlation between the systematic error and the slowly-varying PNA pattern was observed. Based on the fact that all the variabilities in our model are caused by internal nonlinear processes and that the system has a single climatology, the regime-dependent systematic error was explained. For the medium range forecasts made during the positive (negative) PNA phase, the averaged atmospheric state should lie between the climatology and the initial state which has a positive (negative) PNA pattern. Thus the systematic error has a negative (positive) PNA pattern.

Chapter 5

Summary and Conclusions

In this thesis we have investigated the atmospheric low-frequency temperature variability (periods from 10 days to a season) and its interaction with the higher-frequency synoptic-scale eddies. The high-frequency eddies transport heat, and the divergence of this heat flux affects the temperature tendency of the slower time scales.

The temporal correlation was calculated between the low-frequency temperature field and the heat flux convergence by the high-frequency eddies. It was found that the correlation is negative, implying that the heat flux by the faster eddies tends to damp the low-frequency temperature fluctuations, just as it does for the time-mean temperature (Holopainen et al., 1982).

In contrast to the low-frequency height field, which has maximum variances over the eastern Pacific and Atlantic, the low-frequency temperature field has maximum variances over the continental land masses of Canada and Siberia. The likely explanation is that the air-sea interactions tend to smooth out the atmospheric temperature field in the lower troposphere, thereby reducing the possibility of maintaining long-lasting temperature anomalies over oceanic areas. The main horizontal structures of the low-frequency temperature have been obtained by an EOF analysis. The first modes in the East Asian and North American sectors represent the intensity variation of the temperature field in the regions of its maximum variability located over the continental land masses of Siberia and Canada, respectively. The second and the third eigenvectors are connected with the fluctuations of the temperature field in the east coastal areas near the storm tracks.

While negative temporal correlations are generally observed between the low-frequency temperature and the heat flux convergence by the high-frequency eddies, this relation is not geographically homogeneous. The maximum negative correlations were found over the two major storm track regions. Furthermore, the eddy heat flux has less damping effect on the first eigenvectors of the low-frequency temperature field than on the second and third eigenvectors.

We have also studied the interannual variation of the extratropical flow. Significant differences have been found in the winter seasonal mean flow, the low-frequency eddies and the synoptic-scale transients between the El Niño and the non-El Niño winters. During the El Niño winters when the PNA pattern in the seasonal mean geopotential height field is enhanced, the low-frequency eddy activity is reduced over the North Pacific, and the persistent, strong-amplitude anomalies in this area are less frequent. The mechanisms responsible for the interannual variation of the low-frequency fluctuations were discussed.

The reduction of the low-frequency transient activity over the North Pacific during the El Niño winters is caused by two processes. One is that less kinetic energy is supplied to the low-frequency eddies from the large-scale seasonal mean flow. This reduction in the barotropic energy transfer from the mean flow may be related to the decrease of the longitudinal gradient of the basic zonal flow ($\partial\overline{u}/\partial x$) over the western and central Pacific during the El Niño winters. The other mechanism is that the strong seasonal mean Aleutian low tends to keep the baroclinic synoptic-scale eddies moving along its southern side, causing only a weak interaction with the low-frequency eddies in the Northern Pacific, and thus less synoptic-scale eddy forcing for the low-frequency flow.

The weak low-frequency activity over the North Pacific and the southward shift of the baroclinic eddy activity indicate that the transient activity over the North Pacific is significantly reduced during the El Niño winters. The reduced energy transfer to the low-frequency transients from the barotropic energy conversion and the synoptic-scale eddy forcing implies that the interactions between eddies with different time scales are less active during El Niño winters, at least over the North Pacific region. Therefore, the atmospheric internal nonlinear processes that may cause an anomalous seasonal mean flow become less important, which would suggest that the atmospheric response to an external oceanic forcing would be more "stable". If this is the case, we would expect long-range weather predictions during a positive PNA pattern to be more reliable over the North Pacific.

Using a 3-level Q-G model, the level of atmospheric predictability and its relation with the PNA anomaly has been investigated explicitly. The Q-G model was forced by a time-independent external forcing to produce the realistic climatology. A control run was conducted for 300 "winters", and the "interannual" variability of the seasonal mean flow was investigated. We found that the model is able to produce significant "interannual" variability. The Pacific/North American (PNA) pattern, which is one of the most important anomalous seasonal mean flow patterns, has been well simulated.

Comparison of the error growth for the forecasts made during the positive and negative PNA phases was made by composite analysis. Little difference of error growth can be realized before about a week. After that period the error grows faster when the forecasts are made during the negative PNA phases. The medium-range forecast skill is better during a positive phase than during a negative PNA phase over the North Pacific, the North American and the North Atlantic regions. Even when globally averaged, the forecast errors are somewhat smaller during positive PNA periods than during negative PNA periods.

Appendix A

Student's t-test for Significance of Difference

Suppose we have two time series x_i $(i = 1, 2, ...N_1)$, and y_j $(j = 1, 2, ...N_2)$ for the same variable (e.g., both are 700 hPa temperature at a given grid point). The second time series is obtained in a slightly different environment from that of the first time series. We would like to know whether the "environment change" (e.g., from non-El Niño to El Niño winters) leads to a statistically significant difference in the variable under analysis.

We will follow the student's t-test for significantly different means described in *Numerical Recipes* (Press et. al., 1986). Firstly, the standard error is estimated, which can be written as

$$e_s = \left(\frac{\sum_{i=1}^{N_1}(x_i - \overline{x})^2 + \sum_{j=1}^{N_2}(y_j - \overline{y})^2}{N_1 + N_2 - 2} \left(\frac{1}{N1} + \frac{1}{N_2}\right) \right)^{\frac{1}{2}}, \tag{A.1}$$

where N_1 and N_2 are the lengths of the first and second time series, respectively.

Secondly, compute t by

$$t = \frac{\overline{x} - \overline{y}}{e_s}. \tag{A.2}$$

Finally, evaluate the significance of this value of t for Student's distribution with the degree of freedom $\mu = N_1 + N_2 - 2$, by the equation

$$A(t|\mu) = \frac{1}{\mu^{\frac{1}{2}} B(\frac{1}{2}, \frac{\mu}{2})} \int_{-t}^{t} (1 + \frac{s^2}{\mu})^{-\frac{\mu+1}{2}} ds, \tag{A.3}$$

where $B(a, b)$ is the beta function which is defined as:

$$B(a, b) = \int_0^1 z^{a-1}(1-z)^{b-1} dz. \tag{A.4}$$

$A(t|\mu)$ is a number between 0 and 1, and is the probability that t would be smaller than the value calculated in (A.2) if the means were the same. Thus the means of the two time series are significantly different if $A(t|\mu)$ is large (e.g, 0.99 or 0.95).

Bibliography

Bergman, K. H., 1987: The global climate of September–November 1986: A moderate ENSO warming develops in the tropical Pacific. *Mon. Wea. Rev.*, **115**, 2524–2541.

Bjerkness, J., 1966: A possible response of the atmospheric Hadley circulation to equatorial anomalies of ocean temperature. *Tellus*, **18**, 820–829.

——, 1969: Atmospheric teleconnections from the equatorial Pacific. *Mon. Wea. Rev.*, **97**, 163–172.

Blackmon, M. L., 1976: A climatological spectral study of the 500 mb geopotential height of the Northern Hemisphere. *J. Atmos. Sci.*, **33**, 1607–1623.

——, J. M. Wallace, N. C. Lau and S. L. Mullen, 1977: An observational study of the Northern Hemisphere wintertime circulation. *J. Atmos. Sci.*, **34**, 1040–1053.

——, Y.-H. Lee and J. M. Wallace, 1984a: Horizontal structure of 500mb height fluctuations with long, intermediate and short time scales. *J. Atmos. Sci.*, **41**, 961–979.

——, ——, ——, and H.-H. Hsu, 1984b: Time variation of 500 mb height fluctuations with long, intermediate, and short time scales as deduced from lag-correlation statistics. *J. Atmos. Sci.*, **41**, 981–991.

Branstator, G., 1985: Analysis of general circulation model sea surface temperature anomaly simulations using a linear model. Part I: Forced solutions. *J. Atmos. Sci.*, **42**, 2225–2241.

——, 1990: Low-frequency patterns induced by stationary waves. *J. Atmos. Sci.*, **47**, 629–648.

Charney, J. G., 1947: The dynamics of long waves in a baroclinic westerly current. *J. Meteor.*, **4**, 135–163.

——, 1960: Numerical prediction and the general circulation. *Dynamics of Climate*, R. L. Pfeffer, Ed., Pergamon, 12–17.

——, R. G. Fleagle, V. E. Lally, H. Riehl and D. Q. Wark, 1966: The feasibility of a global observation and analysis experiments. *Bull. Amer. Meteor. Soc.*, **47**, 200–220.

Cubasch, U., 1985: The mean response of the ECMWF global model to the composite El Niño anomaly in the extended range prediction experiments. *Coupled ocean-atmosphere models*, Ed. J. Nihoul, Elsevier Press, pp. 329–344.

Dole, R. M., and N. D. Gordon, 1983: Persistent anomalies of the extratropical Northern Hemisphere wintertime circulation: Geographical distribution and regional persistence characteristics. *Mon. Wea. Rev.*, **111**, 1567–1586.

Eady, E. T., 1949: Long waves and cyclone waves. *Tellus*, **1**, 35–52.

Epstein, E. S., 1969: Stochastic-dynamic prediction. *Tellus*, **21**, 739–759.

Frederiksen, J. S., 1979: The effect of long planetary waves on the regions of cyclogenesis. *J. Atmos. Sci.*, **36**, 195–204.

Green, J. S. A., 1977: The weather during July 1976: Some dynamical considerations of the drought. *Weather*, **32**, 120–126.

Hanson, H. P., and B. Long, 1985: Climatology of cyclogenesis over the East China Sea. *Mon. Wea. Rev.*, **113**, 697–707.

Held, I. M., S. W. Lyons and S. Nigam, 1989: Transients and the extratropical response to El Niño. *J. Atmos. Sci.*, **46**, 163–174.

Hendon, H. H., and D. L. Hartmann, 1985: Variability in a nonlinear model of the atmosphere with zonally symmetric forcing. *J. Atmos. Sci.*, **42**, 2783–2797.

Hoerling, M. P., and M. Ting, 1994: On the organization of extratropical transients during El Niño. *J. of Climate*, **7**, 745–766.

Holopainen, E. O., L. Rontu and N.-C. Lau, 1982: The effect of large-scale transient eddies on the time-mean flow in the atmosphere. *J. Atmos. Sci.*, **39**, 1972–1984.

——, 1984: Statistical local effect of synoptic-scale transient eddies on the time-mean flow in the Northern extratropics in winter. *J. Atmos. Sci.*, **41**, 2505–2515.

——, 1994: Cyclone climatology and its relationship to planetary waves and physiography. *Proceedings of an international symposium on the life cycles of extratropical cyclones*, Vol. I, Bergen-Norway, S. Grønås and M. Shapiro Eds., 72–79.

Horel, J. D., and J. M. Wallace, 1981: Planetary scale atmospheric phenomena associated with the Southern Oscillation. *Mon. Wea. Rev.*, **109**, 813–829.

Hoskins, B. J., A. J. Simmons and D. G. Andrews, 1977: Energy dispersion in a barotropic atmosphere. *Q. J. Roy. Meteor. Soc.*, **103**, 553–567.

——, and D. J. Karoly, 1981: The steady linear response of a spherical atmosphere to thermal and orographic forcing. *J. Atmos. Sci.*, **38**, 1179–1196.

——, I. N. James and G. H. White, 1983: The shape, propagation and mean-flow interaction of large scale weather systems. *J. Atmos. Sci.*, **40**, 1595–1612.

Houtekamer, P. L., J. Derome, 1994: Prediction experiments with two-member ensembles. *Mon. Wea. Rev.*, **122**, 2179–2191.

Kok, C. J., and J. D. Opsteegh, 1985: On the possible causes of anomalies in seasonal mean circulation pattern during the 1982–83 El Niño event. *J. Atmos. Sci.*, **42**, 677–694.

Klasa, M., J. Derome and J. Sheng, 1992: On the interaction between the synoptic-scale eddies and the PNA teleconnection pattern. *Beitr. Phys. Atmosph./Contrib. Atmos. Phys.*, **65**, 211–222.

Lau, K.-M., and J. S. Boyle, 1987: Tropical and extratropical forcing of the large-scale circulation: A diagnostic study. *Mon. Wea. Rev.*, **115**, 400–428.

Lau, N.-C., 1979: The observed structure of tropospheric stationary waves and the local balances of vorticity and heat. *J. Atmos. Sci.*, **36**, 996–1016.

——, 1981: A diagnostic study of recurrent meteorological anomalies appearing in a 15-year simulation with a GFDL general circulation model. *Mon. Wea. Rev.*, **109**, 2287–2311.

——, and E. O. Holopainen, 1984: Transient eddy forcing of the time-mean flow as identified by geopotential tendencies. *J. Atmos. Sci.*, **41**, 313–328.

——, 1985: Modeling the seasonal dependence of the atmosphere response to observed El Ninos in 1962-76. *Mon. Wea. Rev.*, **113**, 1970–1996.

——, 1988: Variability of the observed midlatitude storm tracks in relation to low-frequency changes in the circulation pattern. *J. Atmos. Sci.*, **45**, 2718–2743.

——, and M. J. Nath, 1991: Variability of the baroclinic and barotropic transient eddy forcing associated with monthly changes in the midlatitude storm tracks. *J. Atmos. Sci.*, **48**, 2589–2613.

Leith, C. E., 1974: Theoretical skill of Monte Carlo forecasts. *Mon. Wea. Rev.*, **102**, 409–418.

Lin, H., and J. Derome, 1993: Thermal forcing of slow transients by synoptic scale eddies in the atmosphere. C^2GCR Report No. 93–10.

——, and ——, 1994: On the thermal interaction between the synoptic-scale eddies and the intra-seasonal fluctuations in the atmosphere. Accepted by *Atmosphere-Ocean.*

Lorenz, E. N., 1963: Deterministic nonperiodic flow. *J. Atmos. Sci.*, **20**, 130–141.

——, 1969: The predictability of a flow which possesses many scales of motion. *Tellus*, **21**, 289–307.

Madden, R. A., 1976: Estimates of the natural variability of time-averaged sea-level pressure. *Mon. Wea. Rev.*, **104**, 942–952.

Mansfield, D. A., 1986: The skill of dynamical long-range forecasts, including the effect of sea surface temperature anomalies. *Q. J. R. Meteorol. Soc.*, **112**, 1145–1176.

Marshall, J., and F. Molteni, 1993: Toward a dynamical understanding of planetary-scale flow regimes. *J. Atmos. Sci.*, **50**, 1792–1818.

Metz, W., 1990: Empirical modelling of extra-tropical cyclone vorticity fluxes. *Tellus*, **42A**, 14–27.

——, 1991: Optimal relationship of large-scale flow patterns and the barotropic feedback due to high-frequency eddies. *J. Atmos. Sci.*, **48**, 1141–1159.

Miyakoda, K., J. Sirutis and J. Ploshay, 1986: One month forecast experiments—without anomaly boundary forcing. *Mon. Wea. Rev.*, **114**, 2363–2401.

Molteni, F., and S. Tibaldi, 1990: Regimes in the wintertime circulation over northern extratropics. II: Consequences for dynamical predictability. *Q. J. R. Meteor. Soc.*, **116**, 1263–1288.

Mullen, S. L., 1987: Transient eddy forcing of blocking flows. *J. Atmos. Sci.*, **44**, 3–22.

Nakamura, H., M. Tanaka and J. M. Wallace, 1987: Horizontal structure and energetics of Northern Hemisphere wintertime teleconnection patterns. *J. Atmos. Sci.*, **44**, 3377–3391.

North, G. R., T. L. Bell, R. F. Cahalan and F. J. Moeng, 1982: Sampling errors in the estimation of empirical orthogonal functions. *Mon. Wea. Rev.*, **110**, 699–706.

O'Lenic, E. A., and R. E. Livezey, 1988: Relationships between initial circulation anomalies and forecast errors. *Predictability in the medium and extended range*, ECMWF Workshop Proceedings, 311–339.

Palmer, T. N., and Z.-B. Sun, 1985: A modelling and observational study of the relationship between sea surface temperature in the north-west Atlantic and the atmospheric general circulation. *Q. J. R. Meteor. Soc.*, **112**, 613–638.

——, 1988: Medium and extended range predictability and stability of the Pacific/North American mode. *Q. J. R. Meteorol. Soc.*, **114**, 691–713.

——, and S. Tibaldi, 1986: Forecast skill and predictability. ECMWF Technical Memorandum No. 127.

Pandolfo, L., 1993: Observational aspects of the low-frequency intraseasonal variability of the atmosphere in middle latitudes. *Adv. Geophys.*, **34**, 93–174.

Petterssen, S., 1956: *Weather analysis and Forecasting. Vol. 1*, 2nd ed., McGraw-Hill, 422pp.

Press, W. H., B. P. Flannery, S. A. Teukolsky and W. T. Vetterling, 1986: *Numerical Recipes*, Cambridge Univ. Press.

Quinn, W. H., D. O. Zopf, K. S. Short and R. T. W. Kuo Yang, 1978: Historical trends and statistics of the Southern Oscillation, El Niño and Indonesian droughts. *Fish. Bull.*, **76**, 663–678.

Quiroz, R. S., 1983: The climate of the "El Niño" winter of 1982-83—A season of extraordinary climatic anomalies. *Mon. Wea. Rev.*, **111**, 1685–1706.

Rasmusson, E. M., and T. H. Carpenter, 1982: Variations in tropical sea surface temperature and surface wind fields associated with the Southern Oscillation/El Niño. *Mon. Wea. Rev.*, **110**, 354–384.

Rex, D. F., 1950: Blocking action in the middle troposphere and its effect upon regional climate . II. The climatology of blocking action. *Tellus*, **2**, 275–301.

Robinson, W. A., 1991: The dynamics of low-frequency variability in a simple model of the global atmosphere. *J. Atmos. Sci.*, **48**, 429–441.

Sheng, J., and J. Derome, 1991a: An observational study of the energy transfer between the seasonal mean flow and transient eddies. *Tellus*, **43A**, 128–144.

——, and ——, 1991b: On the interactions among flow components in different frequency bands in the Canadian Climate Centre general circulation model. *Atmosphere-Ocean*, **29**, 62–84.

——, and ——, 1993: The dynamic forcing of the slow transients by the synoptic-scale eddies: An observational study. *J. Atmos. Sci.*, **50**, 757–771.

——, and Y. Hayashi, 1990: Estimation of atmospheric energetics in the frequency domain during the FGGE year. *J. Atmos. Sci.*, **47**, 1255–1268.

Shutts, G. J., 1983: Parameterization of traveling weather systems in a simple model of large-scale atmospheric flow. *Adv. Geophys.*, **25**, 117–172.

Simmons, A. J., J. M. Wallace and G. W. Branstator, 1983: Barotropic wave propagation and instability, and atmospheric teleconnection patterns. *J. Atmos. Sci.*, **40**, 1363–1392.

Ting, M., and N.-C. Lau, 1993: A diagnostic and modeling study of the monthly mean wintertime anomalies appearing in a 100-year GCM experiment. *J. Atmos. Sci.*, **50**, 2845–2867.

——, and M. P. Hoerling, 1993: The dynamics of stationary wave anomalies during the 1986/87 El Nino. *Climate Dyn.*, **9**, 147–164.

Toth, Z., and E. Kalnay, 1992: Growing modes of the atmosphere obtained by "breeding" and their application to ensemble forecasting. *Proceedings of the Second International Conference on Modelling of Global Climate Change and Variability.* Hamburg, pp. 84–87.

Tung, K. K., and A. J. Rosenthal, 1986: On the extended-range predictability of large-scale quasi-stationary patterns in the atmosphere. *Tellus*, **38A**, 333–365.

Vinnichenko, N. K., 1970: The kinetic energy spectrum in the free atmosphere—1 second to 5 years. *Tellus*, **22**, 158–166.

Wallace, J. M., and D. S. Gutzler, 1981: Teleconnections in the geopotential height field during the Northern Hemisphere winter. *Mon. Wea. Rev.*, **109**, 784–812.

——, and M. L. Blackmon, 1983: Observations of low-frequency atmospheric variability. *Large-Scale Dynamical Processes in the Atmosphere*, B. J. Hoskins and R. P. Pearce Eds, Academic Press, 55–94.

——, and N.-C. Lau, 1985: On the role of barotropic energy conversions in the general circulation. *Adv. Geophys.*, **28A**, 33–74.

——, G.-H. Lim and M. L. Blackmon, 1988: Relationship between cyclone tracks, anticyclone tracks and baroclinic waveguides. *J. Atmos. Sci.*, **45**, 439–462.